University of Alberta

LUCID and QUARTIC Detector Development in the Forward Region of ATLAS

by

Yushu Yao ©

A thesis submitted to the Faculty of Graduate Studies and Research in partial fulfillment of the requirements for the degree of Doctor of Philosophy

Department of Physics

Edmonton, Alberta
Spring 2008

Your file Votre référence
ISBN: 978-0-494-45632-3
Our file Notre référence
ISBN: 978-0-494-45632-3

Abstract

The ATLAS detector construction is now completed and ready to explore the widest possible range of physics signals after the LHC collider begins running in 2008, at the unprecedented centre of mass energy of 14 TeV.

LUCID is the luminosity monitor of the ATLAS detector designed to achieve a precise measurement of luminosity across the full range of operation of the ATLAS detector, eventually as good as a few percent after calibration with elastic proton scattering data in the Coulomb scattering region. This thesis presents the design, simulation, bench test and test beam study of the LUCID detector.

It is envisaged that the FP420 detectors will be installed at approximately $\pm$420 m from the ATLAS interaction point as part of the project to extend the physics reach of ATLAS in the forward region. Accurate time of flight measurements will be necessary in order to reduce pile-up induced backgrounds in the FP420 detectors. This thesis presents the design, simulation and test beam study of the QUARTIC prototype, an ultra precise Cerenkov time-of-flight detector. Simulation and test beam studies indicate that a 10 ps time resolution is achievable with the QUARTIC detector. Such a resolution would reduce the pile-up background by a factor of fifty.

The exclusive two photon di-muon production process ($pp \rightarrow p\gamma\gamma p \rightarrow p\mu^+\mu^- p$) can be used to calibrate the energy measurement of the FP420 detectors. In this thesis a simulation study combining the LPAIR MC and ATLAS full simulation shows that this process could be used to calibrate the mass of a reconstructed central mass with a resolution of better than one GeV/c^2.

Acknowledgements

I wish to acknowledge all those who have helped to make the last 5 years a challenging, pleasant and memorable experience.

Heart-felt thanks are deserved for my supervisor, Dr. James Pinfold, not only for his ideas and suggestions that made this thesis possible, but also for his wise words and encouragements. He led me into the world of particle physics.

I also wish to thank Dr. Doug Gingrich, Dr. Roger Moore and Dr. Andrzej Czarnecki who gave me thought provoking lectures, that made my introduction to the world of particle physics an enthralling experience.

I would like to thank my thesis advisory and examination committee members: Professor George Lolos, Professor Gino Fallone, Professor Doug Schmitt, Professor Doug Gingrich and Associate Professor Roger Moore, for their advice and commitment. Thanks also to the electrical and mechanical engineers, Lars Holm, Len Wampler, Pat Wong, Paul Zimmermann, John Schaapman for their help and support on my research. I also wish to thank all the members of Centre for Particle Physics (CPP) for a friendly environment especially to Suzette Chan, the CPP administrator.

I also owe great thanks to my fellow graduate students, Hossain Ahmed, Logan Sibley, Wei-yuan Ting, Kevin Chan, Feng Wang, Xuantao Su, for interesting discussions and continuous friendship.

Last, but not least, I would like to thank my family for their uninterrupted support and understanding.

Table of Contents

1 Introduction **1**

2 Theory and Motivation **5**
2.1 Standard Model 5
2.2 Physics at ATLAS 7
2.3 Exclusive Interactions at Hadron Colliders 8
2.3.1 Two-photon Physics (QED Exclusive Interactions) . . . 10
2.3.2 QCD Mediated Exclusive Interactions 13
2.3.3 QCD Exclusive Higgs Production 13
2.3.4 Advantages of Exclusive Interaction 15

3 LHC and ATLAS **17**
3.1 LHC 17
3.2 ATLAS 19
3.2.1 Inner Detector 20
3.2.2 Magnet System 25
3.2.3 Calorimeter 25
3.2.4 Muon System 34
3.2.5 ATLAS Trigger System 38
3.3 Detectors in the Forward Region of ATLAS 40

4 Luminosity Measurement at ATLAS **43**
4.1 Introduction to Luminosity 43
4.1.1 Luminosity Blocks 44
4.2 Methods for Luminosity Determination in ATLAS 45
4.2.1 LHC Machine Parameters (Absolute/Relative) 45
4.2.2 W/Z Counting (Absolute/Relative) 46
4.2.3 $pp \to p\gamma\gamma p \to p\mu^+\mu^- p$ (Absolute) 46
4.2.4 Roman Pots (ALFA) 47
4.2.5 LUCID (Relative) 47
4.2.6 Beam Condition Monitor (Relative) 49
4.3 Luminosity Monitoring with LUCID 50
4.3.1 Collision (Zero) Counting Method 50

4.3.2 Particle Counting Method 51

5 A Luminosity Monitor for ATLAS - LUCID 53
5.1 Introduction 53
5.2 Design of LUCID 54
5.2.1 Phase I LUCID Detector 54
5.2.2 Phase II LUCID Detector 66
5.2.3 Optical Fibre 66
5.3 Electronics and Readout 68
5.4 Radiation Environment of LUCID 71
5.5 Calibration of LUCID 73
5.6 Simulation of LUCID 74
5.7 Integrating LUCID into ATLAS Data Chain 74

6 LUCID Test Beam and Bench Test Experiments 77
6.1 Introduction 77
6.2 Bench Test Setup 78
6.3 Test Beam Experiment and Simulation Setup 79
6.3.1 Test Beam Experiment Setup 79
6.3.2 Simulation Setup 80
6.3.3 Simulation Parameters 81
6.4 Test Beam Results and Simulation 84
6.4.1 Result from PMT Readout Detectors 84
6.4.2 Results from Fibre Readout Detectors 92
6.4.3 Winston Cone 92
6.5 Conclusion 99

7 Performance of the LUCID Phase I 101
7.1 Introduction 101
7.2 Setup and Procedure of Simulation 101
7.3 Expected LUCID Phase I Performance 106
7.3.1 Photo-electrons Generated in the PMT 106
7.3.2 Estimate of the Number of Photo-electrons Generated in the MAPMT 107
7.3.3 Definition of Hits 109
7.3.4 Determination of Threshold at Higher Luminosity . . . 109
7.3.5 Detection Efficiency of LUCID 110
7.3.6 Linear Response of the LUCID 111
7.4 Systematic Error Analysis 112
7.4.1 Beam Optics 114
7.4.2 Interaction Point Displacement Along the Beam Axis . 114
7.4.3 Gas Pressure 115
7.4.4 Temperature Variance 116

7.4.5 Gas Contamination 116
7.4.6 LUCID Alignment 117
7.4.7 PMT Gain Stability 117
7.5 Conclusion 118

8 FP420 Detector **121**
8.1 Introduction 121
8.2 Physics at FP420 122
8.3 Acceptance, Resolution and Calibration 123
8.4 Backgrounds 124
8.5 Proton Tagging Detectors in FP420 125
8.5.1 Modifications to the 420 m Region 125
8.5.2 Positioning the Detectors 126
8.5.3 Silicon Detector 126
8.5.4 Time of Flight Detectors 128

9 QUARTIC - The Time of Flight Detector for FP420 **129**
9.1 Introduction 129
9.2 Design of QUARTIC 129
9.3 Simulation Study of QUARTIC 131
9.3.1 Simulation Parameters 132
9.3.2 Hit Positions of Photons on the MCP-PMT Face . . . 133
9.3.3 Time and Wavelength Distribution of Photons 134
9.3.4 Time Resolution 134
9.3.5 Effect of PMT Quantum Efficiency 141
9.3.6 Number of Photoelectrons 141
9.4 Test beam and Preliminary Results 141
9.5 Simulation Study of an Alternate QUARTIC Design 144
9.6 Conclusion 146

10 Calibration of FP420 with Muon Pair Production **149**
10.1 Introduction 149
10.2 Procedure 150
10.3 Results 150
10.3.1 Detection of Protons by FP420 151
10.3.2 Reconstruction of Central State 153
10.3.3 Precision of the Calibration 153
10.4 Conclusion 156

11 Conclusion **157**

Bibliography **161**

A Estimation of Systematic Error from Beam Optics **169**

List of Tables

2.1 List of Fermions 5
2.2 Standard Model Force Mediating Particle 6

3.1 Selected Machine and Beam Parameters of LHC 19
3.2 Inner Detector Components and Their Corresponding Typical Measurement Resolutions 23

5.1 Major Design Parameters of LUCID 57

6.1 List of Detectors in Each Test Beam Experiment. 81

7.1 List of Beam Conditions 114
7.2 List of Systematic Errors and Significance 119

List of Figures

2.1 ATLAS Sensitivity for Discovery of Higgs Boson 8
2.2 Feynman Diagrams for Exclusive Interactions 9
2.3 Rapidity Gap 10
2.4 Feynman Diagrams of Two-Photon Interactions 11
2.5 Effective Two-Photon Luminosities at the LEP and LHC . . . 12
2.6 Feynman Diagram of QCD Exclusive Higgs Production 13
2.7 Higgs Production Cross-sections at the LHC 14

3.1 Artist's Impression of an LHC Cryodiple 18
3.2 LHC Accelerators and Detectors 18
3.3 A Drawing of the ATLAS Detector 20
3.4 Cross Section of the ATLAS Detector in X-Y Plane 21
3.5 Cross Section of the ATLAS Detector in R-Z Plane 22
3.6 Artistic drawing of the ATLAS Inner Detector 23
3.7 Picture of the ATLAS Pixel Detector, Semiconductor Tracker and Transition Radiation Tracker 26
3.8 Scheme of ATLAS Magnet System 27
3.9 Pictures of ATLAS Magnets 28
3.10 Field Maps of the ATLAS Detector 28
3.11 Cut Away Drawing of the ATLAS Calorimetry 29
3.12 The Accordion Shape of EM Calorimeters 30
3.13 Pictures of LAr EM Barrel and End-Cap Calorimetry 31
3.14 The Hadronic Tile Barrel Calorimeter 32
3.15 The LAr End-Cap Hadronic Calorimeter 33
3.16 Positioning of FCAL Modules 35
3.17 The LAr Forward Calorimeter 35
3.18 Artistic Drawing of ATLAS Muon System 36
3.19 Schematic Diagram of the Cathode Strip Chamber 37
3.20 Schematic Diagram of the Thin Gap Chamber 38
3.21 The ATLAS Trigger System 39
3.22 Placement of the Forward Detectors along the Beam Line around the ATLAS IP 41

4.1 Relation of Higgs Cross-section Measurement and Luminosity Accuracy 44
4.2 Roman Pot Unit Assembly 48
4.3 Schematic of the Fibre Tracker 49
4.4 Non-linear relation 51

5.1 Positioning of LUCID 54
5.2 Side View of the LUCID Detector 55
5.3 Cut-away View of LUCID 56
5.4 Engineering Drawing of the LUCID Front Bulkhead 58
5.5 PMT Detector and Fibre Detector 60
5.6 Cross Section of the Fibre Bundle 60
5.7 Connection of Aluminium Tubes with PMTs and Fibre Bundles 61
5.8 LUCID Gas System 62
5.9 Artistic Drawing of LUCID Gas Vessel 63
5.10 LUCID Front Alignment Features 64
5.11 LUCID Back Alignment Features 64
5.12 LUCID Cooling Pipes 65
5.13 A Cross Section View of the LUCID Phase II Detector 67
5.14 A perspective view of LUCID Phase II Detector 68
5.15 Simulation Parameters for Fibre Readout Detector Simulation 69
5.16 Cable Connections of LUCID 70
5.17 Cable Routing of LUCID 70
5.18 Radiation Environment of LUCID - Ionizing Radiation 71
5.19 Radiation Environment of LUCID - Neutron Flux 72
5.20 Data flow of ATLAS 75

6.1 Bench Test Experiment Setup 78
6.2 Picture of the Bench Test Experiment 79
6.3 Sketch and Photograph of the Test Beam Setup 80
6.4 Setup of the Test Beam Simulation 81
6.5 List of Simulation Parameters 82
6.6 Absorption of the Fibre Core 83
6.7 Reflectivity of Aluminum Surfaces 84
6.8 Shape of the Beam Profile 85
6.9 ADC Distribution of Test Beam Signal 86
6.10 Effect of Electron Selection by the Silicon Tracker 87
6.11 Amplitude Distribution from the PMT Readout Detector . . . 88
6.12 Pressure Test for Aluminized Mylar Tube 89
6.13 Definition of Test Angle 91
6.14 Angle Test Results Compared to Simulation 91
6.15 Schematic Diagram of a Winston Cone 92
6.16 Schematic Diagram of a Winston Cone Used in Test Beam . . 93

6.17 Picture of Fibre Bundle Cross Sections 94
6.18 Signal from Fibre Readout Detector 95
6.19 Distribution of Photon at fibre Entrance 96
6.20 Test Beam Result of Angle Tests 97
6.21 Test Beam Result of Pressure Tests 97
6.22 Comparing Test Beam and Simulation Results of Pressure Tests 98

7.1 Distribution of Particles Pointing to the LUCID Region 102
7.2 Distributions of the Hit Positions of Background 103
7.3 Front View of one LUCID module in GEANT4 Simulation . . 104
7.4 Prospective View of one LUCID module in GEANT4 Simulation 105
7.5 Time of Flight Distribution of Particles when hitting the LUCID volume 106
7.6 The Response of PMT Readout Detectors 107
7.7 The Response of Fibre Readout Detectors 108
7.8 Background Subtraction in PMT Readout Detectors Using Their Adjacent Fibre Readout Detectors 110
7.9 Detection Efficiency of the LUCID Phase I 111
7.10 Linear Relationship Between Luminosity and the LUCID Phase I Response 112
7.11 Calculation of Luminosity Measurement Error 113
7.12 Linear Relationship of the LUCID Phase I for different Z-displacement of the IP 115
7.13 Systematic Error due to PMT Pressure Stability 116
7.14 Linear Relationship of LUCID Phase I for Different Temperature 117
7.15 Systematic Error due to PMT Gain Stability 118

8.1 Position of FP420 Detectors 121
8.2 FP420 Acceptance and Resolution 124
8.3 A Schematic Diagram of Pile-up Backgrounds to Central Exclusive Production 125
8.4 Sketch of FP420 Cryostat and Hamburg Pipe 127
8.5 Sketch of 3D Silicon Detector 127

9.1 Design of QUARTIC 130
9.2 Sketch and Picture of MCP-PMT 130
9.3 Simulation Parameters 132
9.4 Simulation of QUARTIC 133
9.5 Distribution of Photons 135
9.6 Time and Wavelength Plots of Photons in Channel 0 136
9.7 Time and Wavelength Plots of Photons in Channel 7 137
9.8 Effect of Quantum Efficiency For Photons that Arrive at PMT Surface 138

9.9 Effect of Quantum Efficiency For Photons that Arrive at PMT Surface and Generate a Photoelectron 139
9.10 Rise Time of QUARTIC 140
9.11 Number of Photoelectrons 142
9.12 QUARTIC Test Beam Prototype 143
9.13 Sketch of QUARTIC Test Beam Experiment Setup 143
9.14 Picture of the QUARTIC Test Beam Experiment Setup 143
9.15 Alternate QUARTIC Design 145
9.16 Simulation of Alternate QUARTIC Design 145
9.17 Distribution of Number of Photo-electron Produced in MCP-PMT 146
9.18 Time Distribution of QUARTIC Alternate Design 147

10.1 Feynman diagram for $\gamma\gamma \rightarrow \mu\mu$ 149
10.2 Flow chart for FP420 Calibration 150
10.3 Reconstruction Efficiency for ATLAS Muon System 152
10.4 Proton Energy and η Distribution 152
10.5 Muon Transverse Momentum Distribution 153
10.6 Central State Energy Distribution 154
10.7 Central State Selection Efficiency 154
10.8 Resolution for Muon Energy Measurement 155
10.9 Resolution for Proton Calibration 156

A.1 Relation of Number of Hits per unit η and the η 170
A.2 Effect of Beam Size on LUCID Acceptance 170
A.3 Effect of Beam Divergence on the LUCID acceptance 171

Chapter 1

Introduction

In 2008 with the launch of the Large Hadron Collider (LHC) at the European Centre for Particle Physics Research (CERN), the Standard Model (SM) will be tested to unprecedented energies. If the SM is correct, the Higgs Boson should be discovered within a few years of running. The two general purpose LHC detectors ATLAS and CMS have been built with the search for the Higgs boson as one of their main aims.

In addition to the development of the main ATLAS detector, there is now an exciting ongoing development of the forward region of ATLAS. The development consists of four detector systems[1]. If ordered according to distance from the interaction point, the first of these systems is the Cerenkov Luminosity Monitor, LUCID, located at a distance $\sim \pm 17$ m from the interaction point (IP). The second system is a zero degree calorimeter (ZDC) which is located at a distance of ± 140 m from the IP. The next detector system to be installed is the ALFA system, which consists of scintillating fibre trackers located at a distance of ± 240 m from the ATLAS IP. The most remote detector system is the FP420 system deployed at ± 420 m from the IP. The main physics aim of the FP420 project is to search for diffractive Higgs production.

In this thesis we will be concerned with two detectors in the forward region. The first is the LUCID gas Cerenkov luminosity monitor and the second is QUARTIC a high resolution time of flight (ToF) counter that we plan to

[1] At the time of writing an additional detector system has been proposed for deployment at ± 220 m from the ATLAS IP to operate in conjunction with the FP420 detector system. This development is not considered further in this thesis.

deploy as part of the FP420 project.

A dedicated luminosity monitor is a key feature of a collider experiment because in many cases, the precision of the calculated cross-section of the observed physics process is dominated by the resolution of the luminosity measurement [1]. LUCID the luminosity monitor for the ATLAS experiment due to be installed in the spring of 2008. It has been designed, constructed and will soon be installed by the LUCID collaboration, consisting the University of Alberta, the University of Bologna, CERN and Lund University. The LUCID detector will provide both online and offine luminosity monitoring and measurement.

In an exclusive pp process, both colliding protons stay intact after the collision, and travel down the beam pipe constrained by the beam magnet system. The FP420 group is planning to install proton detectors at ± 420 m from the interaction point, allowing the momentum of these protons to be measured, and the kinematics of the central state to be determined. In this way the FP420 detector system extends the physics reach of ATLAS. In order for the FP420 detector system to be useful at design luminosity ($10^{34}\,\mathrm{s}^{-2}\mathrm{cm}^{-2}$) a method is required to reduce background from pile-up events[2]. One method of reducing this background is to determine the vertex position of the protons in FP420 by precisely measuring the time of flight of the protons (to the order of 10's of picoseconds). QUARTIC is a time of flight detector designed for this purpose. Simulation and experimental studies show that its design based on a quartz Cerenkov counter will meet the requirements for FP420 background reduction.

Exclusive di-muon production via the two photon process $pp \rightarrow p\gamma\gamma p \rightarrow p\mu^-\mu^+ p$, where the $\mu^\pm$ are centrally produced, is a good candidate for calibration of the FP420 central mass measurement. This is due to the high resolution of the muon momentum measurement at ATLAS and adequate number of events available. A simulation study is carried out to test the efficiency of this calibration method.

The work reported in this thesis is divided into two parts: work related to the LUCID detector and work related to the FP420 detectors. In more detail:

[2] At high luminosity, multiple proton-proton collisions could take place at the same bunch crossing. These kinds of events are called pile-up events.

- Chapter 2 discusses the physics topics relevant to this thesis;
- Chapter 3 and Chapter 4 describe the ATLAS detector and FP420 detector;
- The fundamentals of luminosity measurement in ATLAS are introduced in Chapter 5.
- Chapter 6 to Chapter 8 set down the design, test beam and simulation study of LUCID as a luminosity monitor;
- Chapter 9 presents the simulation result of QUARTIC performance;
- Chapter 10 describes the calibration method of the FP420 detector;
- In the concluding chapter a brief summary of the major aspects of the thesis will be given paying particular attention to describing my contributions.

Chapter 2

Theory and Motivation

2.1 Standard Model

There are four known fundamental interactions (strong, weak, electromagnetic, and gravity) between the fundamental particles that make up all matter. The Standard Model [2] describes the fundamental particles and their interaction via the electromagnetic, weak and strong interactions. In the Standard Model, elementary particles can be divided into two categories: fermions with spin 1/2, 3/2, 5/2... and bosons with spin $0, 1, ...$ The fundamental fermions include quarks and leptons. Quarks carry both electric charge and colour charge, and interact via strong, weak and electromagnetic forces. Leptons, however, carry electric charge and weak charge, and thus interact via the electromagnetic and/or the weak force. The fundamental fermions are grouped into three generations with increasing mass as shown in Table 2.1.

	Generation 1	Generation 2	Generation 3
Quarks	Up Quark (u) Down Quark (d)	Charm Quark (c) Strange Quark (s)	Top Quark (t) Bottom Quark (b)
Leptons	Electron (e) Electron Neutrino (ν_e)	Muon (μ) Muon Neutrino (ν_μ)	Tau (τ) Tau Neutrino (ν_τ)

Table 2.1: *List of fermions.*

The fundamental bosons are force carrying particles. These bosons include the W and Z bosons of the weak force, eight coloured gluons of the strong

force, the photon of the electromagnetic force, and (in quantum gravity) the graviton of the gravitational force. Table. 2.2 shows the mediators of the three forces described in the Standard Model.

EM Force	Weak Force	Strong Force
Photon	W^+, W^- and Z^0 Gauge Bosons	Gluons (8)

Table 2.2: *Force Mediating Particles.*

According to the Standard Model the universe is permeated by a Higgs field with a non-zero vacuum expectation value (VEV). This VEV is constant and equal to 246 GeV. The particles of the Standard Model acquire mass by interacting with the Higgs field. In particular, the non-zero VEV of the Higgs field breaks the electroweak gauge symmetry, thus giving mass to the $W^{\pm}$ and Z gauge bosons whilst leaving the photon massless. This is called the Higgs mechanism [2]. The Higgs boson is the quantum of the Higgs field that has yet to be discovered. The Higgs boson mass is a free parameter in the Standard Model.

Although the Standard Model is in complete agreement with experiment, the Standard Model is not regarded to be a complete theory of the fundamental interactions, for the following reasons. First of all, the model contains a number of free parameters[1], which must be determined experimentally and cannot be calculated from the theory. It is difficult to believe that a theory with this many free parameters is truly fundamental. Second, the generation structure of the Standard Model does not arise from the theory. Third, why is the magnitude of the electron and proton charge exactly the same? Forth, why are the gauge interactions so different? Why is CP invariance broken? Other flaws in the Standard Model are its lack of a dark matter candidate and the fact that gravity cannot be incorporated into its structure.

A key particle of the Standard Model, the Higgs boson, is yet to be discovered experimentally. The Higgs boson mass is a free parameter in the Standard

[1]The free parameters include the masses of the 3 leptons and 6 quarks, 4 quark mixing parameters in the CKM matrix, coupling strengths for EM, weak and strong interactions, electroweak symmetry breaking (Higgs mass). If neutrinos are included, there are 3 extra neutrino masses, 4 mixing parameters and 2 extra phases if they are Majorana neutrinos.

Model. We can obtain meaningful constrains on the Higgs boson mass from electroweak (EW) precision measurements. These measurements are sensitive to EW radiative corrections at the next to leading order (NLO) and the next to NLO (NNLO) level and thus depend on the Higgs boson entering the loops. EW radiative correction measurements and upper limits can be set on the Higgs mass of 186 GeV with 95% confidence [3]. Theorists predict the highest possible mass scale allowed for the Higgs boson is around one TeV; beyond this point, the Standard Model becomes inconsistent because unitarity is violated in some processes [4]. The current lower limit on the Higgs mass is set by the LEP experiment to be 114.4 GeV/c^2, at the 95% condence level [5].

2.2 Physics at ATLAS

The search for the Standard Model Higgs boson is the main physics goal of the ATLAS experiment (see Chapter 3). Depending on the mass of the Standard Model Higgs particle, different discovery channels become available. The ATLAS detector allows us to cover the complete allowed mass range of the Higgs particle. Fig. 2.1 summarizes the sensitivity of ATLAS for the discovery of a Standard Model Higgs boson.

The LHC can also be used to search for the evidence of physics beyond the Standard Model, for example Supersymmetry (SUSY). In particle physics, supersymmetry is a symmetry that relates an elementary fermion to a "partner" boson with the same mass, or vice versa. Since the particles of the Standard Model do not have this property, supersymmetry must be a broken symmetry allowing the "sparticles" to be heavy. Supersymmetric particles, like the gluinos and squarks will be produced at the LHC if this kind of broken supersymmetry exists at the electroweak scale, and these particles will be detectable in ATLAS.

The general purpose LHC detector ATLAS will be an important tool for the precision measurement of the Standard Model parameters, for example, allowing precision mass measurements of the top quark, Z and W bosons. However, with high statistics, the challenge is to understand the systematic error of the detector.

The LHC physics program in general and of ATLAS, in particular, is de-

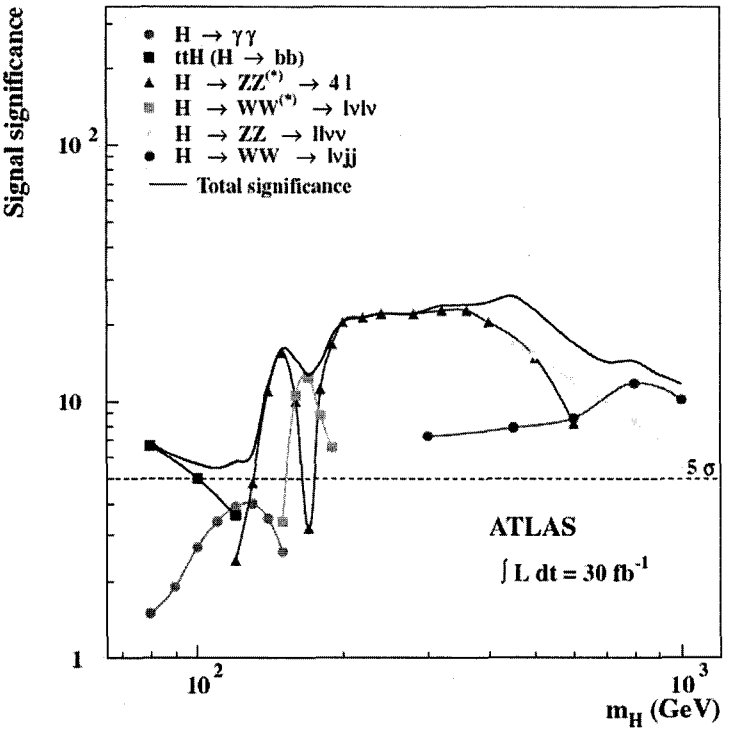

Figure 2.1: *ATLAS sensitivity for discovery of Higgs Boson after 1 year of running.*

scribed in reference [1, 6]. Traditionally the programs of collider detectors concentrate on high transverse momentum physics. In the following sub-section we will sketch aspects of the forward physics program at ATLAS that are relevant to this thesis.

2.3 Exclusive Interactions at Hadron Colliders

In the Standard Model, exclusive interactions, $pp \rightarrow pXp$, can take place via QED or QCD mediation. An example of the QCD mediated exclusive interaction is shown in Fig. 2.2 a), gluons are exchanged during the interaction and form a central system X. While in the QED mediated exclusive interaction, as shown in Fig. 2.2 b), photons are exchanged during the interaction and form a central system X. In both cases the protons remain intact during the interaction, losing only a small fraction of their momenta. Some of the de-

flected protons will travel along the beam line constrained in their trajectory by the beam line magnets. To detect these protons, detectors are planned to be installed in the available spaces 220 m [7] and 420 m [8] away from the interaction points (See Chapter 8). They are sensitive to the protons with a transverse energy loss smaller than several hundred GeV. Under the Regge limit, $s \gg M^2$ [9], the mass of the central system is much smaller than the collision energy, thus the transverse energy of the forward protons can be neglected and the central system energy can be determined by tagging the two forward protons.

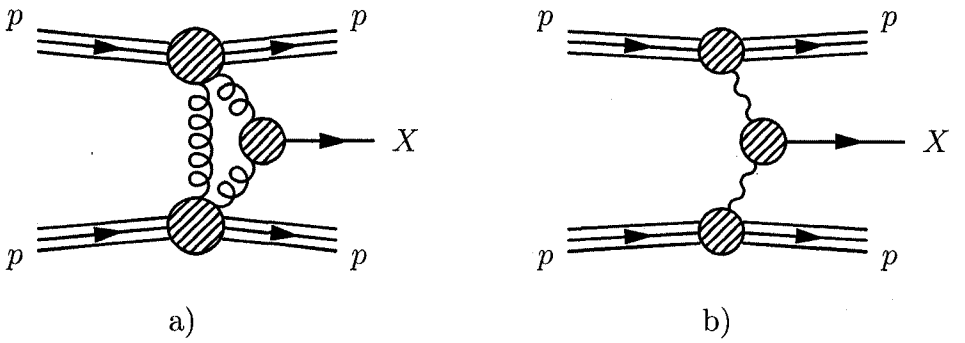

Figure 2.2: *a) QCD and b) QED mediated exclusive interactions, with X as a product. The shaded areas represent interactions that are not completely specified by the diagram.*

In exclusive interactions, since the two protons stay intact, there is a lack of hadronic activity in the detector forward regions forming a "rapidity gap" in the forward regions. Fig. 2.3 shows a proton-proton interaction where two protons exchange Pomerons[2]. The rapidity y is defined as [10]

$$y = \frac{1}{2} ln \frac{E + P_L}{E - P_L}, \tag{2.1}$$

where E is the energy of the particle and P_L is the longitudinal momentum ($P_L \equiv P_z$). In the massless limit, where the particle's energy is much larger

[2]The Pomeron is a force carrying quasi-particle introduced in 1961 in order to explain the energy behavior of soft hadronic collision at high energies. It appeared first in the framework of the Regge Theory of Strong Interactions at high energies, but later as an object derived from QCD calculations. It has been suggested that in perturbative QCD the lowest order prototype of the Pomeron is a colour neutral system of 2 gluons.

than the particle's mass, rapidity and pseudorapidity η are the same. The pseudorapidity η is defined as

$$\eta = -ln\left(tan\left(\frac{\theta}{2}\right)\right), \tag{2.2}$$

where θ is the angle of the particle momentum relative to the beam axis.

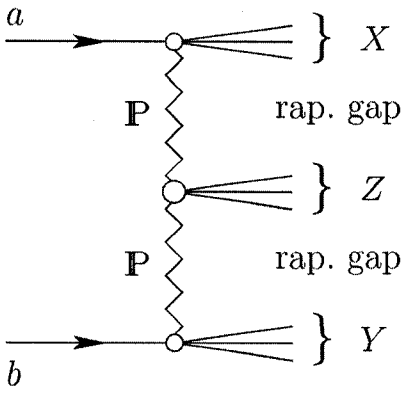

Figure 2.3: *A proton-proton interaction where the two protons exchange Pomerons, a central state and two rapidity gaps are produced. In the case of exclusive interactions, X and Y are intact protons.*

The rapidity gap signature can be used to veto non-exclusive interactions by means of a detector in the forward region (LUCID for example). This is called the rapidity gap trigger. However, in the case of high luminosity, because of the pile up of events, the rapidity gap is filled by the non-exclusive interactions that occur in the same beam crossing, so a rapidity gap trigger is not feasible.

2.3.1 Two-photon Physics (QED Exclusive Interactions)

In hadron colliders like the LHC, in addition to central collisions, it is also possible to study the very peripheral collisions where the hadrons interact via exchange of virtual photons [11]. Virtual photons arise from the electromagnetic field of the incoming beam particles. In this way, the hadron collider can be used as a photon collider.

The general Feynman diagram of the first order two-photon processes is shown in Fig. 2.2 b). Examples of two-photon lepton pair production and the

two-photon Standard Model Higgs boson production are shown in Fig. 2.4.

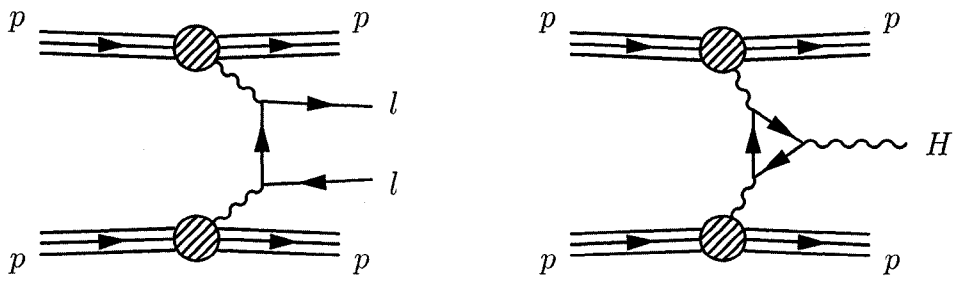

Figure 2.4: *a) Two-photon lepton pair production and b) two-photon standard model Higgs production.*

One can use the effective photon approximation (EPA) to describe two-photon interactions [12]. The idea of EPA is to factorize the $pp \to p\gamma\gamma p \to p+X+p$[3] into two steps: the emission of photons and the collision of photons, under the condition that the photons are quasi-real (virtuality of photons is low) [13]. So the cross-section for the process is factorized into and equivalent photon spectrum and the cross-section for the photon-photon collision process is

$$d\sigma_{TP} = \sigma_{\gamma\gamma\to X} dn_1 dn_2 \,, \tag{2.3}$$

$$\sigma_{TP} = \int \frac{d\omega_1}{\omega_1} n_1(\omega_1) \int \frac{d\omega_2}{\omega_2} n_2(\omega_2) \sigma_{\gamma\gamma\to X}(\sqrt{4\omega_1\omega_2}) \,, \tag{2.4}$$

where $\sigma_{\gamma\gamma\to X}$ is the cross-section for the corresponding photon-photon subprocess; $n(\omega_i)$ are the equivalent photon spectra for the incoming beams; ω_i are the energies of the photons; and $W = \sqrt{4\omega_1\omega_2}$ is the invariant mass of the outgoing system X. Based on the semiclassical impact parameter approach [14, 15], the equivalent photon flux can be written as:

$$n(\omega) = \frac{2\alpha Z^2}{\pi\xi} \left[\frac{\xi}{\xi_0} K_0 \frac{\xi}{\xi_0} K_1 \frac{\xi}{\xi_0} - \frac{1}{2} \left(\frac{\xi}{\xi_0} \right)^2 \left(K_1^2 \left(\frac{\xi}{\xi_0} \right) - K_0^2 \left(\frac{\xi}{\xi_0} \right) \right) \right] \tag{2.5}$$

where $K_{0,1}(\xi/\xi_0)$ are Bessel functions, $\xi_0 = 1/(RM_n) = \omega R/\gamma\beta$ and ξ is the fraction of the total momentum of each nucleus carried by the photons. The

[3] "+" denotes a rapidity gap.

variables R and M_n represent the radius and the mass of the colliding nuclei, respectively. There is a squared dependency upon the atomic number (Z) of the ion beam. Thus when the LHC is running in heavy ion mode, the photon interactions are enhanced due to the high ion charge [16]. Fig. 2.5 shows the effective two-photon luminosity at the LHC for the collision of different ion species as a function of the two-photon invariant mass [17]. Note that Fig. 2.5

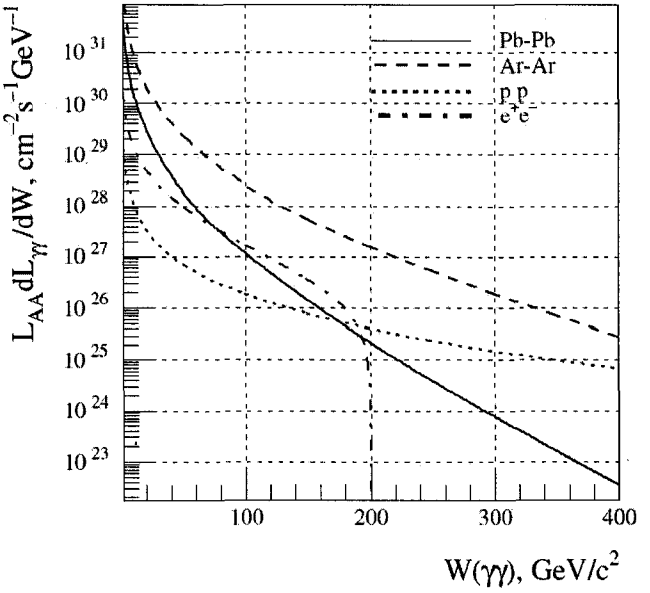

Figure 2.5: *Effective two-photon luminosities at the LEP and LHC for pp, $Ar-Ar$, $Pb-Pb$ collisions as a function of the two-photon invariant mass.*

also takes into account the different luminosities for different ion species. This is the reason why the two-photon luminosity for Ar-Ar is larger than Pb-Pb. The heavy ion luminosities are several orders of magnitudes smaller than the proton-proton luminosity.

Two-photon dilepton production (as shown in Fig. 2.4) has been studied in electron-positron [18], electron-proton [19] and hadron-hadron colliders [20].

Several programs exist to simulate this kind of processes. LPAIR [21] is the only one that contains the full matrix calculation. TPHIC [22] and DPEMC [23] are based on the EPA formalism. TPHIC does not include the small p_T of the outgoing protons. LPAIR and DPEMC are the two generators that are most suitable for simulating two-photon interactions at the LHC. LPAIR is used for event generation in this thesis.

2.3.2 QCD Mediated Exclusive Interactions

Theoretically, the QCD mediated exclusive interactions are very different from two-photon interactions. Fig. 2.2 a) shows a first order general Feynman diagram for this process. Each of the two incoming protons emit a gluon without disintegrating producing one central system by gluon fusion. At the same time, the two protons need to exchange a third gluon to balance the colour charge. This process can also be treated as a double Pomeron exchange process.

For a general case of exclusive diffractive production of a central system, the cross-section σ can be factorized into two parts:

$$\sigma = L(M^2, y) \times \hat{\sigma}(M^2), \tag{2.6}$$

where L is the effective gluon-gluon luminosity for a central system of mass M and rapidity y, and $\hat{\sigma}$ is the hard subprocess cross-section. This approach is described in detail elsewhere [24].

2.3.3 QCD Exclusive Higgs Production

The double diffractive higgs production, $pp \rightarrow p + H + p$ (where the + sign denote rapidity gaps) is shown in Fig. 2.6 . The Durham model of Khoze *et al.* [24, 25, 26, 27] uses perturbative QCD to calculate the cross-section for exclusive Higgs production in proton collisions. The amplitude for this process is that of gluon-gluon fusion through a virtual top quark loop. Gluon fusion is the dominant Higgs production mechanism at the LHC (Fig. 2.7).

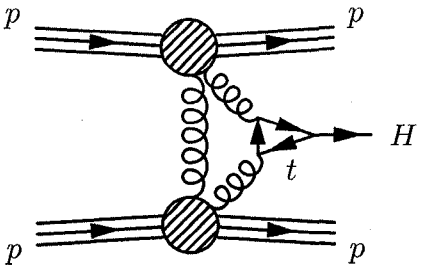

Figure 2.6: *QCD mediated central exclusive Higgs production.*

However, the basic model does not predict: a) the probability that the gluons in the hard subprocess will radiate, making the interaction non-exclusive and b) the probability that there is another soft interaction, independent of the diagram just calculated, that will make the interaction non-exclusive. The error from a) can be estimated and controlled by applying the Sudakov form factor [28]. However, the error from b), which is called the "soft survival factor" or the "gap survival probability", S^2, lies in the realm of non-perturbative QCD and is not calculable. It can only be determined from the previous experiments. This contributes the largest part of the uncertainty in the calculation [29].

Currently the Durham model prediction, with Sudakov and gap survival probability corrections, for the total exclusive cross-section at the LHC $\sigma =$ 3 fb for a Higgs of mass of 120 GeV, with a factor of 2 uncertainty [27].

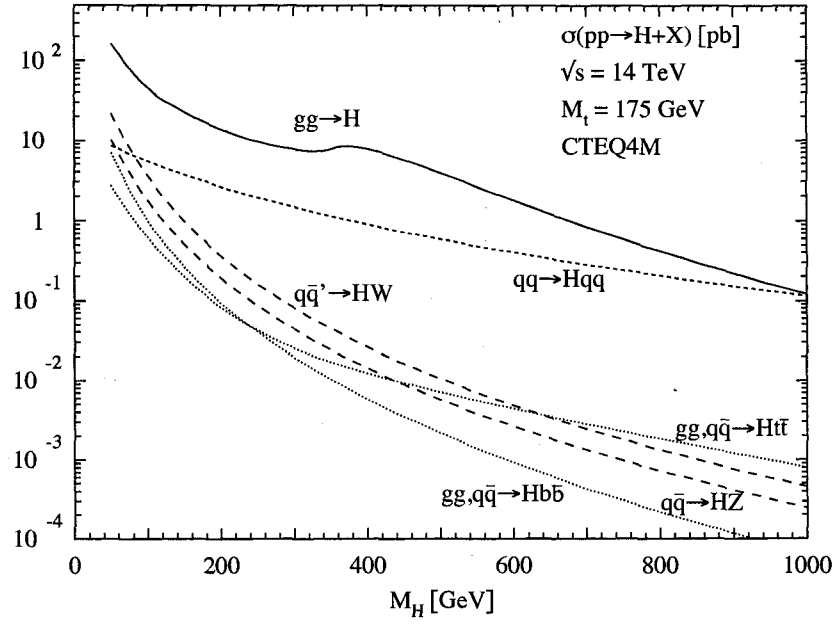

Figure 2.7: *Higgs production cross-sections at the LHC for the various production mechanisms as a function of the Higgs mass. The full QCD-corrected results for the gluon fusion $gg \to H$, vector boson fusion $qq \to VVqq \to Hqq$, vector boson bremsstrahlung $q\bar{q} \to V^* \to HV$ and associated production $gg, q\bar{q} \to Ht\bar{t}, Hb\bar{b}$ are shown. The QCD corrections to the last process are not known [30].*

ExHuME [28] is an event generator that implements the Durham model. In ExHuME, the factorization of the cross-section Eq. 2.6 is used, and the

effective gluon luminosity and the hard subprocess cross-section are calculated. A fixed gap survival factor of $S^2 = 0.01$ at LHC energy is used [25], which is based on experience from previous experiments. To simulate the observables of Higgs production in ExHuME, one can link to the program HDECAY [31] and to PYTHIA [32] for the decay of Higgs and then hadronization, respectively.

The cross section for exclusive Higgs production is calculated to be 3 fb for $M_H = 120$ GeV, falling to $\sim$ 1 fb at $M_H = 200$ GeV [24]. One of the cleanest channels in which to observe the Standard Model Higgs is the WW decay channel. For $M_H = 140$ GeV, 19 exclusive $H \rightarrow WW$ events with both protons tagged in 420 m or 220 m detectors (none using 220 m detectors alone) are expected, for an LHC luminosity of 30 fb^{-1} a year at $10^{33}\,\text{cm}^{-2}\text{s}^{-1}$. This rises to 25 at 160 GeV. Fifty percent of these events will be detected by the optimized trigger system in ATLAS and CMS.

Comparing to other Higgs search approaches, the exclusive Higgs production gives a mass resolution ($\sim 1\%$) that is hard to better. It also gives a large signal to background ratio and provides the possibility to study the quantum numbers of the Higgs boson, as is described in the next subsection.

2.3.4 Advantages of Exclusive Interaction

The QCD mediated exclusive process has two important properties. First, the mass of the central system, M_X, can be determined by measuring the momentum of the outgoing protons, $M_X^2 = (p_1 + p_2 - p_1' - p_2')^2$. Second, because of the spin selection rule of QCD, the central system X is preferentially produced with the quantum number of the vacuum, $J^{PC} = 0^{++}$.

The cross section in the Standard Model Higgs in the exclusive channel is small (3 fb for $M_H = 120$ GeV/c^2), and so it is an unlikely discovery channel for the Higgs in the LHC. However, compared to other Higgs channels, it has several advantages:

- By measuring the energy of the deflected proton, the Higgs mass can be measured to a resolution of ~ 2 GeV/c^2 [33], which is a better resolution than can be achieved in standard high-p_T running at ATLAS.

- Due to the spin selection rule, the QCD $b\bar{b}$ background is suppressed,

allowing the $H \to b\bar{b}$ branching ratio to be measured[4].

- The exclusive channel can provide a determination of the quantum numbers of the Higgs boson. The quantum numbers of the central object (in particular C- and P-parities) can be analyzed by studying the azimuthal angular distribution of the tagged protons [37]. This applies to different Higgs decay channels including $H \to b\bar{b}$, $H \to W^+W^-$, $H \to \tau^+\tau^-$, etc. Due to the selection rules, the production of 0^{++} states are strongly favored.

The cross-section of some QED mediated exclusive interactions can be precisely calculated. The process $pp \to p+l^+l^-+p$, especially di-muon production, can be used for luminosity determination in ATLAS (See Chapter 4).

By installing detectors in the very forward direction alone the beam pipe, FP420 [8] for example (See Chapter 8), the energy of the Pomeron-Pomeron and photon-Pomeron interactions can be determined and LHC can be used as a high luminosity photon-photon and Pomeron-Pomeron collider. The FP420 detector can also be used to detect the breakup of the proton and thus help to eliminate an important background to exclusive two proton processes arising from events where the breakup of one or both of the interacting protons would otherwise be unobserved.

[4]For forward outgoing protons the projection of the total angular momentum is $J_Z = 0$ along the beam axis. On the other hand, the Born amplitude for light fermion pair production vanishes in this $J_Z = 0$ state (see for example [34]). This result follows from P- and T-invariance and fermion helicity conservation of the $J_Z = 0$ amplitude [35]. Thus, if we were to neglect the b-quark mass m_b, then at leading order we would have no QCD $b\bar{b}$-dijet background at all [36].

Chapter 3

LHC and ATLAS

3.1 LHC

The Large Hadron Collider (LHC) [38] at the European Laboratory for Particle Physics (CERN) will, starting in 2008, collide protons at the unprecedented centre of mass energy of 14 TeV, with luminosity as high as $10^{34}\,\mathrm{cm}^{-2}\mathrm{s}^{-1}$. The energy densities created were only seen before just 10^{-12} s after the big bang, when the temperature was still 10^{16} K.

The LHC is housed in the 27 km circular underground tunnel originally used by the Large Electron Positron Collider (LEP). The LHC is the world's largest cryogenic system. To achieve the design energy, the LHC needs to cool 1232 dipole magnets to 1.9 K to enable the super-conducting magnets to achieve a field of 8.4 T. The counter rotating protons are accelerated in two different pipes sitting in a single yoke and cryostat (See Fig. 3.1). To focus the beam for collision at the IP, quadrupole magnets are used, which also work at 1.9 K to provide a field gradient of $\sim$ 200 T/m over a 70 mm aperture. A total of 96 T of helium is used to cool down the total cold mass of 37 000 T. Some basic machine and beam parameters are listed in Table. 3.1. The accelerating stages are shown in Fig. 3.2.

Four major experiments are deployed at the LHC, namely: two large multi-purpose detectors - ATLAS [39] and CMS [40]; the heavy-ion experiment ALICE [41]; and LHCb [42], which is dedicated to the study of b-quark physics. Beside the four major experiments, an additional experiment TOTEM will be installed to measure small angle scattering [43]. ATLAS and CMS are de-

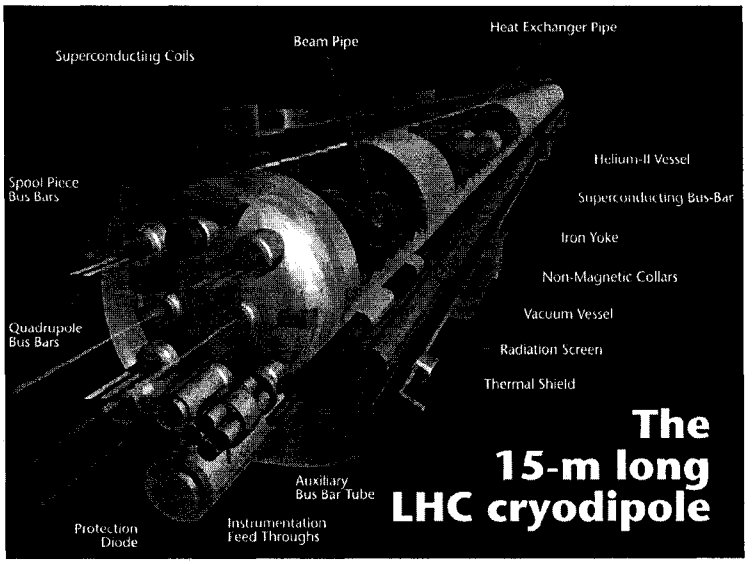

Figure 3.1: *Artist's impression of an LHC Cryodiple.*

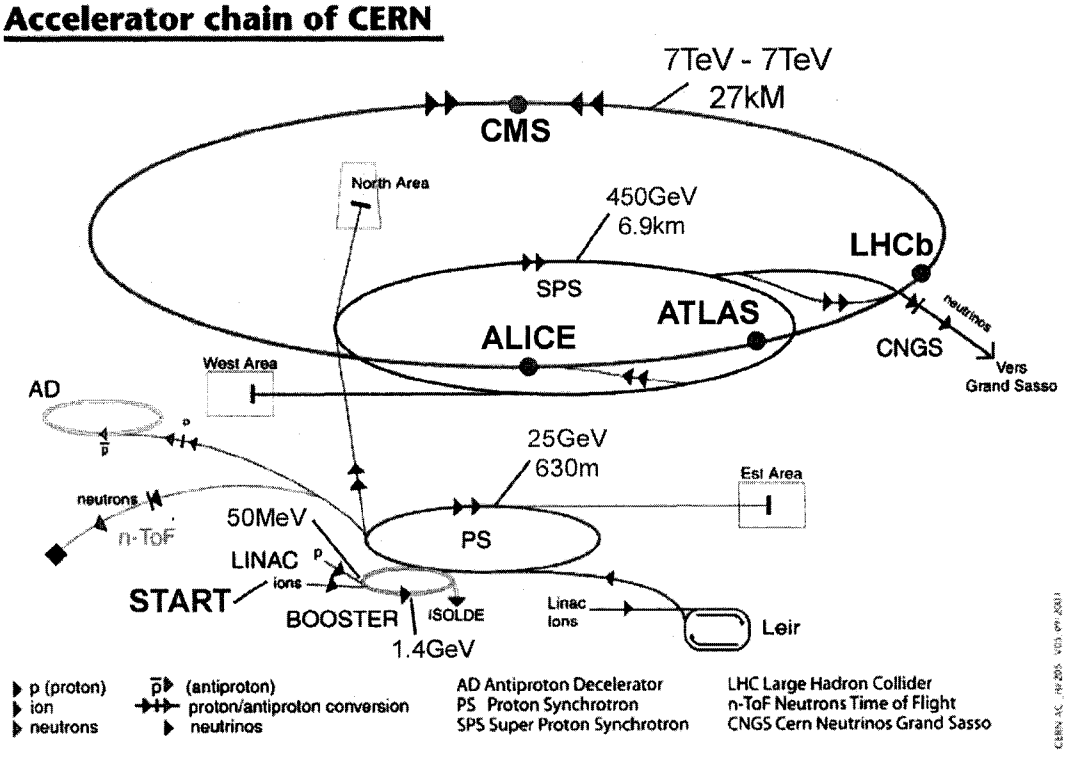

Figure 3.2: *LHC accelerator system at different stages, and the four detectors deployed (ATLAS, CMS, ALICE and LHCb) [38]. The circumference of each ring and the energy in each stage is also shown.*

Proton energy	7 TeV
Injection energy	450 GeV
Dipole field	8.4 T
Current at nominal field	11850 A
Luminosity	1034 $cm^{-2}s^{-1}$
Bunch spacing	25 ns
Particles per bunch	1011
Number of bunches	2808
Bunch length (r.m.s.)	7.5 cm
Inelastic cross-section	60 mb
Total cross-section	100 mb
Events per bunch crossing	19
Stored beam energy	362 MJ (equals to 80 kg of TNT)
Energy loss per turn	6.7 keV
Synchrotron radiation power per ring	3.6 kW

Table 3.1: *A few selected machine and beam parameters of LHC.*

signed to cover a wide range of physics in the Standard Model and beyond, while ALICE, LHCb and TOTEM have more specialized physics goals.

3.2 ATLAS

The ATLAS detector [1, 6] is a general purpose detector designed to investigate a wide range of known and hypothetical processes. Fig. 3.3 shows the overall design of ATLAS. The detector has a total length of 42 m and a radius of 11 m, and its total weight is about 7000 tons. It is designed to run at a luminosity as high as $10^{34}\,cm^{-2}s^{-1}$. ATLAS has the typical structure of a general purpose collider particle detector.

As shown in Fig. 3.4 and Fig. 3.5, the inner−most detectors surrounding the interaction points (IP) comprise the tracking system, which measures the trajectory of the charged particles. The tracking volume is permeated by a solenoidal magnetic field of magnitude 2 T. The momentum of the charged tracks traversing the tracking system is determined from their curvature in the magnetic field.

Surrounding the tracking system is the electromagnetic (EM) calorimetry, the purpose of which is to measure the energy of photons and electrons. Sur-

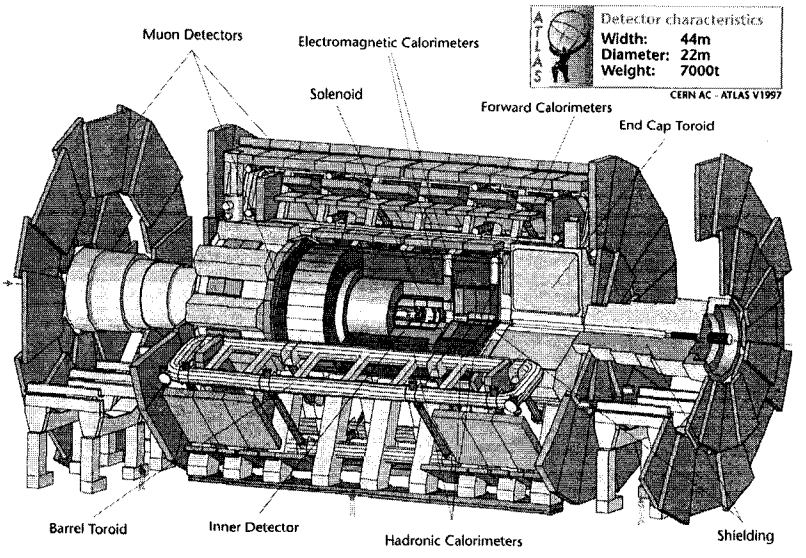

Figure 3.3: *A Drawing of the ATLAS Detector.*

rounding the EM calorimetry, the hadronic calorimetry is used to measure the energy of hadrons (K, n, $\pi^{\pm}$, p). Neutral hadrons (e.g. neutrons) can only be measured in hadronic calorimetry. The outer-most layer of ATLAS is the muon spectrometer, where the energy and momenta of the muons are determined.

3.2.1 Inner Detector

The ATLAS Inner Detector (ID) (See Fig. 3.6, [44, 45]) is the detector system closest to the interaction point. It is used to track and measure the momentum of charged particles. Around the vertex region are the silicon semi-conductor detectors, which include the Pixel Detector in the inner-most layer that has the highest granularity, and the Semi-conductor Counter (SCT) that encloses the Pixel Detector. A Transition Radiation Tracker (TRT) encompasses the SCT providing continuous tracking and particle identification with lower material budget.

The whole ID is contained in a cylindrical envelope with outer radius 115 cm and total length 7 m. The ID is deployed within a 2 T solenoid magnetic field. A list of ID components and their typical measurement resolutions is given in Table. 3.2.

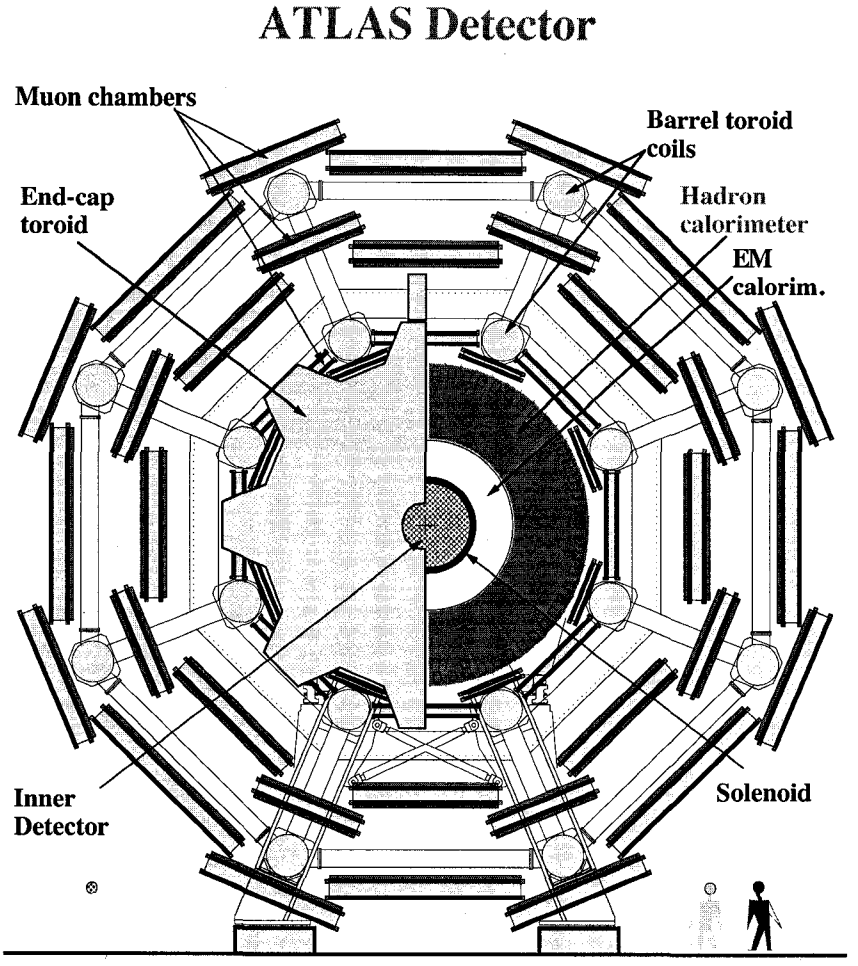

Figure 3.4: *Cross Section of the ATLAS Detector in X-Y Plane.*

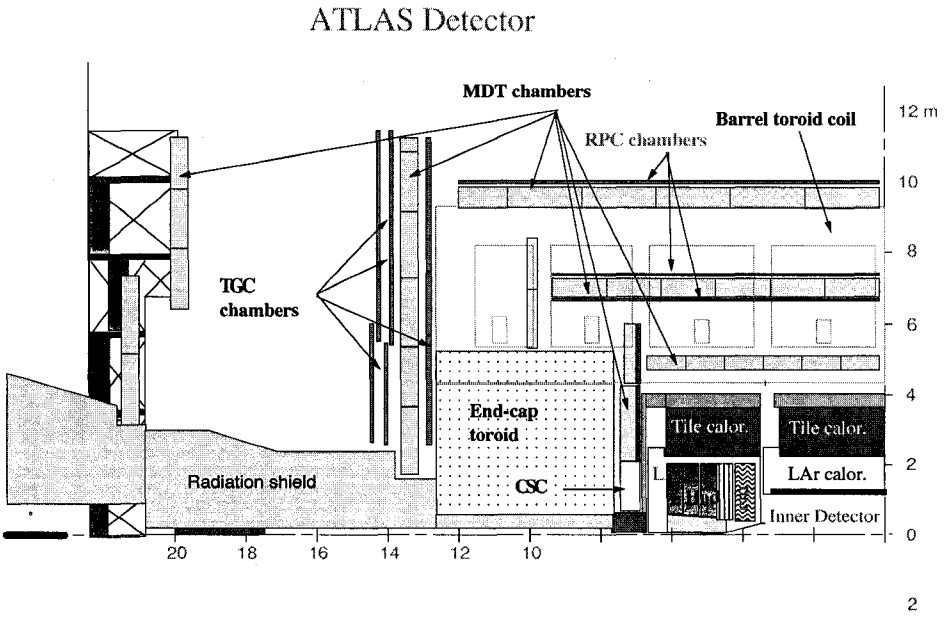

Figure 3.5: *Cross section of the ATLAS detector in R-Z plane.*

The fine-granularity detectors provide high resolution measurements of particle position, thus allowing the precise determination of charged particle trajectories, impact parameter, and vertex position, which is crucial for identifying heavy flavour decays.

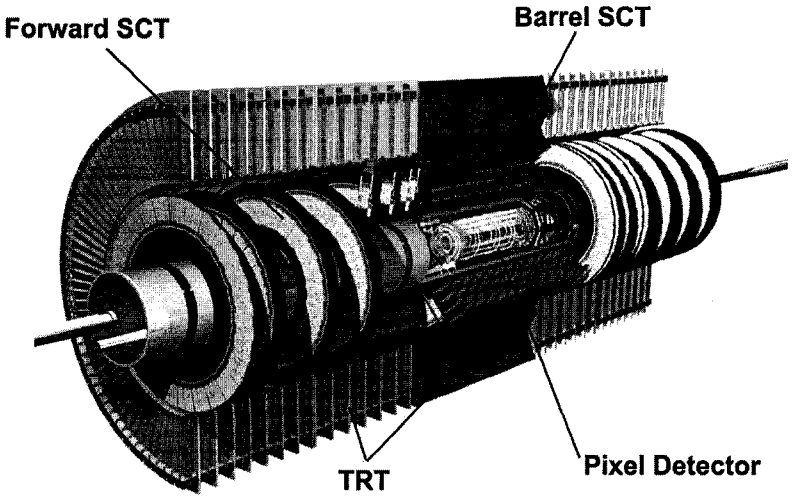

Figure 3.6: *Artistic drawing of the ATLAS inner detector.*

System	Position	Area (m^2)	Resolution $\sigma(\mu m)$	Channels (10^6)	Coverage $\|\eta\|$
Pixels	1 removable barrel layer	0.2	$\sigma_{R\phi} = 12$, $\sigma_Z = 66$	16	2.5
	2 barrel layers	1.4	$\sigma_{R\phi} = 12$, $\sigma_Z = 66$	81	1.7
	5 end-cap disks per side	0.7	$\sigma_{R\phi} = 12$, $\sigma_R = 77$	43	1.7-2.5
SCT	4 barrel layers	34.4	$\sigma_{R\phi} = 16$, $\sigma_Z = 580$	3.2	1.4
	9 end-cap disks per side	26.7	$\sigma_{R\phi} = 16$, $\sigma_R = 580$	3.0	1.4-2.5
TRT	axial barrel straws		170 (per straw)	0.1	0.7
	radial end-cap straws		170 (per straw)	0.32	0.7-2.5

Table 3.2: *Inner Detector components and their corresponding typical measurement resolutions.*

Pixel Detector

The Pixel Detector [46] system provides three 3D position measurements over the rapidity range $|\eta| < 2.5$. The detector consists of 3 barrels and 6 disks (3 on each side), all the barrels and disks are composed of 6.4 cm $\times$ 2.1 cm pixel modules. Each pixel module contains 47268 pixel elements. The inner barrel

layer covers a rapidity range $|\eta| < 2.5$. The other two layers cover $|\eta| < 1.7$, the three end-cap disks are used to provide additional space points in the forward regions covering $1.7 < |\eta| < 2.5$. The accuracy of the position measurement in the barrel layers is 12 μm in $R - \phi$ and 66 μm in z. The accuracy of the end-cap layers are 12 μm in $R - \phi$ and 77 μm in R. Where R denotes the radial coordinate and ϕ the zenith coordinate. A picture of the Pixel Detector is shown in Fig. 3.7 (top).

Semiconductor Tracker (SCT)

The SCT utilizes silicon technology as in the Pixel Detector, however, layers of silicon strip detectors are used. The strips are 12 cm long. The SCT covers a large area (60 m^2) with a relatively small number of readout channels compared to the Pixel Detector. It consist of 4 nested barrel layers and 9 end-cap disks (each side).

The barrel layers cover $|\eta| < 1.4$ with accuracy 16 μm in $r - \phi$ and 580 μm in z. While the end-cap disks cover $1.4 < |\eta| < 2.5$ with accuracy 16 μm in $r - \phi$ and 580 μm in R. Fig. 3.7 (middle) shows a picture of SCT.

Transition Radiation Tracker (TRT)

The TRT consists of straw detectors, giving 36 points per track from radii between $\sim$ 50 cm and $\sim$ 100 cm. It consists of 36 layers of straw tubes each with 4 mm diameter. Each straw functions as a drift tube, with a gas mixture $Xe : CO_2 : O_2 = 70/27/3$, for measuring the position of a track and as an ionization chamber for recording the amplitude of the signals. The straw tubes are embedded in radiator material consisting of polypropylene foam/fibres. X-rays are produced when the charged particle crosses the multiple radiator-air boundaries. The straw detects x-ray photons arising from the transition radiation effect in the radiator material.

The TRT consists of 1 barrel module and 2 end-cap modules. In the barrel module the straws are arranged axially while in the end-cap modules the straws are arranged radially. Fig. 3.7 (bottom) shows the two end-cap modules.

The barrel module provides a rapidity range of $|\eta| < 0.7$, the end-cap modules cover $0.7 < |\eta| < 2.5$. They provide a position measurement with an

accuracy of ~ 200 μm per straw.

An important function of the TRT is particle identification, mainly the separation of electrons and pions [47]. For example, for an electron efficiency of 90%, the measured pion efficiency is about 1.2%, i.e. a rejection factor of 75 is achieved against 20 GeV pions in a magnetic field of 0.8 T.

3.2.2 Magnet System

ATLAS has two magnet systems, a sketch of the ATLAS magnet systems is given in Fig. 3.8. The first is a cylindrical solenoid coil (CS) with a 2 T field placed around the Inner Detector. The position in front of the EM calorimeter requires careful minimization of material used to reduce showering before the calorimetry. A picture of the CS is shown in Fig. 3.9

In the muon spectrometer there is one barrel toroidal magnet (BT) and two endcap toroidal magnets (ECT). Each toroid consists of 8 coils assembled symmetrically around the beam axis, as shown in Fig. 3.8. The BT coils are integrated into individual cryostats as shown in Fig. 3.9 (bottom-left), while the ECT toroids are placed into one large cryostat. A picture of one ECT module is shown in Fig. 3.9 (bottom-right). The peak magnetic field on the superconductors in BT and ECT are 3.9 T and 4.1 T respectively. The total weight of the toroid magnet is more than 1300 tons.

Both CS and BT magnets are super-conducting coils that are cooled by helium to a working temperature of 4.5 K. A field map of ATLAS is shown in Fig. 3.10.

3.2.3 Calorimeter

In ATLAS, the calorimeter system consists of EM calorimeters, the surrounding hadronic calorimeters and the forward calorimeters, as shown in Fig. 3.11. The EM calorimetry includes a Liquid Argon Barrel EM calorimeter which covers the pseudorapidity region $|\eta| < 1.475$, and a Liquid Argon End-Cap Calorimeter (EMEC) which covers $1.375 < |\eta| < 3.2$. The hadronic calorimetry includes a Hadronic Tile Barrel Calorimeter which covers $|\eta| < 1.7$, and Hadronic Liquid Argon End-cap Calorimeter which covers $1.5 < |\eta| < 3.2$. The Liquid Argon Forward Calorimeter (FCAL) covers $3.1 < |\eta| < 4.9$.

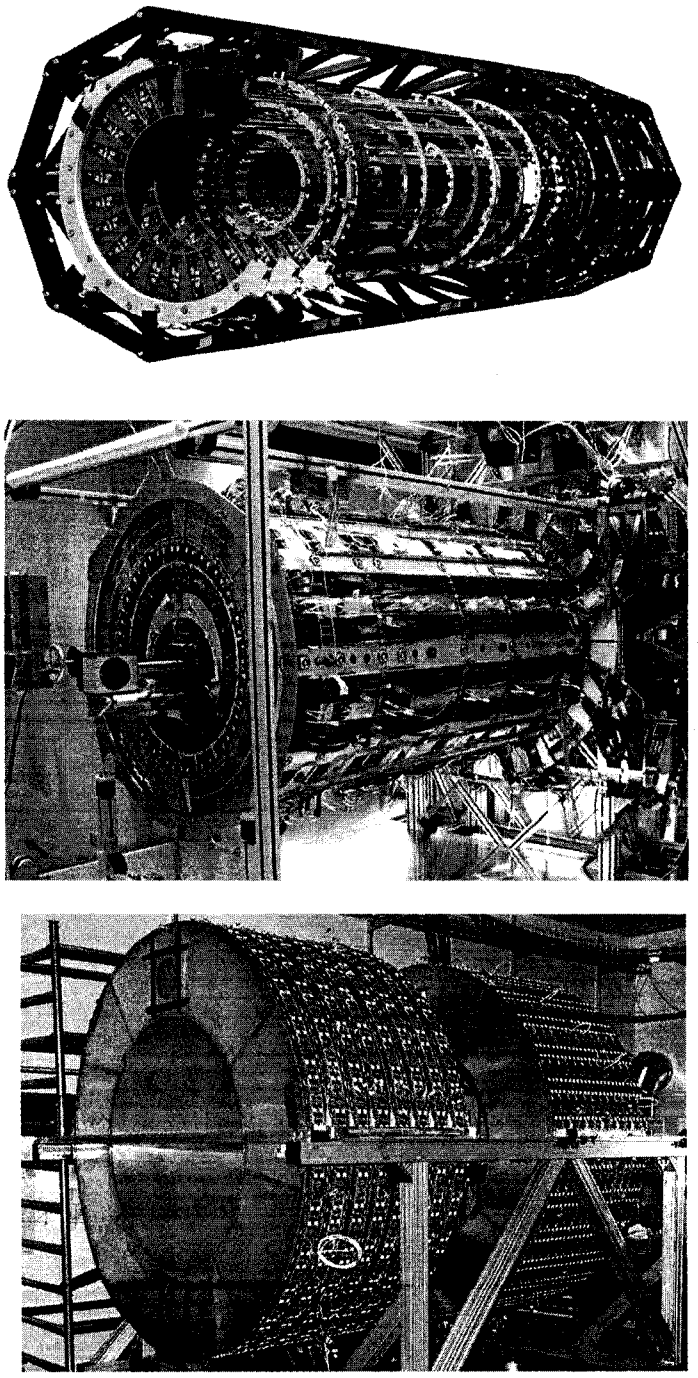

Figure 3.7: *The ATLAS Pixel Detector (top), Semiconductor Tracker (middle) and Transition Radiation Tracker (bottom). The dimensions of these detectors is given in Fig. 3.5.*

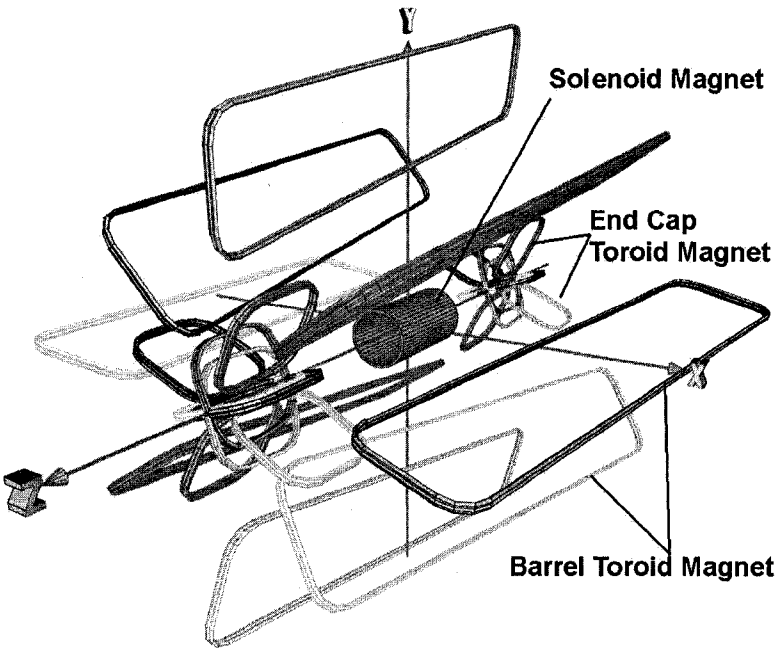

Figure 3.8: *Scheme of ATLAS magnet system.*

The energy resolution of a sampling calorimeter can be parameterized as follows:

$$\frac{\sigma(E)}{E} = \frac{a}{\sqrt{E}} \oplus \frac{b}{E} \oplus c, \tag{3.1}$$

where the constants a, b and c depend on stochastic fluctuations, electronic noise and non-uniformity, respectively.

EM Calorimeter

The ATLAS EM Calorimeter [48] consists of one barrel module and two end-cap modules. All modules are high-granularity Liquid Argon Calorimeters. The electromagnetic shower develops in the lead absorber plates. The thickness of the absorber plates is 1.5 mm in the barrel and 1.7 mm and 2.2 mm in the first and second end-cap wheel. The absorbers are folded into an accordion shape and oriented along R (z in the end-caps) to provide complete ϕ symmetry without azimuthal cracks, as shown in Fig. 3.12.

The thin (2-6 mm) gaps are filled with liquid argon and equipped with multiple electrodes in which the charge resulting from the ionization energy loss of the charged components of the shower (electrons and positrons) is read

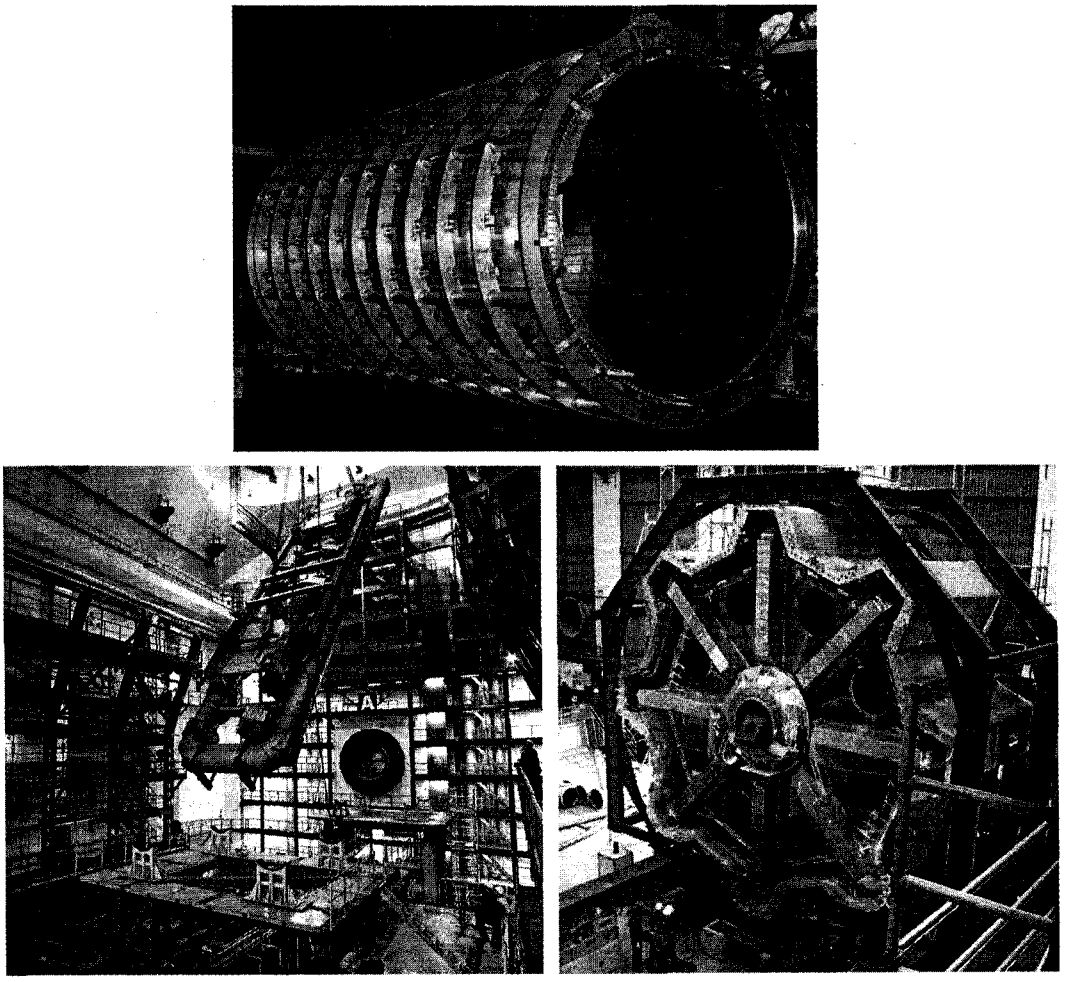

Figure 3.9: *Central Solenoid Magnet (top), a module of the Barrel Toroid Magnet (bottom-left) and the End-Cap Toroid Magnet (bottom-right).*

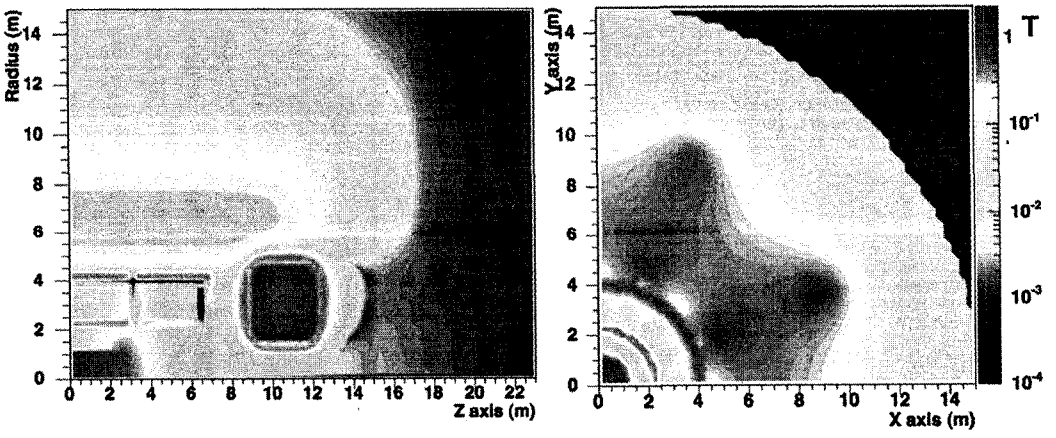

Figure 3.10: *ATLAS magnet field map in Z-R (left) and in X-Y (right).*

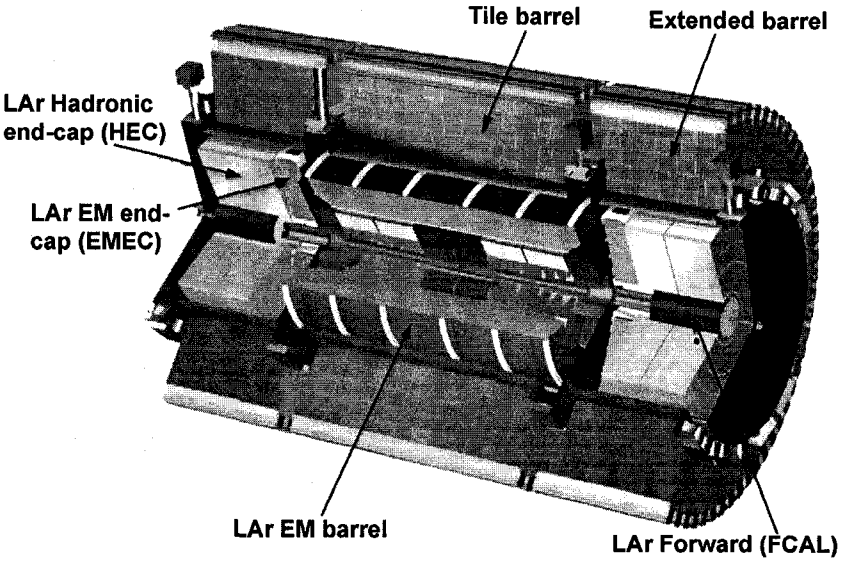

Figure 3.11: *Cut away drawing of ATLAS calorimetry.*

out. The total EM Calorimeter presents 24 (26) radiation lengths in the barrel (end-caps) region to reduce the error in the energy resolution, and to minimize the leakage of particles to the next layer.

Testbeam results on the EM barrel and end-cap give a combined resolution for electromagnetic showers of [49]:

$$\frac{\sigma(E)}{E} = \frac{10\%}{\sqrt{E}} \oplus \frac{400\,\mathrm{MeV}}{E} \oplus 0.7\%. \tag{3.2}$$

Fig. 3.13 shows a photo of the ATLAS barrel and end-cap EM calorimeters, during construction.

Hadronic Calorimeter

The hadronic calorimeter in the barrel region [50] utilizes iron absorbers with scintillator plates, as shown in Fig. 3.14 (top). The scintillation light generated by the particles in the hadronic shower is collected by wavelength-shifting fibers on both sides of the scintillator and is sent to two separated photo-multiplier tubes. The cells are grouped in bundles to form readout cells of the desired segmentation ($\Delta\eta \times \Delta\phi = 0.1 \times 0.1$). Fig. 3.14 (bottom) is a photo of one wedge of Tile Calorimeter. The Tile Barrel Calorimeter lies outside of the EM

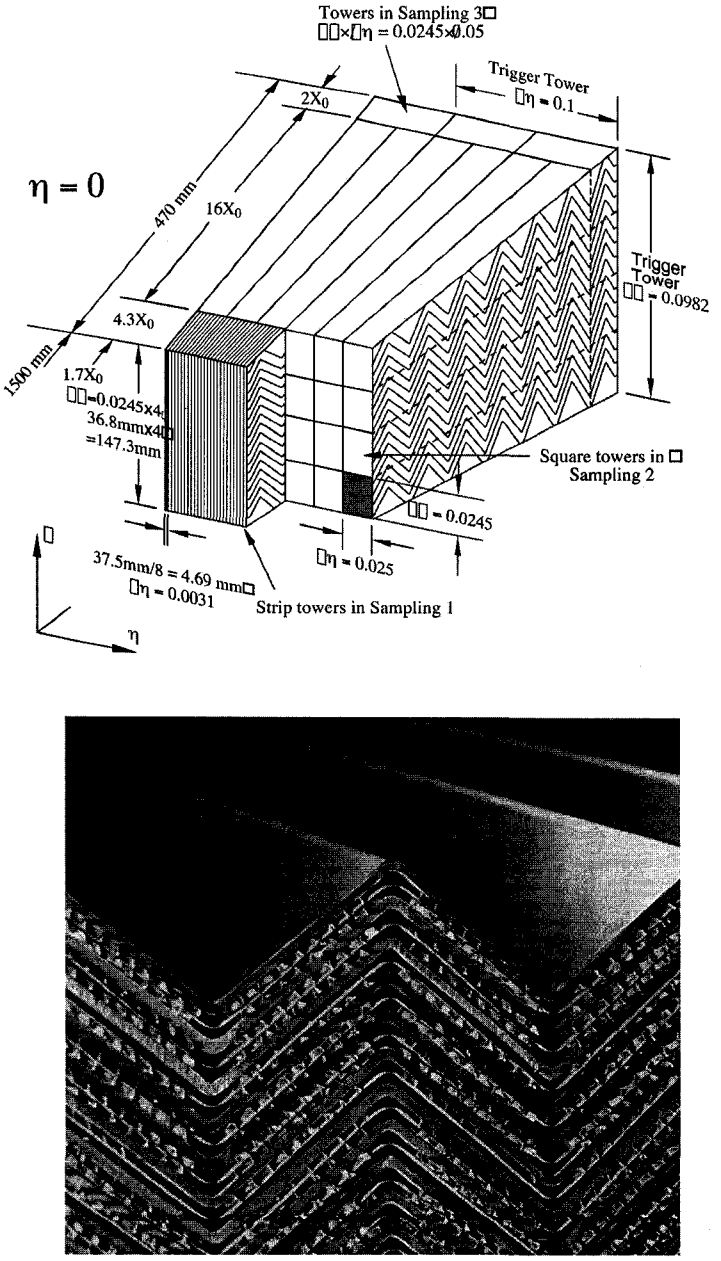

Figure 3.12: *Sketch of the EM calorimeter (top) and a picture of the accordion shape of EM calorimeters (bottom).*

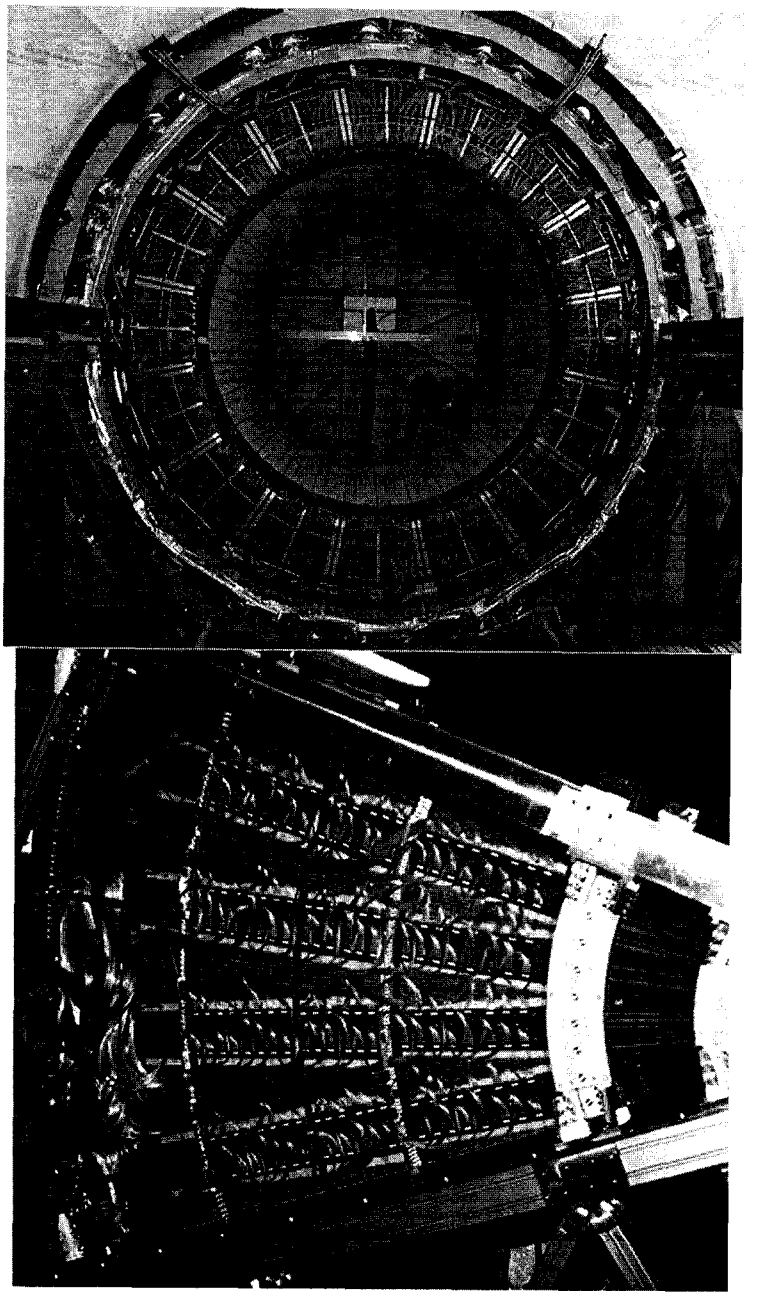

Figure 3.13: *The liquid Argon EM barrel (top) and one module of theend-cap (bottom) calorimeter.*

barrel between a radius of 2.28 m and 4.23 m, covering the pseudorapidity range $|\eta| < 1.6$. Each of the three cylinders of the tile calorimeter (one barrel and two extended barrels), is composed of 64 wedges in the azimuthal direction with a granularity in $\eta \times \phi$ of 0.1×0.1, providing 9.5 interaction lengths of depth.

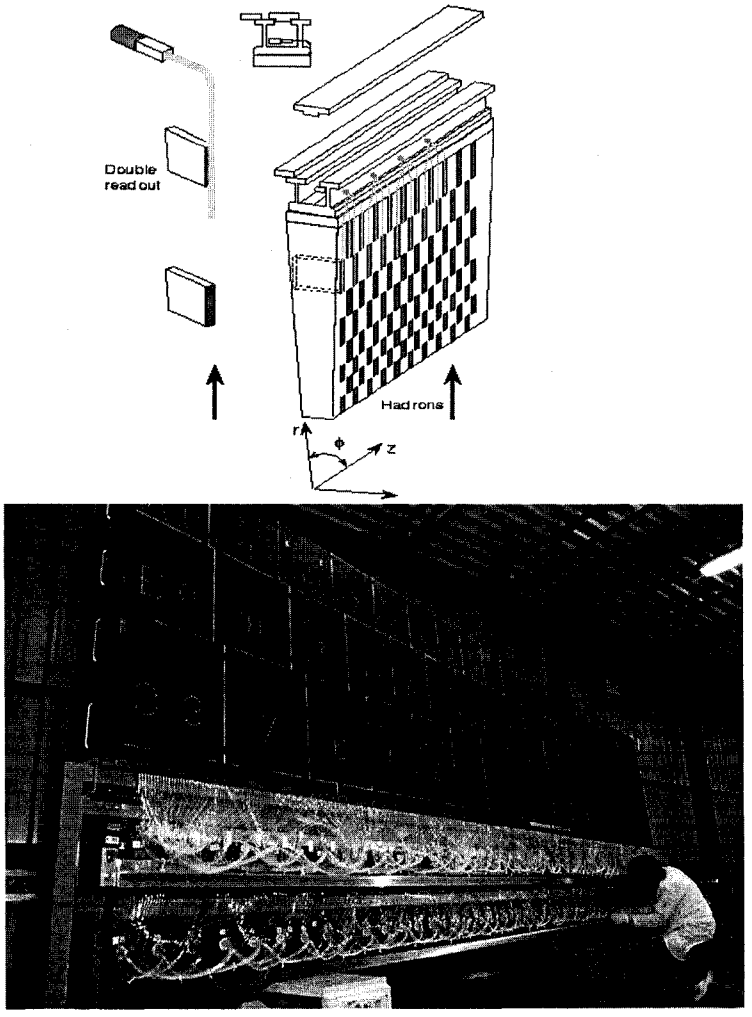

Figure 3.14: *The hadronic tile barrel calorimeter.*

The End-Cap Liquid Argon Hadronic Calorimeter is a liquid argon/copper sampling calorimeter. Covering a pseudorapidity range of $1.5 < |\eta| < 3.2$, it is 10 radiation lengths deep. Each End-Cap consists of two separate wheels containing 32 modules, as shown in Fig. 3.15 (top). The wheel closest to the IP has flat 25 mm thick copper plates, separated by 8.5 mm liquid argon gaps,

which the second wheel implements 50 mm thick plates. The granularity of the Hadronic End-Cap is 0.1×0.1 up to a pseudorapidity value of $|\eta| = 2.5$.

The expected energy resolution combining the Barrel and Hadronic End-Cup calorimeters is [50]

$$\frac{\sigma(E)}{E} = \frac{50\%}{\sqrt{E}} \oplus \frac{3\%}{E}. \tag{3.3}$$

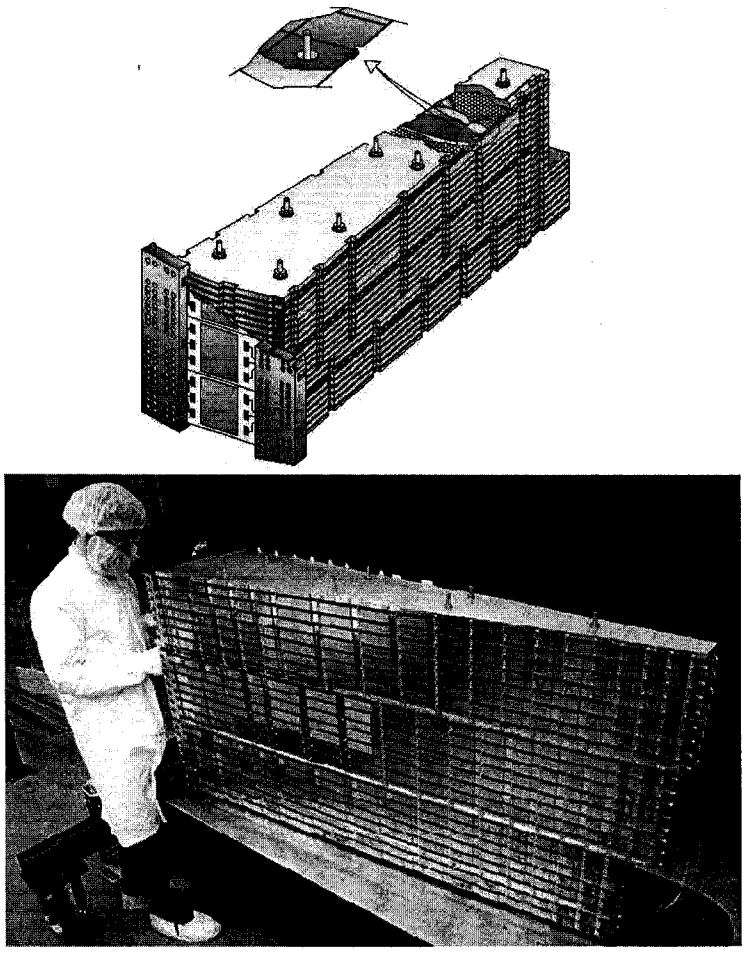

Figure 3.15: *The liquid Argon end-cap hadronic calorimeter module.*

Forward Calorimeter

The Forward Calorimeter (FCAL, [49]) also utilizes liquid argon technology. However, the configuration of the detector is very different from EM and hadronic end-cap calorimeters.

The FCAL is composed of three modules: the electromagnetic (FCAL1) and two hadronic modules (FCAL2 and FCAL3). The FCAL1 module is of copper composition and the hadronic modules of tungsten and sintered tungsten alloy. These three modules, together with a copper passive shielding plug are positioned within the forward tube structure of the end-cap cryostat as shown in Fig. 3.16. Structurally, the FCAL modules consist of single absorber matrix bodies carrying an array of tube electrodes in holes in the matrix bodies. Fig. 3.17 (left) shows the layout of the copper absorber matrix of FCAL1 module. Fig. 3.17 (right) shows a picture of the FCAL1 module.

The electrodes consist of a rod (with a signal pin inserted in one end) inside an outer tube such that there is a cylindrical shell gap of liquid argon between the two. Centring of the rod in the tube is done by means of a polyimide-coated quartz fibre wound onto the rod (prior to insertion in the tube) in a single helical pattern.

The EM module FCAL1 uses copper absorber matrix while the two Hadronic modules FCAL2 and FCAL3 use tungsten absorber matrix. The modules are each 28, 91 and 89 radiation lengths in depth and provide nearly 2.7, 3.7 and 3.6 interaction lengths. The FCAL covers an angular range $3.2 < |\eta| < 4.8$, with granularity approximately 0.2×0.2.

The expected energy resolution of the FCAL is [49]

$$\frac{\sigma(E)}{E} = \frac{100\%}{\sqrt{E}} \oplus \frac{10\%}{E} \tag{3.4}$$

3.2.4 Muon System

The ATLAS Muon System is important because many physics processes of interest involve the production of muons. In the decay of the Higgs boson, for example, a significant number of events involve muons in the final state, as shown in Fig. 2.1, therefore the identification of muons provides an important signature for event selection, and is crucial for triggering. Furthermore, the accurate determination of the momentum of the muons allows the precise reconstruction of events that have muons in their final state.

Fig. 3.18, Fig. 3.4 and Fig. 3.5 show the layout of the muon spectrometer. In the barrel region, tracks are measured in chambers arranged in three cylin-

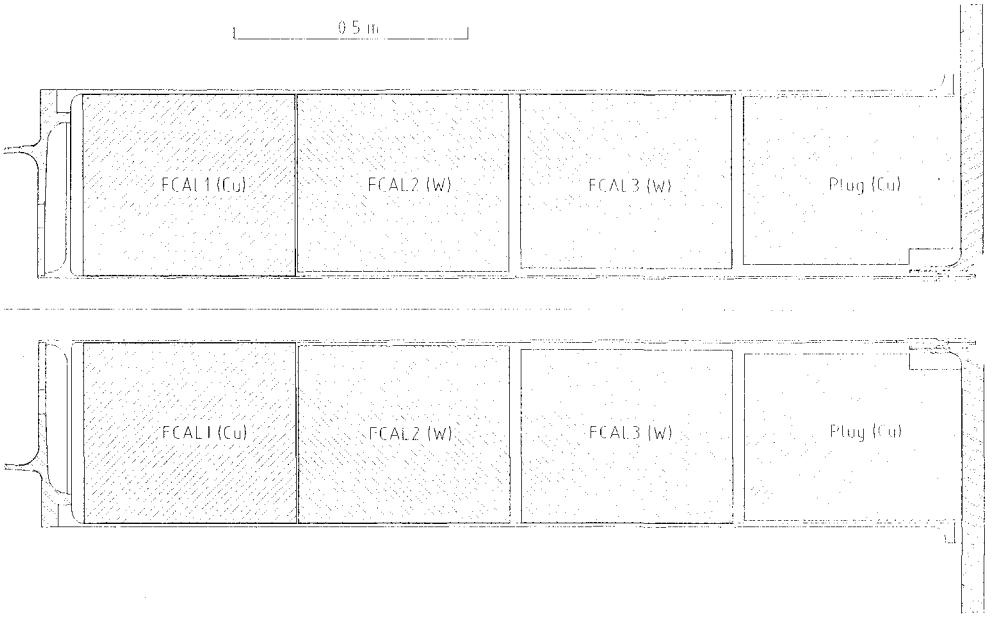

Figure 3.16: *The ATLAS FCAL (vertical section along the beam line axis, particles incident from the left).*

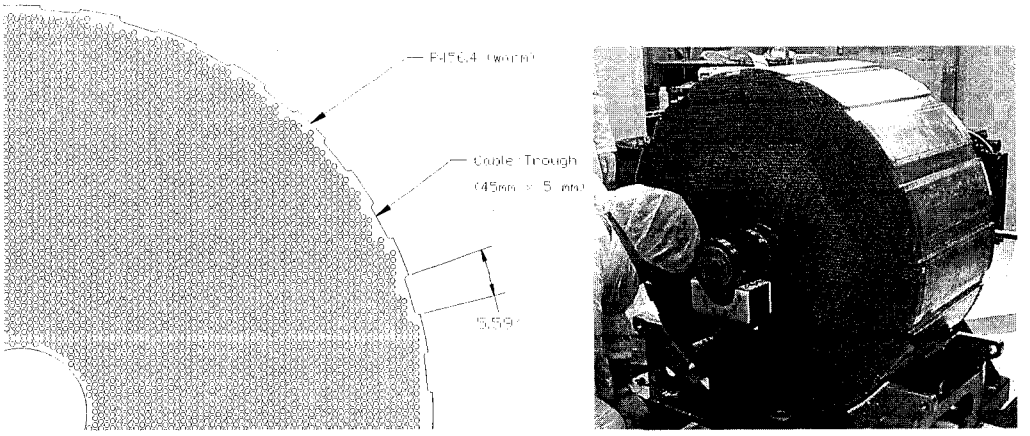

Figure 3.17: *Left: FCAL1 absorber plate (quadrant view); Right: Picture of one copper module of the liquid Argon forward calorimeter.*

drical layers (stations) around the beam axis. In the transition and end-cap regions, the chambers are installed vertically, also in three stations. Over most of the pseudorapidity range ($|\eta| < 2.7$), a precision measurement of the track coordinates in the principal bending direction of the magnetic field is provided by Monitored Drift Tubes (MDTs). At large pseudorapidities ($|\eta| > 2.7$) and close to the interaction point, Cathode Strip Chambers (CSCs) with higher granularity are used to sustain the demanding rate and background conditions.

The trigger system covers the pseudorapidity range $|\eta| < 2.4$. Resistive Plate Chambers (RPCs) are used in the barrel and Thin Gap Chambers (TGCs) in the end-cap region.

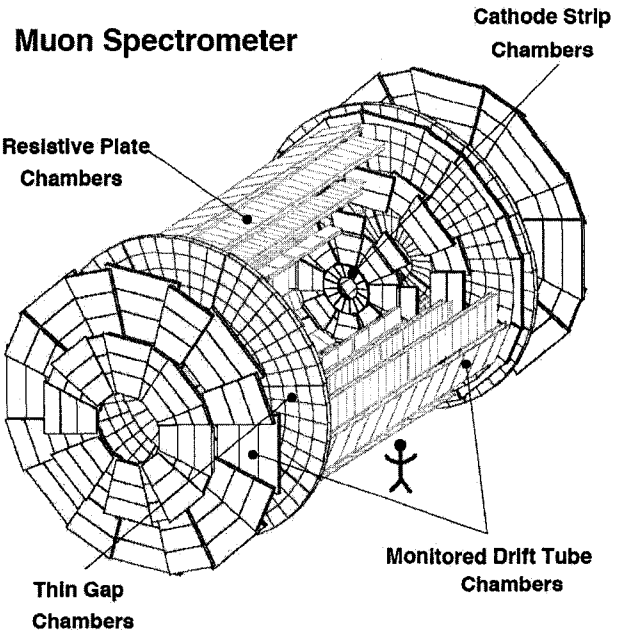

Figure 3.18: *Artistic Drawing of ATLAS muon system.*

The Monitored Drift Tube Chambers cover the area near 5500 m^2 with rapidity range $|\eta| < 2.7$. The basic detection element is a cylindrical aluminium drift tube of 30 mm diameter and a W-Re central wire of 50 μm diameter. A gas mixture of $Ar/N_2/CH_4$ (91%/4%/5%) with 3 bar absolute pressure fills the tube. A voltage difference of 3270 V is applied between the wire and tube to provide the electric field required to allow the drifting of ionization electrons. Each single tube provides an average spatial resolution of 80 μm. To obtain such precision with a lightweight construction the chambers are assembled on

their support or spacer frame using precision mechanics during production. Their deformations are monitored by built-in optical systems once they have left the flat granite table on which they were assembled.

The CSCs are multiwire proportional chambers with a symmetric cell in which the anode-cathode spacing d is equal to the anode wire pitch S, which has been fixed at 2.54 mm in view of the required performance (Fig. 3.19). The cathode readout pitch W is 5.08 mm. In a typical multiwire proportional chamber the anode wires are read out limiting the spatial resolution. In CSC, the precision coordinate is obtained by measuring the charge induced on the segmented cathode by the avalanche formed on the anode wire. The spacial resolution provided by CSC is 40 μm in the bend plane (when 4 points of the track are detected), and 0.5 cm in the azimuthal direction.

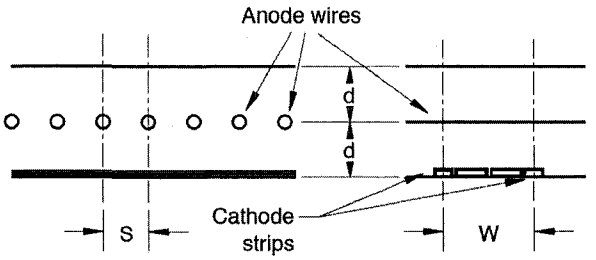

Figure 3.19: *Schematic diagram of the cathode strip chamber.*

The TGCs has similar structure to the traditional Multi-Wire proportional Chambers (MWPCs), except that the anode-to-anode distance (the wire to wire distance) is bigger than the anode-to-cathode distance. A schematic description of the TGC is shown in Fig. 3.20. The gas mixture used in the TGCs is CO_2 / $n-C_5H_{12}$ (55%/45%). TGCs provide the muon trigger capabilities in the end-cap modules, as well as the azimuthal coordinate to complement the coordinate measured by MDTs.

RPCs provide trigger signals for the barrel region. RPCs are composed of two high resistance plates with gas mixture in the thin (several mm) gap. A high voltage around 10 kV is applied between the two plates. When a muon travels across the gas, the avalanche electrons travel to one of the resistive plates and a current is induced in the readout strip attached to it. The ATLAS RPCs work in the avalanche mode. Tetrafluoroethane ($C_2H_2F_4$) is used in

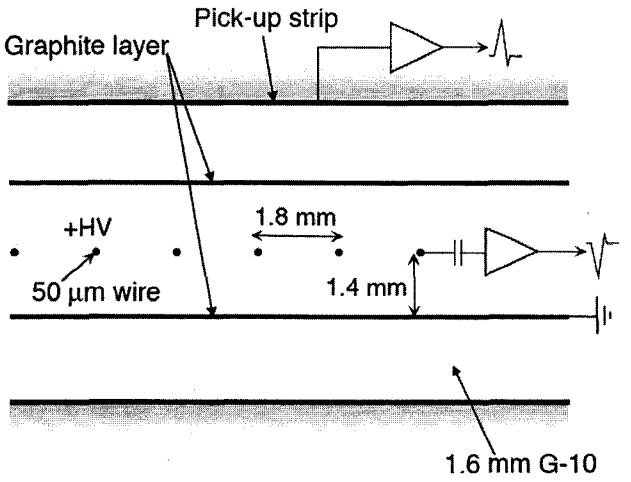

Figure 3.20: *Schematic diagram of the thin gap chamber.*

the RPCs. The space-time resolution of RPCs is of the order of 1 cm×1 ns including the performance of the digital readout. This resolution is needed in order to fulfill the requirements of the ATLAS trigger system.

3.2.5 ATLAS Trigger System

The LHC will run at a maximum luminosity of $10^{34}\,\mathrm{cm}^{-2}\mathrm{s}^{-1}$ and a 40 MHz beam crossing rate, giving around 10^9 interactions per second. Most events are inelastic pp collisions. The trigger system is designed to enhance high-p_T events for "hard" (quark-quark) interactions. The trigger system must make a decision in a very short time to match the high interaction rate. In order to do this, the ATLAS trigger system is designed in three levels, as shown in Fig. 3.21.

The first level trigger (LVL1) decision is based on information of two sub-detector systems, the muon system (trigger chambers only) and the calorimetry. In the decision process the LVL1 utilizes the estimated transverse momentum of muon candidates, the total energy deposited in the calorimeters, the missing (transverse) energy in the calorimeters and the occurrence of isolated energy depositions in the calorimeters. The LVL1 trigger is designed to operate at a maximum pass rate of 100 kHz with a latency[1] of 2 μs. Because

[1]In general latency is the time delay between the moment something is initiated, and the

the latency is much longer than the event frequency, the information of all detector channels must be stored in "pipeline" memories before it is processed. For events accepted by the LVL1, the information of all sub-detector systems is pre-processed and stored in Read-Out Buffers (ROBs). This level of filter is implemented in hardware [51].

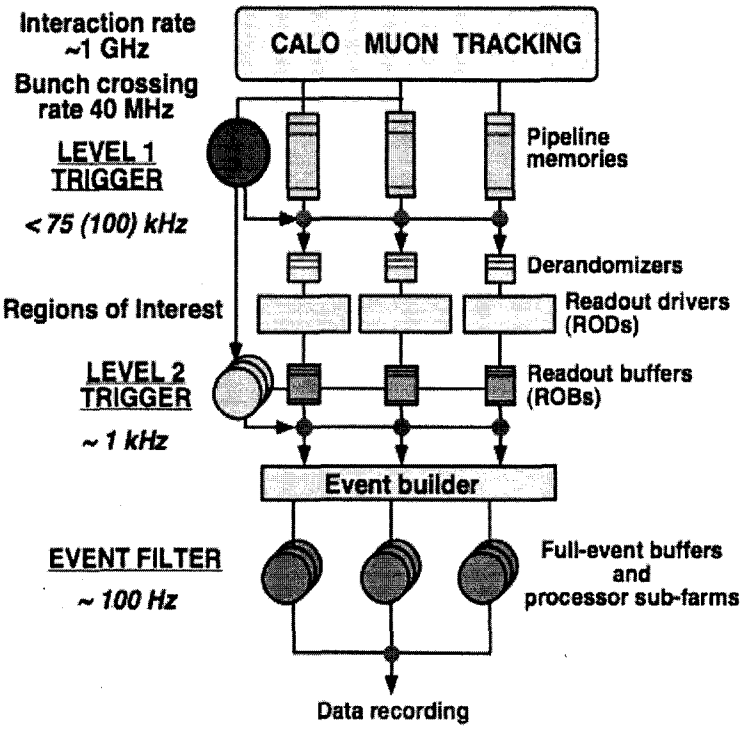

Figure 3.21: *The three levels of ATLAS trigger.*

The second level trigger (LVL2) utilizes both the LVL1 output and the data stored in the ROBs to further reduce the data rate to a maximum of $\sim$ 1 kHz. The LVL2 incorporates the precision MDT chamber information to improve the muon momentum estimate, it also has a chance to access the reconstructed track from the inner detector, and calorimeter clusters. The latency of LVL2 is event dependent, a simple event takes only 1 ms while a complicated event might take up to 10 ms. All the accepted events and their the data fragments stored in the ROBs, are collected by the Event Builder and written into the Full Event Buffers (FEB). This level of trigger uses computer farms to perform the selection.

moment one of its effects begins or becomes detectable.

An important piece of the strategy of the ATLAS trigger relies on the Region-of-Interest (RoI) mechanism for which the LVL2 trigger makes use of information provided by the LVL1 trigger in localized region of the calorimeter and muon sub-detectors. The information contained in the RoI typically include the position (η and ϕ) and the p_T of the candidate objects as well as energy sums. Candidate objects selected by the LVL1 can be high-p_T muons, electrons or photons, hadrons or taus, and jets. The energy sums include the missing-E_T vector and the scalar E_T value. For all selected LVL1 events, the RoI information is sent to the LVL2 using a dedicated data path. Making use of the RoI information, the LVL2 algorithms only transfer data from the necessary ROBs in order to arrive quickly at a LVL2 decision.

The third level trigger is called the Event Filter (EF). From the event information stored in the Full Event Buffers, the EF utilizes farms of PCs to reconstruct the event and to compute quantities like track trajectories, cluster energies, jets, missing transverse energy, secondary decay vertexes, etc. The final dataset is written to storage at around 100 MB per second after the third level trigger.

3.3 Detectors in the Forward Region of ATLAS

In addition to the main ATLAS detector, three smaller systems are being built to provide coverage in the very forward region. These are closely connected to the luminosity determination in ATLAS, but are also foreseen to study forward physics. If ordered according to their distance from the ATLAS interaction point (see Fig. 3.22), the first system is a Cerenkov detector called LUCID that is the subject of this thesis. LUCID is the main luminosity monitor in ATLAS and is located at a distance of 17 m from the interaction point. The second system is a zero degree calorimeter (ZDC), which is located at a distance of 140 m from the interaction point. This corresponds to the location where the LHC beam pipe is divided in two and the ZDC is located between the beam pipes just after the split inside an absorber. The most remote detector is the ALFA system which consists of scintillating-fibre trackers located inside Roman Pots

at a distance of 240 m from the ATLAS interaction point.

The FP420 Research and Development (R&D) project is proposing to place detectors near to the beam about 420 m from the interaction point. This effort and our contribution to it are described later in chapters 8 through 10.

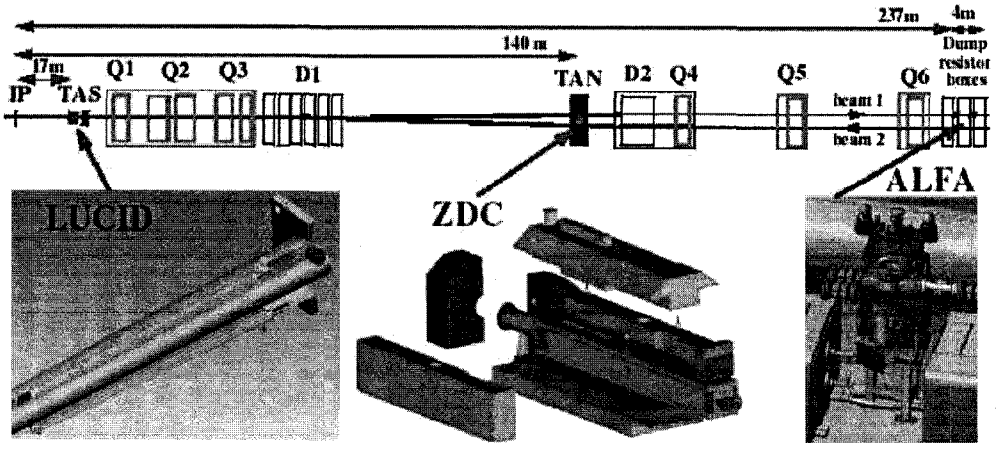

Figure 3.22: *Placement of the forward detectors along the beam line around the ATLAS interaction point (IP).*

Chapter 4

Luminosity Measurement at ATLAS

4.1 Introduction to Luminosity

In particle physics, an accurate luminosity measurement is key to an optimal measurement of cross-section. As shown in Fig. 4.1, in the detection of the Higgs boson in ATLAS, for example, of $m_H = 140$ GeV, the error on measuring $\sigma \times Br$ (where Br is the branching ratio) is of the order of 10% with a luminosity accuracy of 5% [1].

Luminosity connects the number of signal events with the production cross-section. Considering the situation at a collider detector, the number of observed events passing the final analysis cuts is related to the cross-section by the following:

$$N_{observed} = \varepsilon \cdot \mathcal{L} \cdot \sigma,\ N_{true} = \mathcal{L} \cdot \sigma, \tag{4.1}$$

where N is the number of signal events after background subtraction, ε is a general efficiency term combining the detector and trigger efficiency, and acceptance [52], $\mathcal{L}$ is the integrated luminosity.

Thus over a period of running Eq. 4.1 can be written as an integral over time:

$$\int n(t)dt = \sigma \cdot \int \mathcal{L}(t)\varepsilon(t)dt\,, \tag{4.2}$$

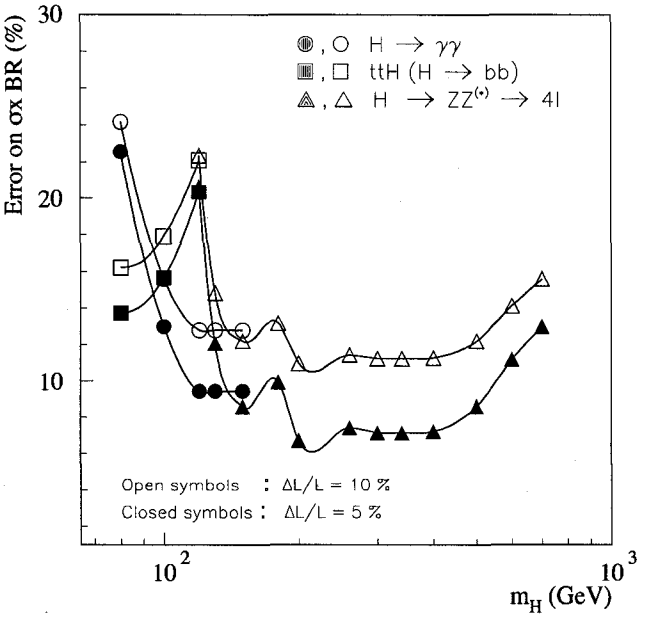

Figure 4.1: *Relative precision on the measurement of the Higgs-boson rate ($\sigma \times Br$ for various channels, as a function of m_H, assuming an integrated luminosity of 300 fb^{-1}. The luminosity is assumed to be known to 10% (open symbols) or to 5% (closed symbols).*

where $\int n(t)dt = N$. Thus the cross-section is

$$\sigma = \frac{\int n(t)dt}{\int \mathcal{L}(t)\varepsilon(t)dt} = \frac{N}{\int \mathcal{L}(t)\varepsilon(t)dt}, \tag{4.3}$$

where $\mathcal{L}(t)$ is the luminosity at time t (instantaneous luminosity).

4.1.1 Luminosity Blocks

In practice, we can assume that the time dependence of the luminosity is slow enough that we can approximate it as constant over a short time period (in the order of minutes). The data acquired in this time is called a Luminosity Block (LB). The size of the LB is set by experience, it should be small enough to avoid a large luminosity change and big enough to be practical for data analysis. In ATLAS the instantaneous luminosity of the machine is expected to decreases exponentially with a time constant of 6 to 7 hours, with a nominal time constant of 14 hours. So under nominal conditions, the luminosity drops by 1% after 10 minutes. The size of the LB in ATLAS is of the order of

minutes.

Considering the concept of LB, Eq. 4.3 can be written as:

$$\sigma = \frac{\sum_i N_i}{\sum_i \mathcal{L}_i \varepsilon_i} = \frac{N}{\sum_i \mathcal{L}_i \varepsilon_i}. \tag{4.4}$$

The LHC has 3564 different slots for particle bunches, and therefore 3564 bunch crossings (BCs) occur per LHC turn. The instantaneous luminosity of the i^th bunch, Bunch Crossing ID (BCID)=i, is denoted $L_B^{(i)}$. Of all the 3564 BCs per turn, initially only 2808 of them will be filled with particles. The empty BCs have luminosity $L_B^{(i)} = 0$. Thus the delivered luminosity for a LB, which spans n_{turns} number of LHC turns is given as

$$\mathcal{L}^{delivered} = 25\text{ns} \cdot \sum_{k=1}^{n_{turns}} \sum_{i=0}^{3563} L_B^{(i)}. \tag{4.5}$$

Detailed calculation of luminosity determination considering the detector and trigger effects is discussed in Ref. [52].

4.2 Methods for Luminosity Determination in ATLAS

The absolute luminosity is used to calculate cross-sections. Relative luminosity measuring devices need to be calibrated to provide an absolute luminosity determination. For ATLAS, there are three methods to determine the absolute or relative luminosity, which are summarized below:

4.2.1 LHC Machine Parameters (Absolute/Relative)

The LHC beam parameters can be used to estimate the instantaneous luminosity at ATLAS [52]. These parameters include the number of protons per bunch, the transverse beam dimensions (β functions and beam emittance), and the transverse displacement of the two beams. Since these parameters will be available as soon as the beam is turned on, this method is likely to be the first method to give a reasonable luminosity estimate. The error of this

method is dominated by the uncertainty of the emittance of the beam, and is estimated to be on the order of 10%.

4.2.2 W/Z Counting (Absolute/Relative)

The absolute luminosity can be calculated from the measured W/Z event rate through leptonic decays [53]. The uncertainty of this method is determined by the understanding of parton distribution functions (PDF) and the theory of the physics process. With PDF uncertainties, tracking detector effects and the theoretical error in the W/Z production cross-section taken into account, the absolute luminosity can be determined to about 10%. Better precision can be achieved after better understanding of the PDF's and W/Z cross-section is available from the LHC. In this case precision as good as ~7% could be achieved.

The rate of W/Z production in LHC (at $10^{34}\,\mathrm{cm}^{-2}\mathrm{s}^{-1}$, the $W \to \nu e$ rate is of the order of 100's per second and $Z \to ee$ rate is of the order of 10's per second). Thus W/Z counting can be used for online relative luminosity monitoring with high statistical precision. With standard W/Z cuts, at $10^{34}\,\mathrm{cm}^{-2}\mathrm{s}^{-1}$ a statistical precision of 5% (1%) is expected after 10 s (3 min). This method is useful for luminosities higher than $10^{32}\,\mathrm{cm}^{-2}\mathrm{s}^{-1}$.

4.2.3 $pp \to p\gamma\gamma p \to p\mu^+\mu^- p$ (Absolute)

The possibility of using QED mediated exclusive muon pair production to measure the absolute luminosity is studied in [54]. Special kinematic requirements and selections are used in this method where no forward tagging of the scattered proton is needed. This method could potentially be used in all modes of LHC operation, including some luminosity pileup, instead of only during special beam conditions or very low luminosity runs. The cross-section for this process is small, given the requirement that the triggering muon must have a minimum p_T of 6 GeV to do online luminosity monitoring. A muon trigger, utilizing the Tile Calorimeter, with a 3 GeV muon energy threshold is envisaged, but not yet implemented. Therefore this method can only be used to measure absolute luminosity. The rate of muon pair production in the LHC (at $10^{34}\,\mathrm{cm}^{-2}\mathrm{s}^{-1}$) is of the order of 10's/minute with muon p_T cut 3 GeV and

<10/minute with muon p_T cut 6 GeV. The estimated experimental accuracy for the absolute luminosity measurement is between 3 - 5 %, assuming that sufficient statistics can be collected during the measurement period where the luminosity conditions are stable.

4.2.4 Roman Pots (ALFA)

By measuring the scattered proton under high β^*[1] condition, the absolute luminosity can be determined. During this run the LUCID luminosity monitor will be calibrated. The expected error on the absolute luminosity is $\Delta\mathcal{L}/\mathcal{L} = 2 - 3\%$.

This measurement will only be made at high β^* runs, at low luminosity ($10^{27}\,\mathrm{cm}^{-2}\mathrm{s}^{-1}$), to reach the theoretically well-calculable Coulomb scattering regime with the appropriate optics [55, 56, 43]. The scattered proton will be measured with a scintillating fiber tracking detector (ALFA) deployed in Roman Pots[2] [39] mounted at ±240 m from the ATLAS IP. A schematic of the Roman Pot assembly is shown in Fig. 4.2.

The detector used to determine the position of the proton track is a scintillating fibre tracker, as shown in Fig. 4.3, each detector contains one x and one y plane, accompanied by a scintillator plate for triggering. A plane is made of staggered fibers and the size of each plane is 3×3 cm^2. The fibers are connected to multi-anode photo-multiplier tubes (PMT) for light readout. The square fibers have a size of 0.5 mm, by placing 10 layers of these fibers together along the beam direction, an overall spatial resolution of 30 μm for each track can be achieved.

4.2.5 LUCID (Relative)

LUCID is a gas Cerenkov detector which measures the relative luminosity by counting tracks from minimum bias events[3]. It is designed to work over all

[1] β^* is a parameter of the proton beam optics. With higher β^*, the size of the cross section of the beam is larger, while the divergence of the beam is smaller.

[2] A Roman Pot is a device that allows the detector assembly to be placed around the beam axis. It can move the detector to as close as possible to the circulating beam during the data taking without breaking the beam pipe vacuum.

[3] Minimum-bias events are normally elastic or inelastic diffractive pp interaction with low transverse energy.

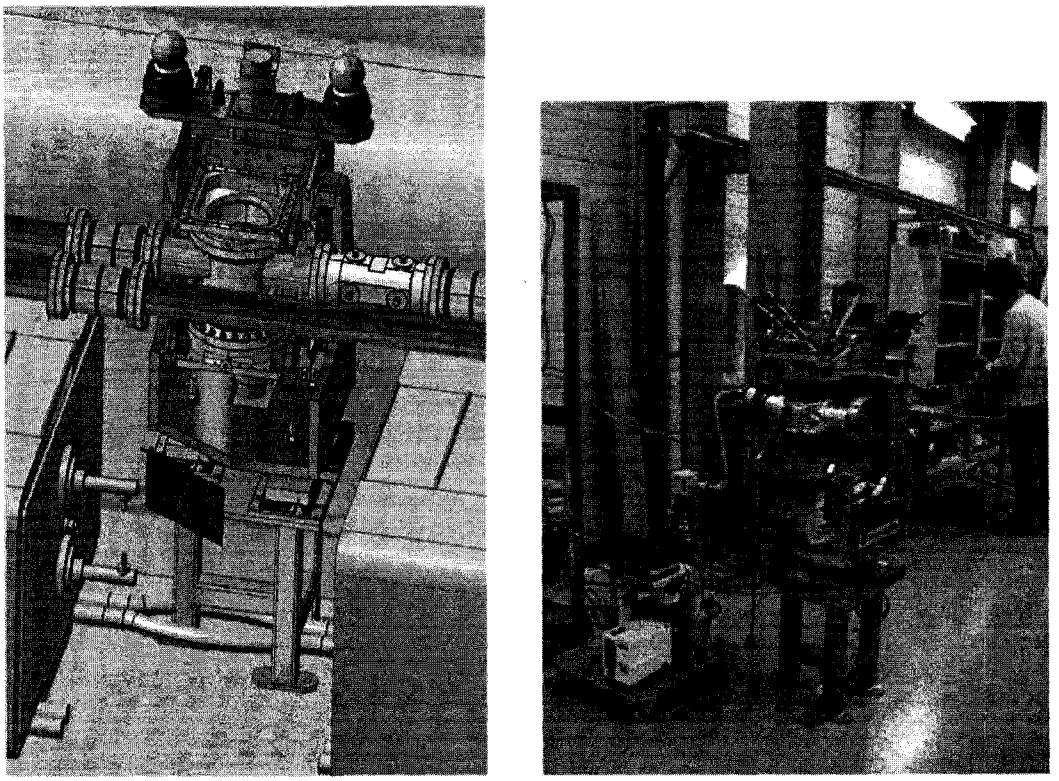

Figure 4.2: *Schematic view of the support mechanics (Roman Pot) for one of the ALFA detectors and of its location at a distance of 240 m from the ATLAS interaction point (left). Also shown (right) is one of the as-built structures, which will house the scintillating fibre trackers.*

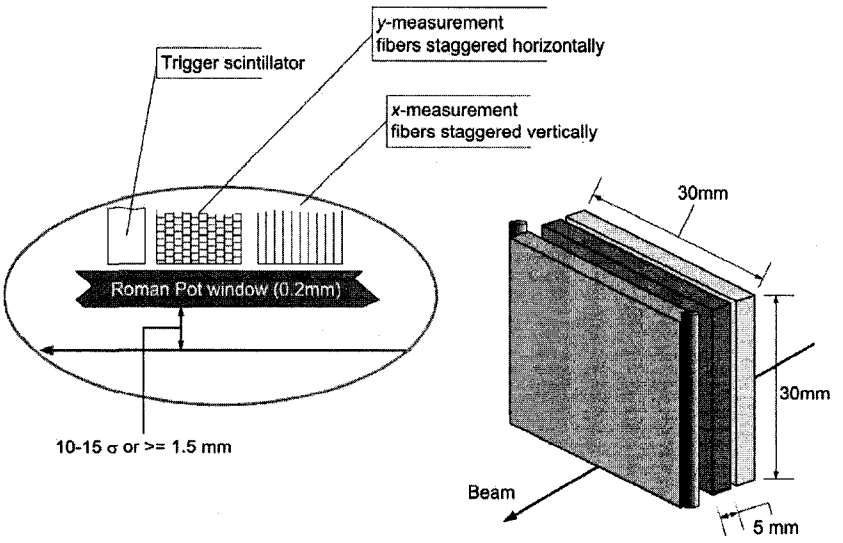

Figure 4.3: *Schematic representation of the fibre tracker, housed inside a Roman Pot. The tracker comprises two planes with fibers staggered horizontally (y plane) and vertically (x plane). A large scintillator plate is added in front for the trigger.*

luminosity range. LUCID can be calibrated using the machine luminoisty determination, or physics processes as described above. The luminosity measurement resolution is estimated to be as good eventually as ~3% after calibration with the measurement of elastic scattering in the Coulomb region performed utilizing the ALFA detectors. Details of the LUCID detector are covered in Chapters 5 and 7.

4.2.6 Beam Condition Monitor (Relative)

The Beam Condition Monitor (BCM) is designed to provide monitoring information about the beam conditions. However, its potential of providing luminosity information is also under study [57]. The BCM consists of four 1×1 cm^2, 500 μm thick diamond sensors which are mounted in modules at a distance of 1.8 m on each side of the IP and at 5 cm radius from the beam axis. The luminosity monitoring of BCM is based on inelastic events, where the BCM covers $3.9 < |\eta| < 4.1$ and the system can in principle cover the whole luminosity range at the LHC.

4.3 Luminosity Monitoring with LUCID

In the case of the LUCID luminosity monitor, the luminosity, $\mathcal{L}_B^{(i)}$, can be determined from inelastic collisions mainly using two methods [52]: the Collision (Zero) Counting Method and the Particle Counting Method.

4.3.1 Collision (Zero) Counting Method

The collision counting method relates the luminosity to the total collision rate of the bunch crossings. For each of the 3564 bunches in the LHC, the collision rate is monitored separately by the luminosity monitors, i.e., for a specific $BCID = i$, the luminosity for this BC $\mathcal{L}_B^{(i)}$ during a defined time interval can be determined from [52]

$$\frac{n_{pp}^i}{n_{BC}^i} = 1 - e^{-A \cdot \mathcal{L}_B^{(i)}}, \tag{4.6}$$

where n_{pp}^i is the number of times one or more interactions have been detected for $BCID = i$ by the luminosity monitor, n_{BC}^i is the total number of crossings of $BCID = i$, A is a calibration constant and $\mathcal{L}_B^{(i)}$ is the bunch luminosity for $BCID = i$.

The integrated luminosity for a specific luminosity block can then be written as:

$$\mathcal{L} = n_{turn} \sum_i^{3564} \mathcal{L}_B^{(i)} = -\frac{n_{turn}}{A} \sum_i^{3564} ln\left(1 - \frac{n_{pp}^i}{n_{BC}^i}\right). \tag{4.7}$$

This method counts how many zeros (where there is no interaction detected in the luminosity monitor) for each BCID. The advantage of this method is the fact that it does not require a particle counting capability from the luminosity monitor. So it is possible to use this method with the LUCID and BCM systems.

The relation between the luminosity and the measured fraction of the colliding BCs n_{pp}^i/n_{BC}^i is not a linear relation across the luminosity range of ATLAS. At very low luminosity where the number of pile-up events per BC is much smaller than 1 ($\mu << 1$), this relation become linear $n_{pp}^i/n_{BC}^i \sim A \cdot \mathcal{L}_B^{(i)}$.

Another problem with the use of the zero counting luminosity determination at the LHC is the fact that at the design luminosity there will rarely be a crossing with zero hits.

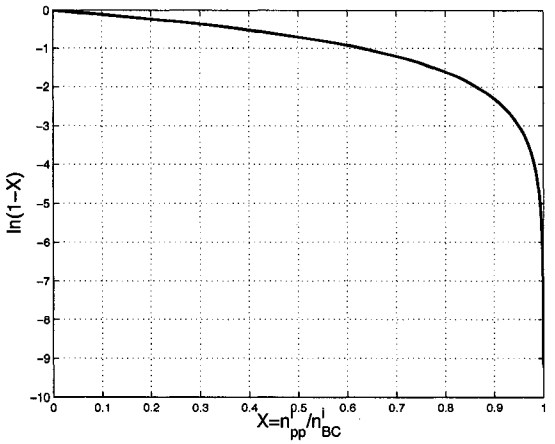

Figure 4.4: *Non-linear relation of Eq. 4.7.*

For a higher luminosity, Eq. 4.7 becomes highly non-linear since the integrated luminosity, expressed as the sum of the contributions from each BC, does not correspond to the mean number of collisions obtained from all the BCs:

$$-\frac{n_{turn}}{A}\sum_{i}^{3564} ln\left(1-\frac{n^i_{pp}}{n^i_{BC}}\right) \neq -\frac{n_{turn}\cdot 3564}{A} ln\left(1-\frac{\sum_i n^i_{pp}}{\sum_i n^i_{BC}}\right). \tag{4.8}$$

For this reason, the luminosity monitor system that determines luminosity from this method should be capable of determining n_{pp}/n_{BC} separately for each BCID.

4.3.2 Particle Counting Method

The particle counting method relates the luminosity to the mean number of particles per BC:

$$<M> = \sum_{i,j}^{3564,n_{turn}} \frac{n^{ij}_{part}}{3564\cdot n_{turn}} = <C>\cdot A\cdot <\mathcal{L}_B>, \tag{4.9}$$

where $<M>$ is the measured average number of particles per BC, n^{ij}_{part} is the number of particles obtained from $BCID = i$ at turn j, n_{turn} is the number of turns in a LB, A is a calibration constant, and $<C>$ is the average number of

particles per detected interaction. $<C>$ has to be detected at low luminosity where at most one interaction per BC is by far the most probable event.

Unlike the Zero Counting Method, the linear relationship between $<M>$ and $<\mathcal{L}_B>$ is maintained over the full luminosity range. Also, the relation is $BCID$ independent so that the luminosity for a specific luminosity block can be written as

$$\mathcal{L} = n_{turn} \cdot 3564 \cdot \frac{<M>}{<C> \cdot A}. \tag{4.10}$$

This method has the advantage of a linear relation at higher luminosity, however it does require particle counting capability. The Particle Counting Method will be used as the baseline method in the LUCID detector.

Chapter 5

A Luminosity Monitor for ATLAS - LUCID

5.1 Introduction

The received luminosity of hadron collider experiments is traditionally monitored using dedicated scintillation counters which measure the fraction of bunch crossings with no interactions. Such detectors are usually put at relatively high rapidity so that they have a larger acceptance for inelastic $pp(\bar{p})$ interactions. In LHC and ATLAS, however, the designed luminosity is so high that the fraction of crossings with no interaction will be small. Also, the radiation levels are high enough to render scintillation counters unusable.

LUCID (short for LUminosity measurement using a Cerenkov Integrating Detector) is a robust, fast, dedicated detector to monitor with precision the average number of pp interactions. It is a detector based on Cerenkov technology, which is used by CLC (Cerenkov Luminosity Counter) at CDF [58, 59]. LUCID measures the number of hits per beam crossing directly. Also the radiation hard construction of LUCID renders it useable at the highest projected luminosity.

5.2 Design of LUCID

The LUCID detector will be installed in two phases. In the first phase, within the first three years of ATLAS running from the spring of 2008, ATLAS will be running at a relatively low luminosity ($10^{33}\,\mathrm{cm}^{-2}\mathrm{s}^{-1}$). The Phase I LUCID detector will be installed to cover this period. When ATLAS starts full luminosity ($10^{34}\,\mathrm{cm}^{-2}\mathrm{s}^{-1}$) running, the Phase II LUCID detectors will be installed to allow precise luminosity monitoring at high radiation loads.

5.2.1 Phase I LUCID Detector

Overview

The Phase I LUCID detector consists of two modules that are located in the available space between the beam pipe and the conical beam-pipe support structure, in the forward shielding, after the ATLAS End-Cap Muon System Toroids, as shown in Fig. 5.1. The beam pipe inner diameter at the position

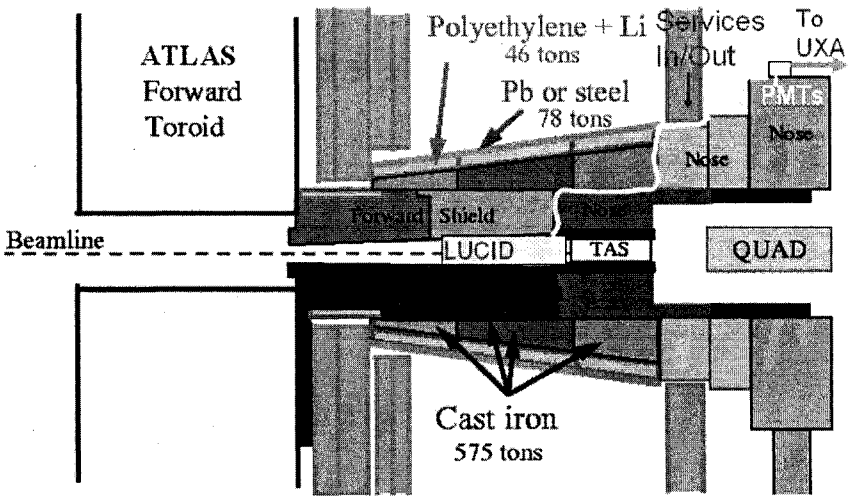

Figure 5.1: *A sketch of the proposed positioning of one of the two LUCID detector. The other detector would be placed in the symmetrically opposite position.*

of LUCID is 123 mm with thickness 1.5 mm. The range of pseudorapidity covered by LUCID is $5.6 < |\eta| < 5.9$ when the front of the detector is placed at $z = 16.7$ m from the IP. A side view of the LUCID detector and the VJ

cone that supports LUCID is shown in Fig. 5.2, and a perspective view in Fig. 5.3.

Each LUCID detector module consists of twenty 15 mm inner diameter, 1.5 m long, cylindrical, gas filled Cerenkov tubes. Sixteen of the tubes are directly mounted onto a (PMT) photo-multiplier tube. The other four tubes are connected to a fused-silica fibre bundle through a concentrator. The fibre bundle is in turn connected to a Multi-anode PMT (MAPMT) located on top of the shielding, in a low radiation zone (5 Gy/yr). The twenty tubes are arranged around the beam pipe in two layers. A cross-section through LUCID is depicted in Fig. 5.4.

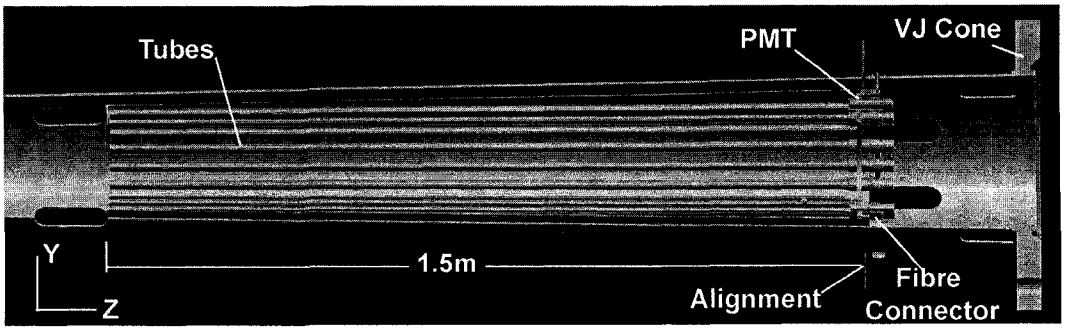

Figure 5.2: *Side view of the LUCID detector.*

The LUCID mechanics system includes PMT readout Cerenkov tube detectors, fibre/MAPMT readout Cerenkov tube detectors, Gas System, Alignment System and Calibration System. A summary of major design parameters is given in Table.5.1.

Because the tubes are pointing to the IP, prompt particles coming from the IP (primaries), and some of their direct secondaries (from interactions in the beam pipe), will travel the full length of the Cerenkov counter tube and generate a large amplitude signal in the photo-detector. Particles originating from soft secondary interactions and coming from other directions will in general traverse the counters at larger angles, with shorter path length, thus giving less light. In addition, the light from these particles will also suffer a larger number of reflections in the aluminum tubes. The signals from these "soft" particles are therefore usually significantly smaller than those from the primaries and hard secondaries and can be discriminated using suitable amplitude thresholds in the electronics and in the offline data analysis. This is

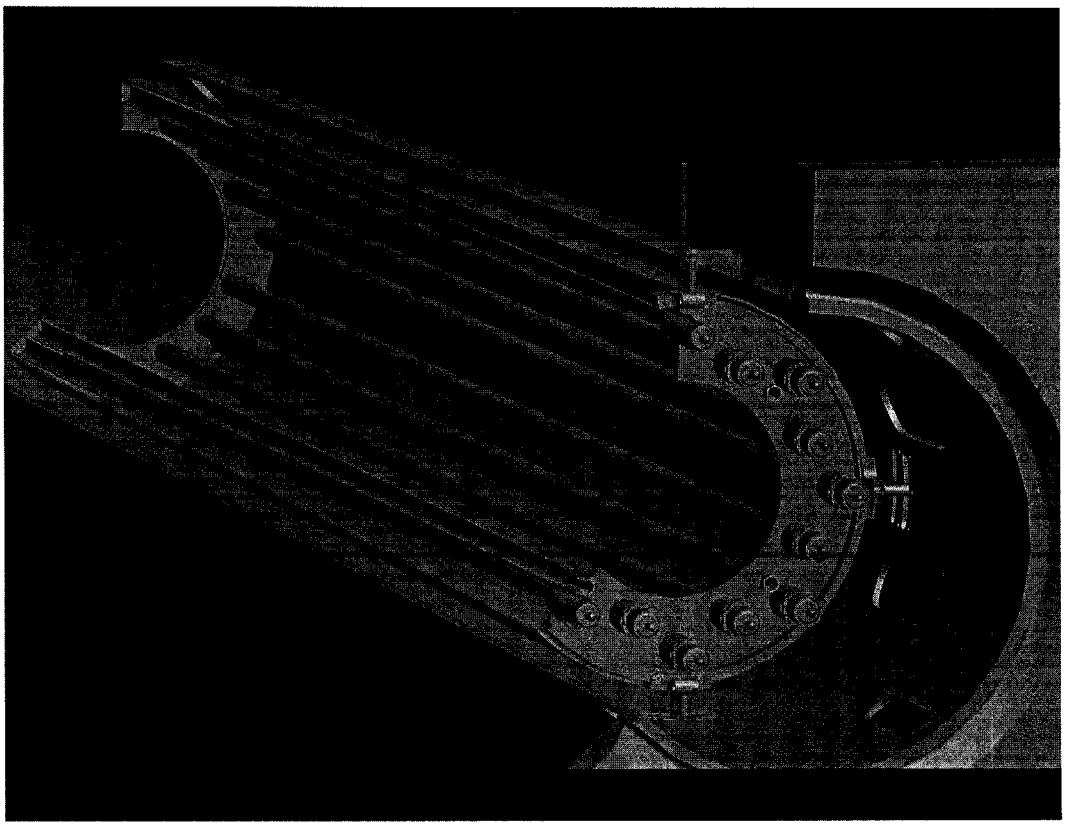

Figure 5.3: *Cut-away view of LUCID, viewed from the downstream end (Looking at the direction of IP).*

General		
	Al Tube Inner Diameter	15 mm
	Al Tube Outer Diameter	16.5 mm
	Radiator Gas	C_4F_{10}
	Working Pressure	1.3 bar
PMT Detector		
	Tube Length	1494.5 mm
	PMT Model	Hamamatsu R1166
	PMT Sensitive Diameter	15 mm
	PMT Window Thickness	1 mm Quartz
Fibre Detector		
	Tube Length	1391.5 mm
	Cone Length	100 mm
	Cone Input Diameter	15 mm
	Cone Output Diameter	6 mm
	Fibre Model	PUV-900
	Fibre Bundle Diameter	6mm
	Number of fibres in Bundle	37
	Fibre Bundle Length	$\sim$ 5 m
	MAPMT Model:	Hamamatsu R7600
Cooling System		
	Heat Power Source	$\sim$ 250 W/m Alone Beam Pipe (Heat Flux 634 W/m^2)
	Baking Temperature	250°C
	Cooling Pipe Diameter	4 mm
	Water Flow	20 liter/hours

Table 5.1: *Major Design Parameters of LUCID.*

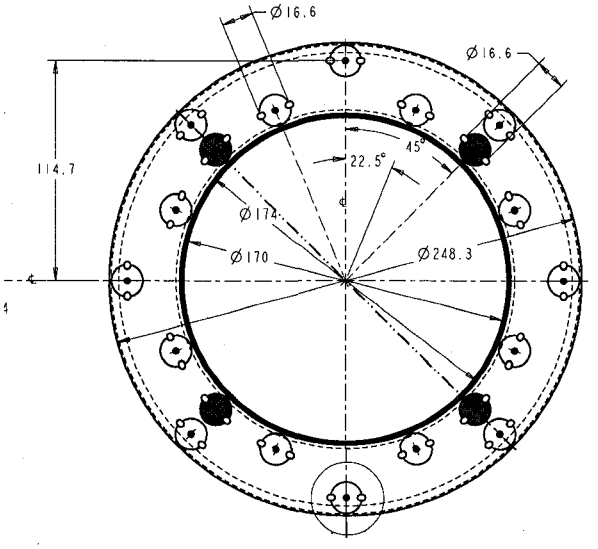

Figure 5.4: *Engineering Drawing of the LUCID Front Bulkhead. The blue (shaded) tubes are connected to fibre bundles, the other tubes are connected to PMTs directly.*

also an advantage of LUCID over normal scintillation counters.

At higher occupancies, when two primary particles traverse a single tube the resulting signal is twice that of a single particle. Given that there are no Landau fluctuations (as in scintillators) the counter's amplitude distribution should show distinct peaks for the different particle multiplicities hitting the counters. These distributions enable us to count the actual number of primary particles hitting LUCID and not the number of "hits", particularly at high luminosity.

The LUCID detector counts tracks from minimum bias events that consist of elastic scattering events, diffractive events, double diffractive events, low-p_T scatters and semi-hard QCD ($2 \rightarrow 2$) processes. The total cross-section for these processes is estimated to be ~ 100 mb[1].

The Phase I LUCID is now being fabricated and will be installed in ATLAS in February 2008 before the first beam in the LHC.

[1]The estimation is done with PYTHIA.

Type of Detectors

Two different readout schemes are incorporated in LUCID. The first, where the Cerenkov tube directly couples to a PMT, and the second, where the light is collected from the Cerenkov tube by optical fibre and read out by MAPMT.

Fig. 5.5 (top) shows the setup of a Cerenkov tube with a PMT mounted on it. The Cerenkov tube is made of aluminum with thickness 0.5 mm, inner diameter 15 mm and length 1494.5 mm. At the far end of the Cerenkov tube, a PMT with 15 mm diameter sensitive area is installed to collect the Cerenkov light produced in the tube. To minimize the background produced in the PMT window, the PMTs have specially made quartz flat front window of 1 mm thick.

PMTs were used to read out the Cerenkov tubes in the CLC detector at CDF. The advantages of this type of detector are: the simple optics, and the large number of photo electrons (over 50) produced for each primary charged track. A disadvantage is that secondary non-pointing charged particles also produce large amount of photons in the PMT window. Thus at higher luminosity the background is considerable larger (See Chapter 7).

Fig. 5.5 (bottom) shows the setup of a Cerenkov tube connected to a MAPMT through a light collector cone and an optical fibre bundle. This light collector is a 10 cm straight cone and it reduces the diameter from 15 mm to 6 mm. A Winston Cone [60] was also considered, with the same length, input and output aperture. In this configuration the Winston Cone is only 15% more efficient than a straight cone. A straight cone was used for ease of manufacture.

The fibre chosen for the setup is PUV900 from Ceramoptec. 37 fibres are bundled together through optimal packing (Fig. 5.6) to form a 6 mm diameter fibre bundle. The 37 fibres are divided into 10 groups; each group connects to a channel on the 64-channel MAPMT. The length of the fibre bundles are ~ 5 m. Parameters of the fibre bundle are listed in Table 5.1.

The connections between the PMT-tube and fibre-tube are shown in Fig. 5.7

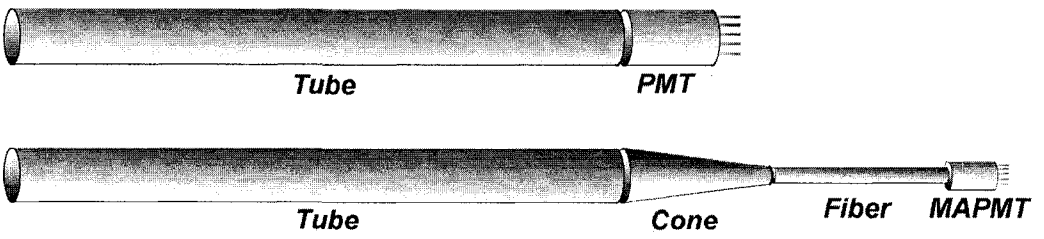

Figure 5.5: *A sketch of a Cerenkov tube with PMT (top) and a Cerenkov tube connected to a MAPMT through a light concentrator cone and optical fibre bundle (bottom).*

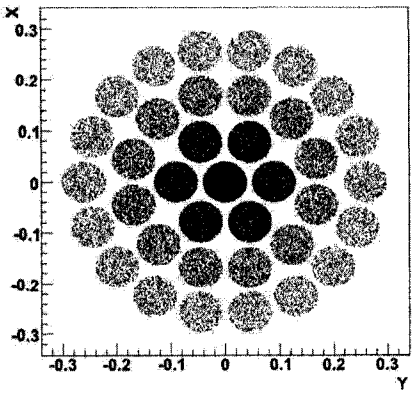

Figure 5.6: *Packing of 37 fibres to form a fibre bundle. Fibres represented in a darker color collect more light, when a charged particle traverse the tube along its axis. Both X and Y are in cm.*

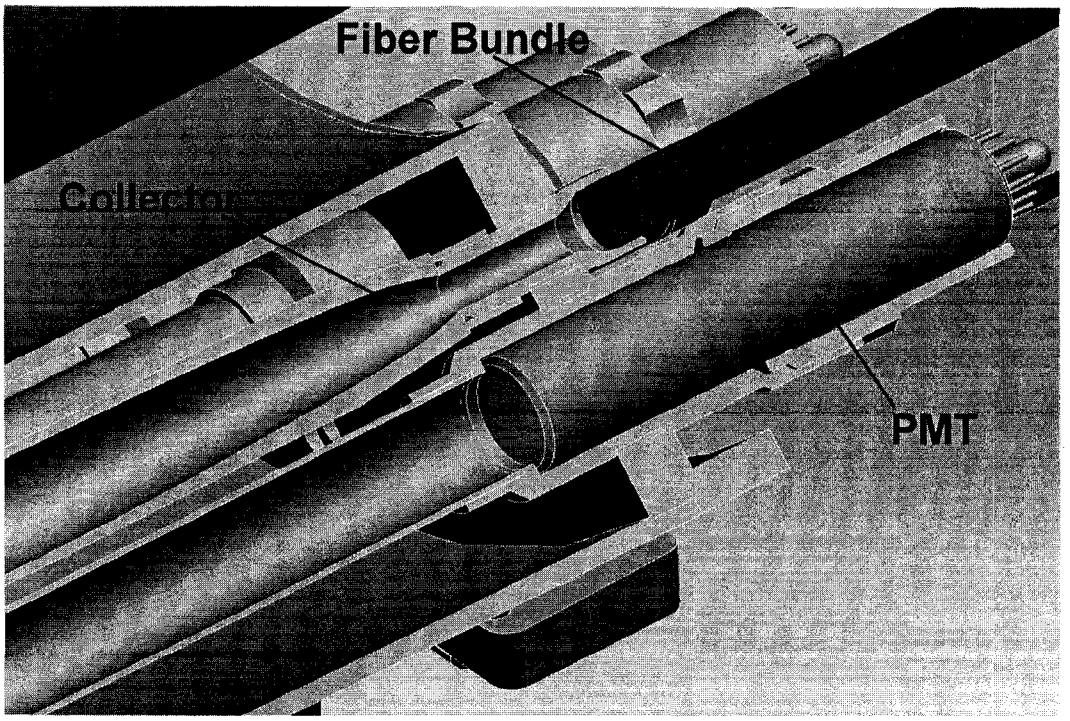

Figure 5.7: *Connection of Al tubes with PMTs and fibre Bundles.*

Gas System

The gas radiator used is C_4F_{10}, a safe gas with large index of refraction ($n = 1.00137$) at atmospheric pressure, which has good transparency for photons in the UV region, where most of the Cerenkov light is emitted. The detector is designed to run at 1.3 bar absolute.

The Cerenkov light cone half angle under this pressure is $\sim 3°$, and the momentum threshold for light emission is 9.3 MeV/c for electrons, 2.7 GeV/c for pions and ~18 GeV/c for protons. C_4F_{10} was chosen over the lower cost Isobutane (C_4H_{10}) alternative because it is non-flammable.

A diagram of the LUCID gas system is shown in Fig. 5.8. Two gas sources are used, one source provides the environmental friendly inert Argon used mainly for flushing the detector, the other source provides the working gas C_4F_{10}. An absolute pressure regulator is used to maintain the working pressure of 1.3 bar with an accuracy of ± 10 mbar. The gas system also contains a vacuum pump, to allow LUCID to be evacuated, prior to filling with C_4F_{10}.

The LUCID gas vessel is connect to the gas system through 8 mm copper

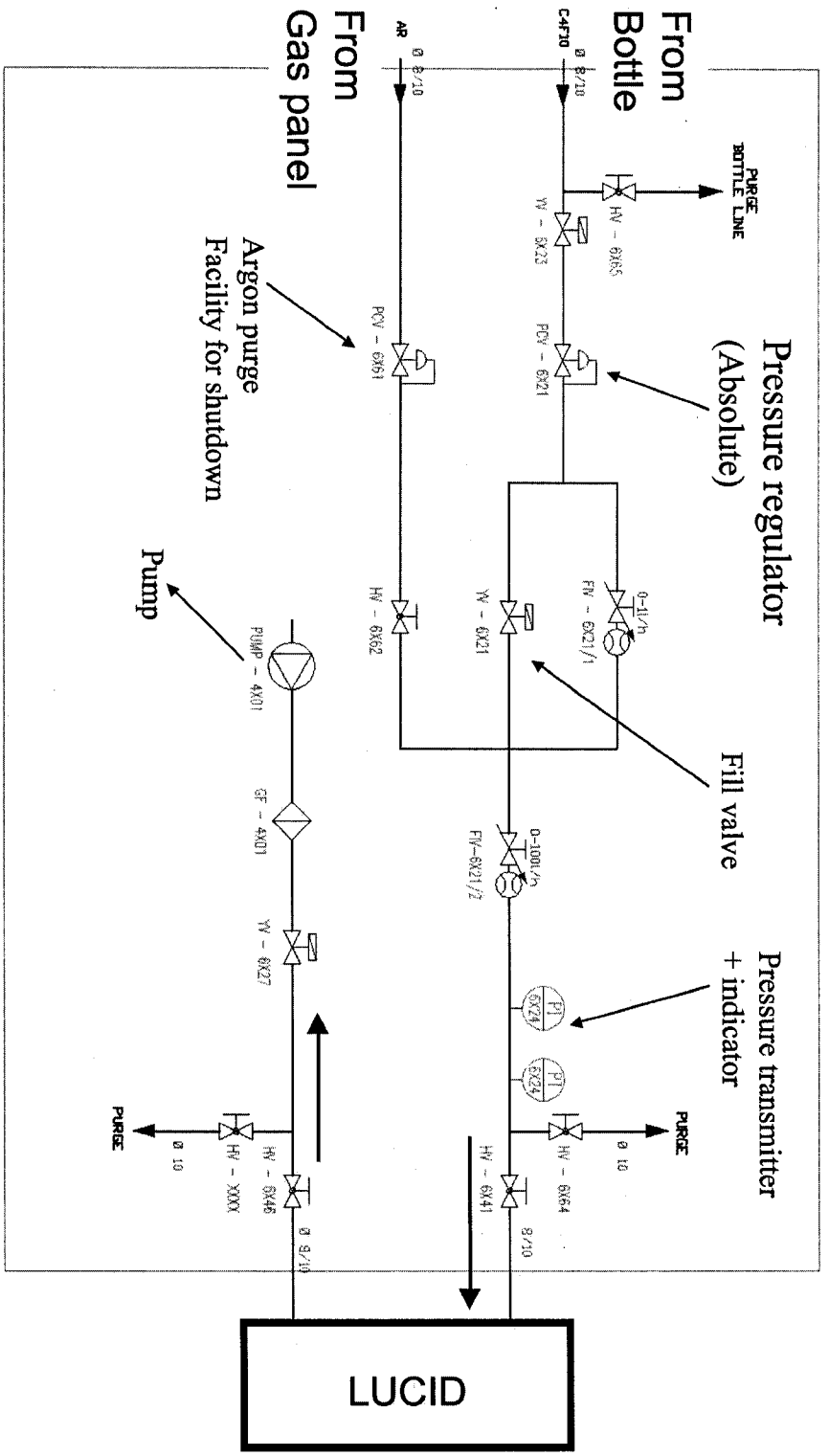

Figure 5.8: *The LUCID gas System.*

or stainless steel tubes. Fig. 5.9 shows the gas vessel and the front/back bulkheads.

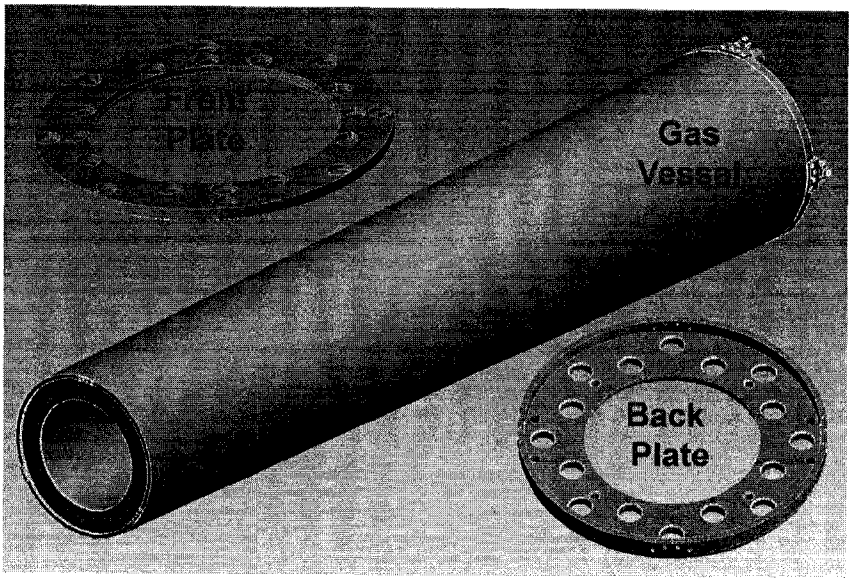

Figure 5.9: *The LUCID gas vessel and the front and back bulkheads (plates).*

Alignment System

The LUCID detector is mounted on the VJ support cone. Since the Cerenkov Detectors are required to point to the IP, with a pointing accuracy of the order of 0.1 degrees, the alignment of the system is very important. The LUCID Alignment System consists of 3 front alignment features and 4 back alignment features. In the front (closest to the IP) end, LUCID is suspended on 3 multi-thread steel cables, which are connected to a precision adjustment mechanism, as shown in Fig. 5.10. In the back end, LUCID is mounted to the VJ Cone by 4 sets of screw-nuts, as shown in Fig. 5.11, which provides movement in the transverse plane (X-Y). The pole sticking out of the VJ cone in Fig. 5.11 is used for the surveyors mark. So that the position of the LUCID can be located by the LHC coordinate system.

Calibration System

A LED calibration system is also included in LUCID. Several LEDs at different wavelength (from $\sim$ 200 nm to $\sim$ 600 nm), and driven by a pulsar system, are

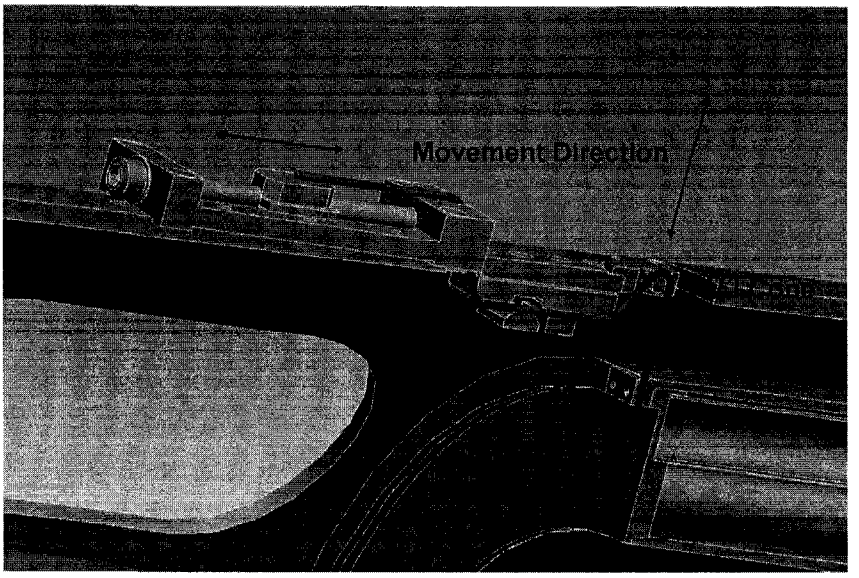

Figure 5.10: *LUCID front alignment features.*

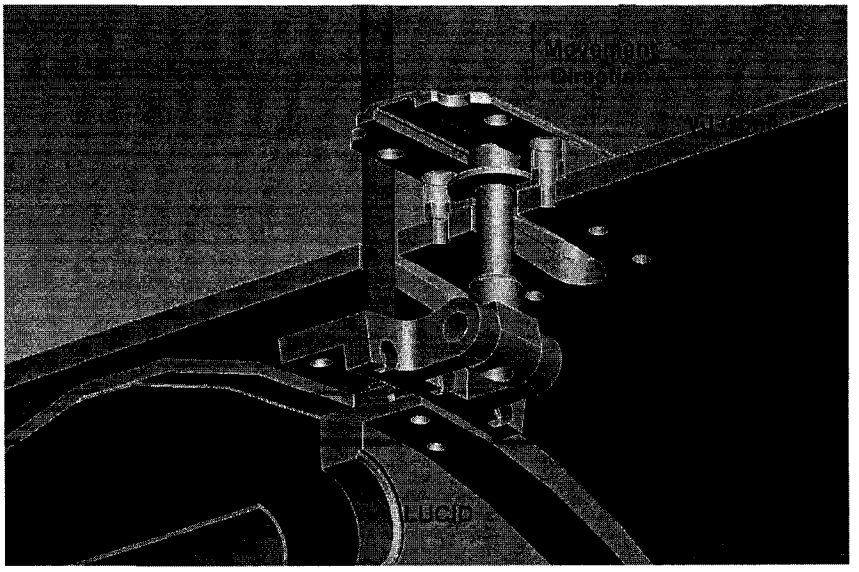

Figure 5.11: *LUCID Back Alignment Features.*

located on top of the shielding (where the MAPMTs are housed). The LEDs are coupled to optical fibres and the fibres in turn are placed in the front end of each of the Cerenkov tubes. The main purpose of the system is to monitor the gain of the PMT and MAPMTs, and to detect gas impurities by measuring UV light transmission.

Cooling System

During the start-up period of LHC, to achieve high vacuum, the beam pipe is baked at 250°C for 24 hours. As LUCID is adjacent to the beam pipe, to protect the PMTs, fibres and other mechanical parts from overheating, a cooling system is needed during bake-out.

The LUCID cooling system includes 4-6 loops of 4 mm copper tubes mounted on the outer shell of the beam pipe section near LUCID, as shown in Fig. 5.12. The cooling water provided by ATLAS services at 18°C is pumped into the tubes at 20 litres/hour. The temperature inside LUCID is maintained below 30-40°C, which satisfies the requirement that the PMTs not be heated over 50°C.

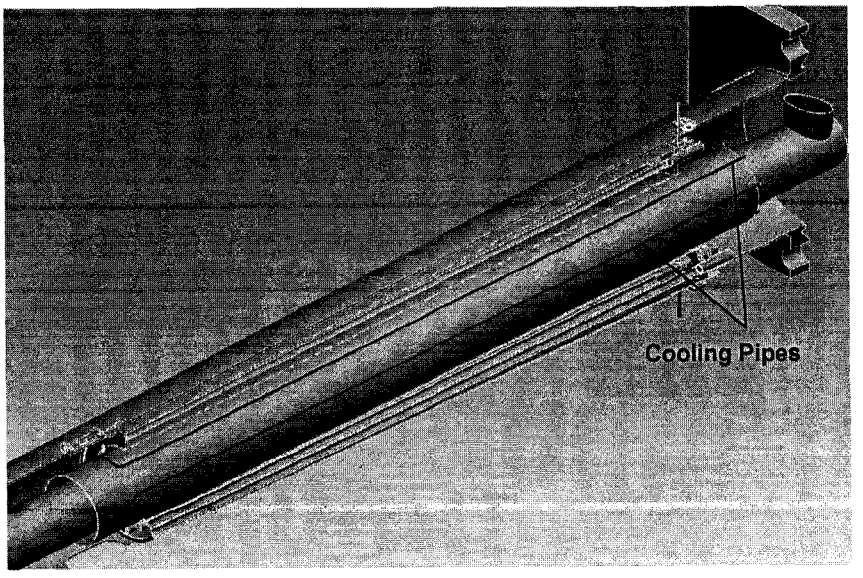

Figure 5.12: *LUCID Cooling Pipes.*

5.2.2 Phase II LUCID Detector

The Phase II LUCID detector is designed to run at higher luminosity (up to $10^{34}\,\mathrm{cm}^{-2}\mathrm{s}^{-1}$). It is based on the same principle as Phase I, but it is designed to operate at higher radiation levels. In addition, a large number of Cerenkov tubes are installed to provide full coverage over the pseudorapidity range of the LUCID detector. The purpose of this modification is to make LUCID a detector for forward physics at ATLAS.

The Cerenkov tubes are deployed in 4 layers each with 42 tubes. Each layer of tubes has different radius in order to maximize the area coverage. As in Phase I, all the tubes are pointing to IP. A perspective view is shown in Fig. 5.14.

The pseudorapidity coverage of Phase II LUCID is $5.5 < |\eta| < 6.1$; and the tubes cover $\sim 81\%$ of the area in this pseudorapidity region (Fig. 5.13).

To be able to endure the high radiation level in the LUCID region, all the tubes are connected to MAPMT's via Winston Cones connected to optical fibre bundles. The MAPMT's are located on top of the shielding which has a much lower radiation level (~ 5 Gy/yr). The final choice of MAPMT, cone shape and fibre bundles are still under study.

The Phase II LUCID design is likely to change as more experience is acquired with Phase I running. The detector is expected to be installed around 2010 prior to high luminosity running.

5.2.3 Optical Fibre

Several different types of optical fibres were tested in the test beam experiments. They are PUV fibres with 500 μm, 700 μm and 900 μm core diameter, and HUV fibre with 1000 μm core diameter. PUV and HUV are brand names of CeramOptics. Both PUV and HUV fibres have fused silica cores. PUV fibre has silicon cladding, while the HUV fibre has hard polymer cladding. The thickness of the cladding in PUV fibre is 50 μm. The thickness of the cladding in HUV fibre is ~ 18 μm. The PUV 900 fibre is chosen for the production of Phase I LUCID since it provide the right bundle size of 6 mm via optimally packing of 37 fibres.

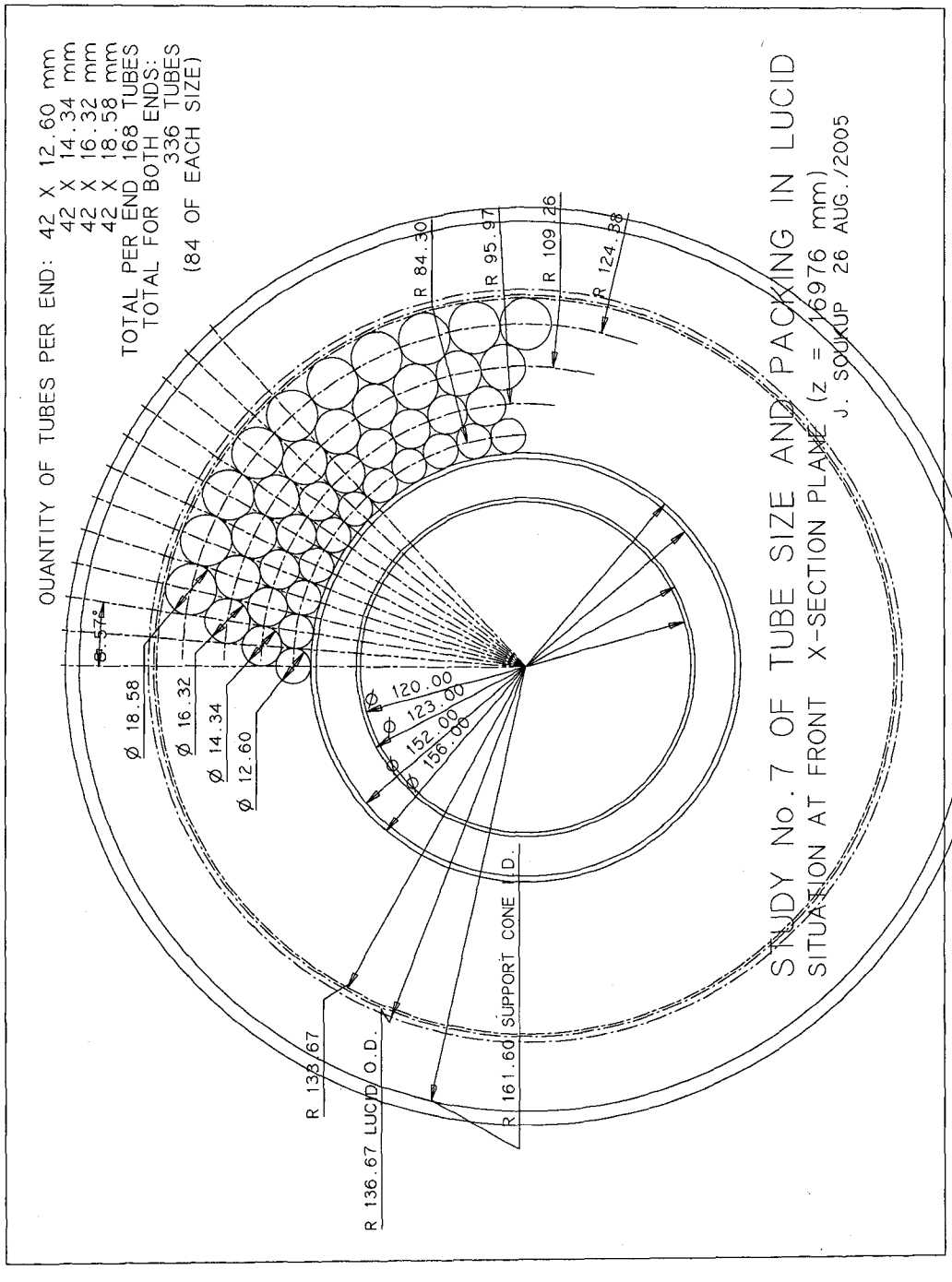

Figure 5.13: *A Cross-section view of Phase II LUCID at the mouth of a detector (Z = 16976 mm).*

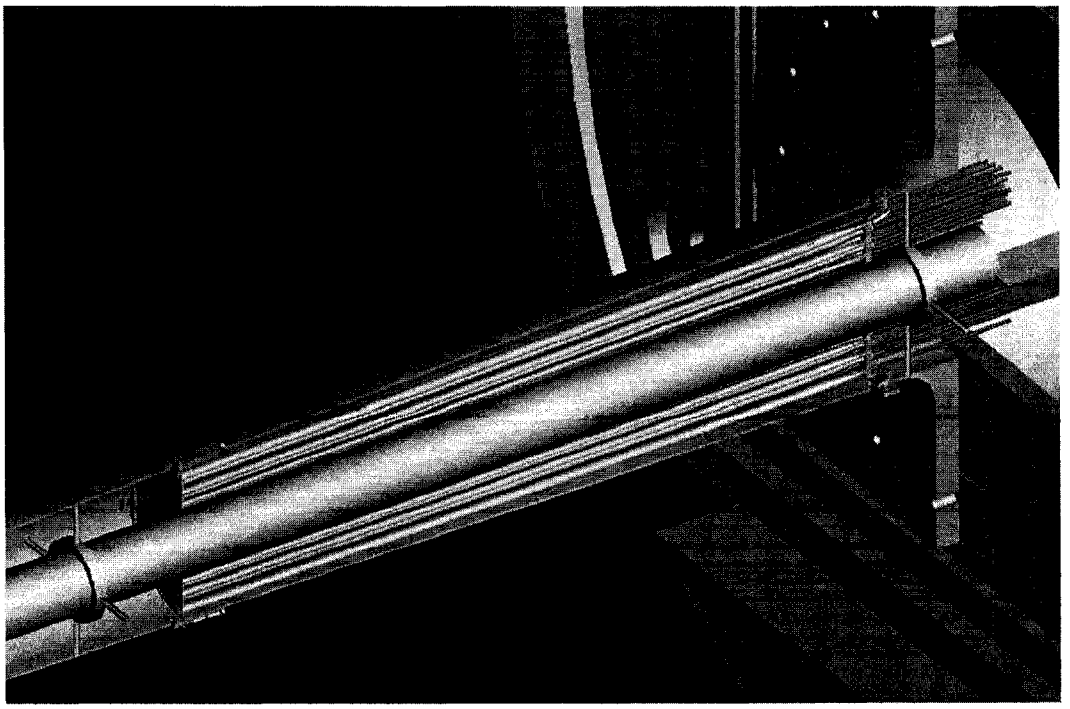

Figure 5.14: *A perspective view of LUCID Phase II Detector.*

The Numerical Aperture (NA) of an optical fibre is defined as:

$$NA = \sqrt{n_{core}^2 - n_{cladding}^2} \tag{5.1}$$

where n_{core} is the refractive index of the core and $n_{cladding}$ is the reflective index of the cladding. $NA \leq 0.37$ is used in the simulation. This number is obtained from the specifications provided by the fibre manufacturer.

The refractive index of fused-silica is used for the refractive index of the core as a function of wavelength. Assuming NA is the same over all wavelength regions, the refractive index of fibre cladding is obtained from Eq. 5.1.

5.3 Electronics and Readout

The basic requirement for the LUCID electronics is to count the track/hit multiplicity per bunch crossing in the detector. The track/hit multiplicity in a Cerenkov tube is proportional to the light signal collected by a photosensitive device (in our case PMT or MAPMT). The electronics also has to provide a

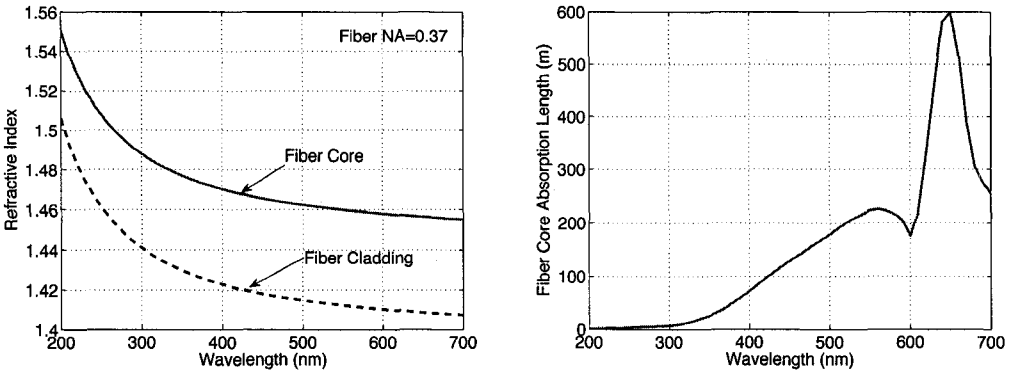

Figure 5.15: *Refractive index of fibre core and cladding (left) and the absorption length of fibre core. The absorption length is obtained from the company specifications.*

trigger and transfer the necessary information to the ATLAS DAQ.

For Phase I LUCID there are two methods by which Cerenkov tubes are read out. When the light produced in single Cerenkov tubes is read out directly by a single PMT device, the amplitude and time of arrival of the signal is used to count the detector track multiplicity. In the case of fibre and MAPMT, however, the signal from a single tube coupled to different MAPMT channels are summed to calculate the multiplicity of the tube. In this procedure, the MAROC chip [61] is used for frontend readout to process the MAPMT signals and help to reduce background.

As shown in Fig. 5.16, the $\sim$ 5 m optical fibres are coupled to the MAPMT's on top of the shielding, while all the cables are routed from LUCID region to USA15 where the VME crates housing the backend readout are deployed. The length of the path in between is $\sim$ 80-100 m, as shown in Fig. 5.17.

In the case of PMT readout of the Cerenkov tubes, signals from the PMT are fed into an amplifier in order to provide the necessary signal strength. The differential output of this amplifier is sent to USA15 via twisted pair shielded cable. The received analog signal is then processed by a ROD (ReadOut Driver) card. The multiplicity per tube is evaluated by LUT (Look-Up Table), combining time of arrival and amplitude information. The result is stored in pipelines to be read pending a L1A (Level 1 Accept signal) and sent directly to the trigger card.

Online luminosity scalers are implemented in the logic and readout via

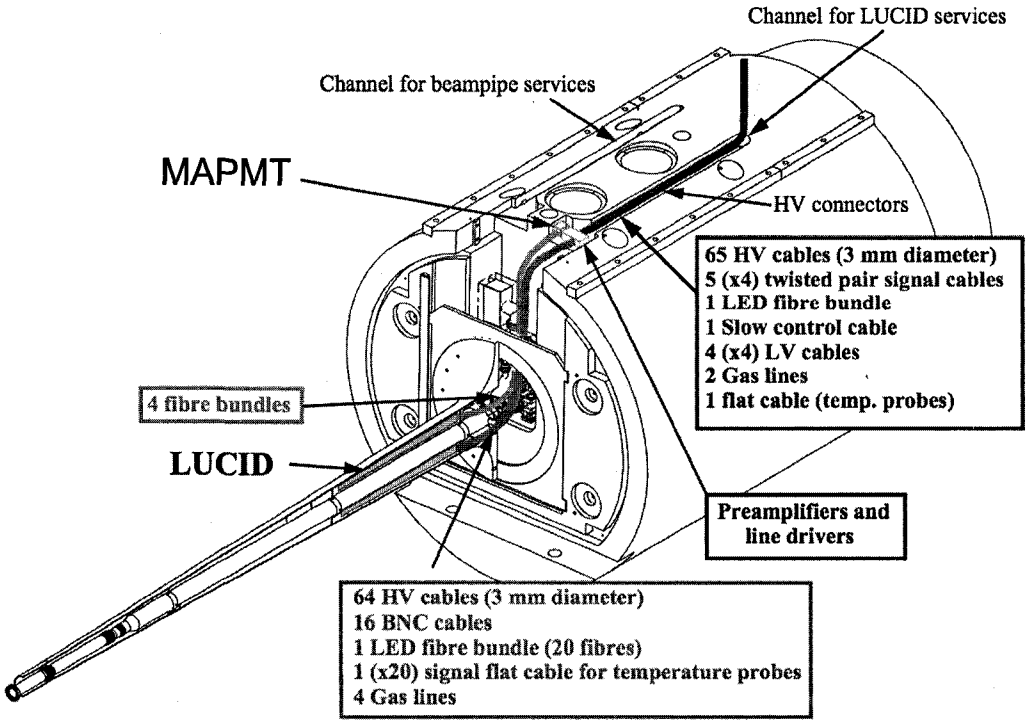

Figure 5.16: *Cable Connections of LUCID.*

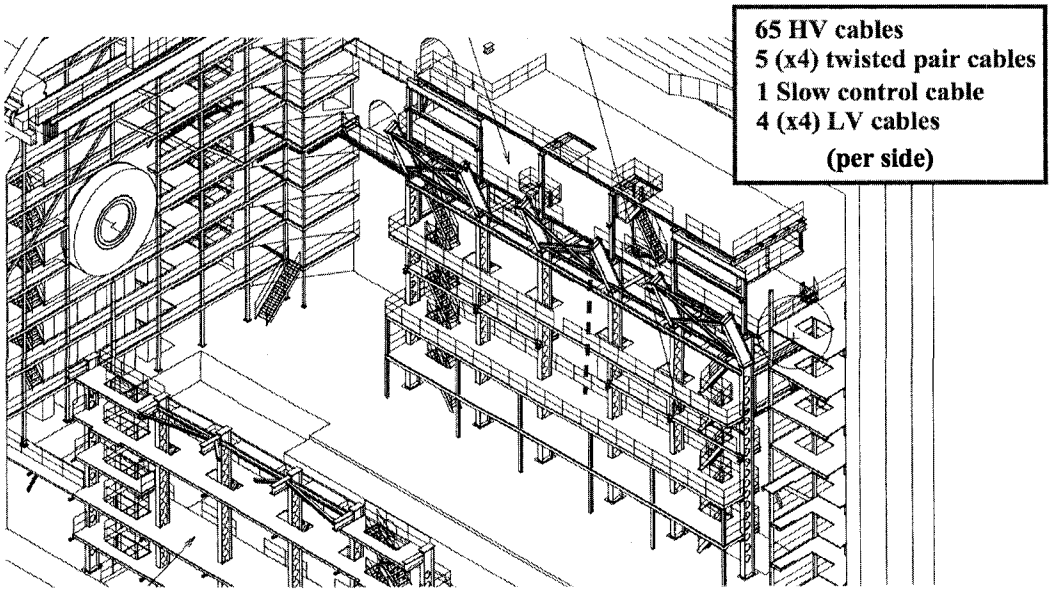

Figure 5.17: *Cable routing of LUCID.*

VME. The processed data, stored in a pipeline, are sent to ROS pending a L1A and form part of the LUCID event.

5.4 Radiation Environment of LUCID

The total ionizing dose and the neutron flux predicted for high luminosity are shown in Fig. 5.18 and Fig. 5.19, respectively. The radiation environment at the LUCID detector is substantial for Phase I and severe for Phase II. For Phase II, the total ionizing dose is at 10^5 Gy/yr and there is a flux of 10^{13} neutrons (1 MeV equivalent) per $(\text{cm}^2 \cdot \text{yr})$ through the same region. For Phase I, since LHC operates at a luminosity which is one order of magnitude smaller than the full luminosity, thus the expected radiation dose is roughly one order magnitude smaller. However, it is still severe enough to be a challenge to the detector design. It is important that all aspects of the LUCID

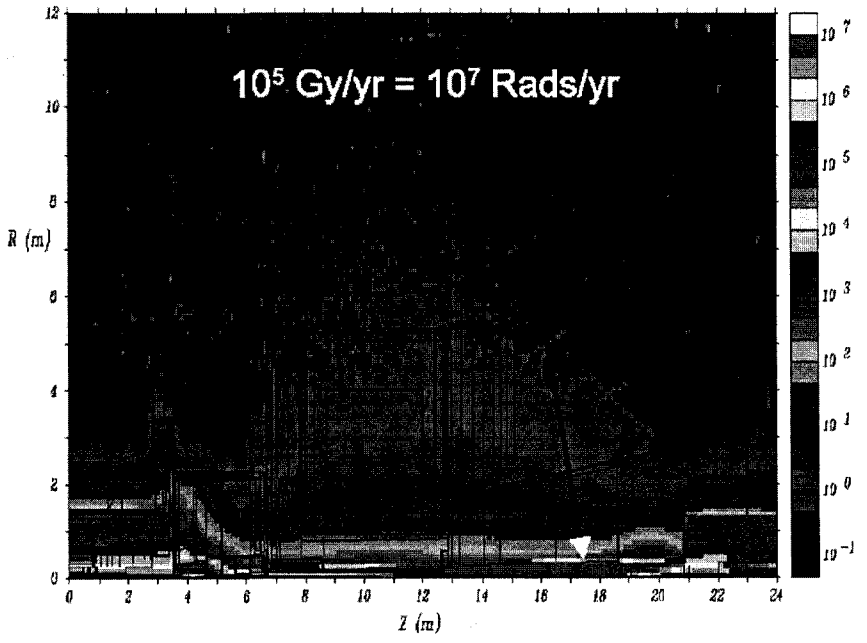

Figure 5.18: *The ionizing radiation environment of ATLAS measured in Gy/yr (TID). The LUCID region as pointed out suffers an annual dose of* 10^5 *Gy/yr.*

detector, including the optical fibres, PMTs, and electronics undergo radiation testing, in order to ensure that they will operate correctly in the high radiation environment.

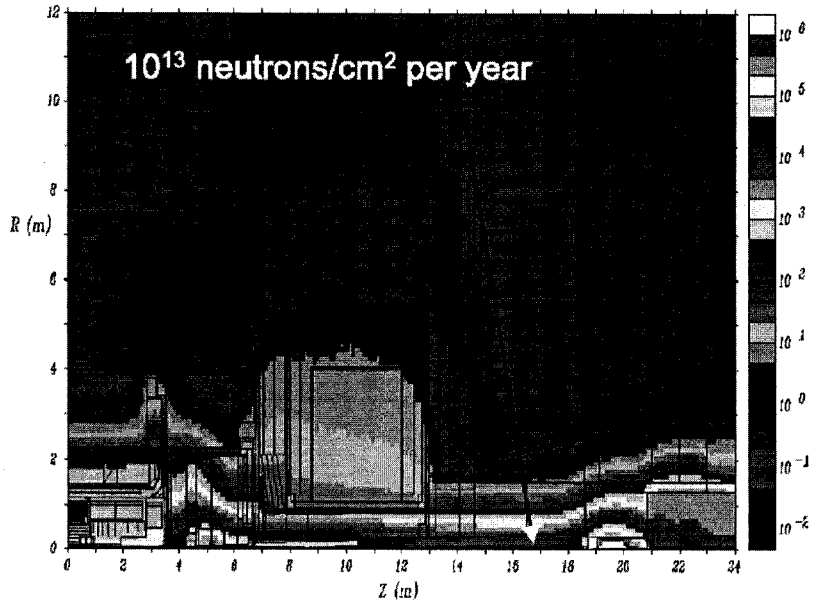

Figure 5.19: *The neutron flux ($E_n > 100$ keV) throughout the ATLAS experiment measured in KHz/cm^2. The neutron flux through the LUCID regions is shown at around $10^{13} neutrons/cm^2$ (1 MeV equivalent).*

The first radiation test on the PMT was performed in January 2007. A PMT was irradiated at the National Laboratory in the UK by γ's produced from ^{60}Co at an average dose at 1.1 MRad/hour, for a total dose of 20 MRad, which equals a three year running period under the full luminosity (Phase II conditions). The result shows that performance of the PMT remained within an acceptable range.

Another radiation test was performed in June 2007. A U^{235} source was used in a 1.5 hour exposure to give a total flux of 10^{14}neutrons/cm^2 which corresponds to at least 5 - 10 years of full luminosity run. Results show that passive materials were not substantially damaged by this intense flux of neutrons: fibres and quartz had no change in colour; cable and base of PMT had no breakdown; and, only a slight decrease in the elasticity of the O-ring was observed. It was also shown that the performances of the PMT remained within an acceptable range [62].

5.5 Calibration of LUCID

LUCID will be calibrated in three stages. In early LHC running, when no other luminosity information is available, LUCID will be calibrated with reference to the LHC beam parameters. A precision of $\sim$ 10% is expected. At the second stage, after some experience has been gained with ATLAS data taking, LUCID will be calibrated according to the luminosity measured from physics processes (W/Z, $\gamma\gamma \rightarrow \mu^+\mu^-$, etc.), a 5$-$10% error is expected after this stage of calibration. In later 2009 or early 2010, when the Roman Pot detector is installed, LUCID will be calibrated with Roman Pot data, where a precision of 2-3% is expected to be eventually obtained.

The calibration of LUCID using the ALFA detectors deployed in Roman Pots will be based on the elastic scattering data in the Coulomb region. The elastic scattering data (as described in the Chapter 4) will be recorded at a luminosity of $10^{27}\,\mathrm{cm}^{-2}\mathrm{s}^{-1}$ and the luminosity monitor will be calibrated at this luminosity. After calibration, LUCID will run under the normal luminosity range of $10^{33} - 10^{34}\,\mathrm{cm}^{-2}\mathrm{s}^{-1}$. Thus the calibration has to be carried over six to seven orders of magnitude, from running conditions with 2×10^{-4} interactions per bunch crossing to about 5 ($2 \times 10^{33}\,\mathrm{cm}^{-2}\mathrm{s}^{-1}$) interactions per bunch crossing (Poisson average) for Phase I, and 20 interactions per bunch crossing for the Phase II detector. These numbers illustrate the two main requirements for any luminosity monitor to be calibrated via special low luminosity runs: there has to be very good background rejection to avoid counting of fake interactions at low luminosity and there has to be a dynamic range of at least 5 (20 for Phase II) to avoid saturation of the monitor at high luminosity.

The design of LUCID addresses both these requirements. Using Cerenkov tubes pointing to the interaction points aids greatly in the rejection of low energy secondary particles, thus making LUCID more sensitive to primary and hard secondary particles that point to the interaction point. Furthermore, if the background levels permit, it will be possible to separate the one and two particle peaks in the amplitude distribution from each single tube. This will allow counting of particles instead of counting only hits. Particle counting will be necessary to avoid saturation at high luminosity, obtain the necessary dynamic range, and ensure the optimum linearity of response. Detailed

performance on this topic is covered in Chapter 7.

5.6 Simulation of LUCID

A full GEANT4 simulation of the LUCID detector was developed in order to study the detector performance and the detector design. This involved a simulation of the full path of the interaction products from the collision point to the LUCID detectors; the interaction and/or energy loss of the these particles in the detector; tracking of the Cerenkov photon produced by the particle in LUCID, including optical reflection, refraction and Rayleigh reflection; and the efficiency of the PMT/MAPMT for the detection of photons.

The test beam simulation software simulates the setup of the LUCID test beam experiment at DESY. In this case, the test beam vessel and the PMT/fibre tubes are included. Once the parameters are determined from the test beam experiments and the test beam simulation, they can be used in the full LUCID simulation to study the performance of the full LUCID detector. The details of the test beam simulation setup and results will be presented in the following chapter.

In the case of full LUCID simulation, the software implements the whole detector, for both Phase I and Phase II. The detector is put into the real radiation environment of ATLAS by connecting it to a full ATLAS simulation. The purpose of this work is to study the performance of LUCID as a luminosity monitor - understand the background from secondary particles, estimate systematic errors and study the installation and calibration scenarios. This study is reported in Chapter 7.

5.7 Integrating LUCID into ATLAS Data Chain

The data flow through ATLAS (including simulation as well as the real detector) is shown in Fig. 5.20. The end user only utilizes the reconstructed files (ESD/AOD) for physics analysis. These files contain the information of the reconstructed particles (e.g. muons, electrons, photons and jets). To study the performance of different parts of the detector, a simulation of the major parts of the ATLAS detector has been developed by the ATLAS collabora-

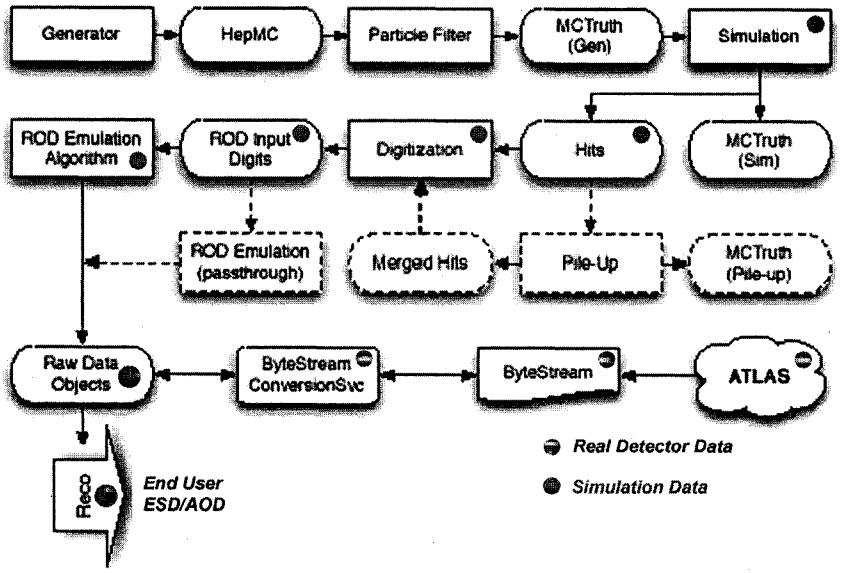

Figure 5.20: *Data flow of ATLAS.*

tion. The simulation starts from the physics event generators that simulate the physics processes in which we are interested. These generators produce the final state particles in the pp collision. The final state particles are passed to the GEANT4 simulation of ATLAS, where they generate hits in different parts of the detector. The results of the hits are passed to digitalization process where the hits in separate detector parts are combined together to generate the digitalized data (for example, how much light is collected in a calorimeter channel, or what is the pulse amplitude in a pixel detector channel). The digitalized data are converted to Raw Data Object (RDO) format before they are passed to the reconstruction process, where the responses of different detector parts are combined to determine the track of the particles, identify particles, calculate their 4-momentum, etc. In the reconstruction process, the end user files are produced.

In the case of the ATLAS detector (not the simulated one), final state particles are generated in real interactions. Different parts of the detector detect the particles and the same RDO format data is produced. The same reconstruction procedure is used to produce the end user files for physics studies.

The LUCID detector produces luminosity information on an event by event basis. This information is transfered into the ATLAS data chain. LUCID

also provides luminosity information for each luminosity block in the offline condition database of ATLAS.

The simulation of LUCID is currently being integrated into the full simulation data chain of ATLAS. This work includes the ATLAS GEANT4 simulation which produce the hits, the digitalization process of LUCID hits, and the LUCID reconstruction procedure where the response of LUCID is summarized and the results are stored for end user access.

The differences between the integrated LUCID simulation and the full LUCID simulation (mentioned in the previous section) are:

- The full LUCID simulation is a standalone GEANT4 program. The integrated simulation is developed under ATHENA - the ATLAS general computing framework.

- To simulate the ATLAS environment, the full simulation utilizes another program to simulate the ATLAS detector and passes the information to LUCID. While in the integrated simulation the simulation of LUCID, as well as other parts of ATLAS, are implemented in the same program.

Chapter 6

LUCID Test Beam and Bench Test Experiments

6.1 Introduction

Three test beam experiments were performed on Oct. 2005, July 2006 and Dec. 2006 at DESY's beam area 22, in order to study the performance of the LUCID detector prototype. An electron beam with maximum energy of 6 GeV was employed in these experiments. The main goals of these experiments were to:

- Compare basic parameters of the performance of LUCID with the simulation;
- Test the performance of electronics;
- Measure the angular dependence of the signal from the Cerenkov tubes;
- Measure the variation in signal with radiator gas pressure;
- Test mechanics, including design of tubes, light collectors, vacuum sealing methods, etc.

In the first test beam experiment a prototype of the fibre design read out by a MAPMT was deployed. The second test beam experiment included an improved light collection method for the fibre design. This test also included Cerenkov tubes read out via a PMT placed on the exit aperture. The third

test beam experiment focused on the testing of the performance of the PMT readout design.

In addition, test facilities were setup at CERN and at the University of Alberta to enable the reflectivity of the aluminum tubes and light collectors to be measured. These test facilities were used to assess polishing procedures for the Cerenkov tubes and to measure input parameters for the simulation (reflectivity, polish, etc).

6.2 Bench Test Setup

The CERN Bench Test facility is shown in Fig. 6.1, a red laser at 633 nm is used as the light source. The laser beam is directed in to the tube by a prism. A 11 mm diameter silicon photo-diode light metre was placed at the far end of the tube. As the prism rotates, the laser beam enters the tube with different incidence angles, producing 1, 2, 3, 4 or more reflections. The light metre measures the power of the laser beam after a certain number of reflections. In this way the reflectivity of the aluminum tube can be determined. A

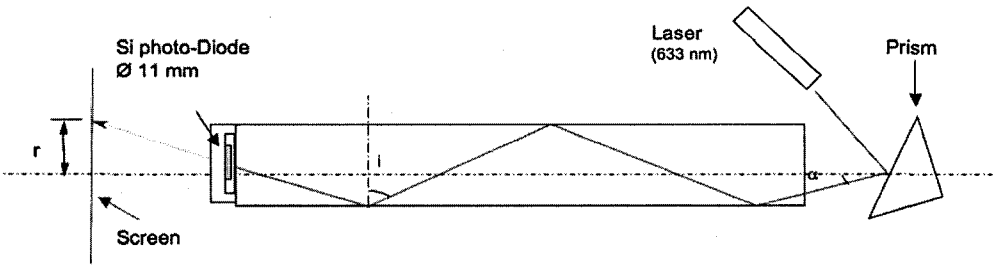

Figure 6.1: *Bench Test Experiment Setup*

photograph of the test setup is shown in Fig. 6.2.

Another bench test facility was available at the University of Alberta. In this case the setup utilizes blue and UV lasers. With the combination of these two bench test facilities, the reflectivity of the tubes can be measured with red, blue and UV light. The test result are shown in Fig. 6.7.

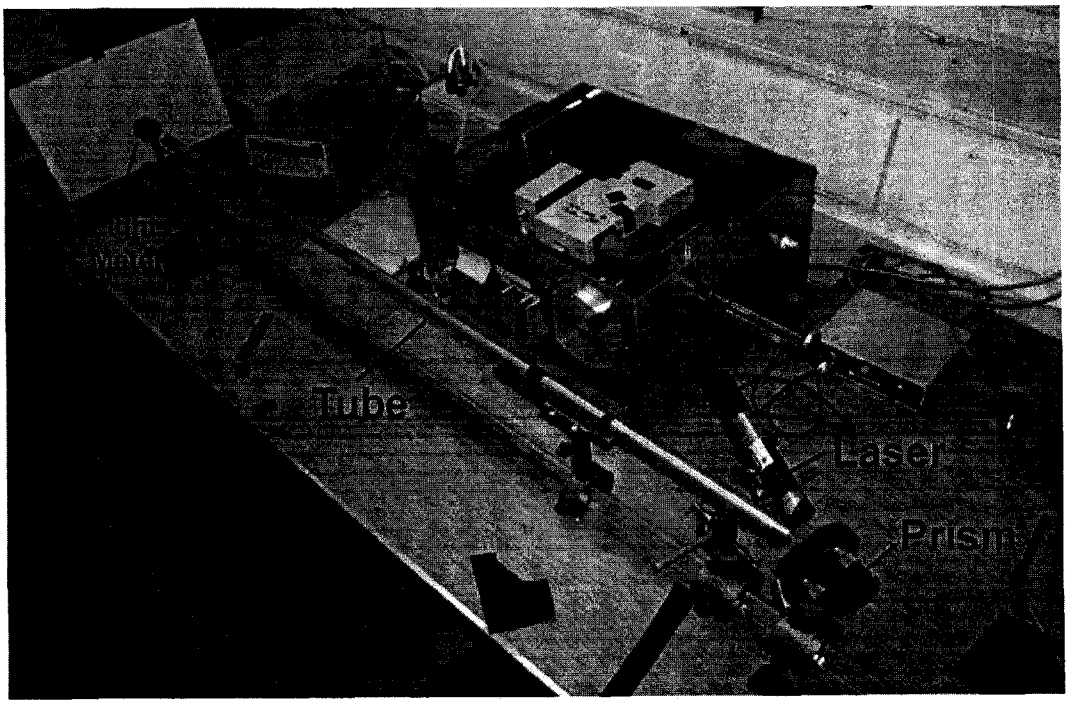

Figure 6.2: *Picture of the bench test experiment*

6.3 Test Beam Experiment and Simulation Setup

6.3.1 Test Beam Experiment Setup

The same test vessel and vacuum system were used in all three experiments. The test setup is sketched in Fig. 6.3 (top). The beam passes through three small (0.5 cm thick, 5×5 cm in size) scintillator detectors and three silicon strip tracking detectors before it reaches the test vessel. The scintillator detectors are used to trigger the test system. The silicon strip detectors are placed in the x and y directions to measure the position and angle of the incoming electron. The pitch of the silicon strips is 50 μm.

The test vessel is placed on a table that can move in the horizontal or vertical directions with an accuracy of 0.1 mm. The vessel itself can rotate in the horizontal plane within the range of $\pm 10°$. Six Cerenkov tube detectors were installed in the vessel. The test vessel is connected with a gas system that supplies the Isobutane or C_4F_{10} radiator gas at a certain pressure, ranging from 1 to 2.5 bar. In the case of a Cerenkov tube read out by a PMT, the PMT is directly mounted at the end of the light collector (cone). In the case of

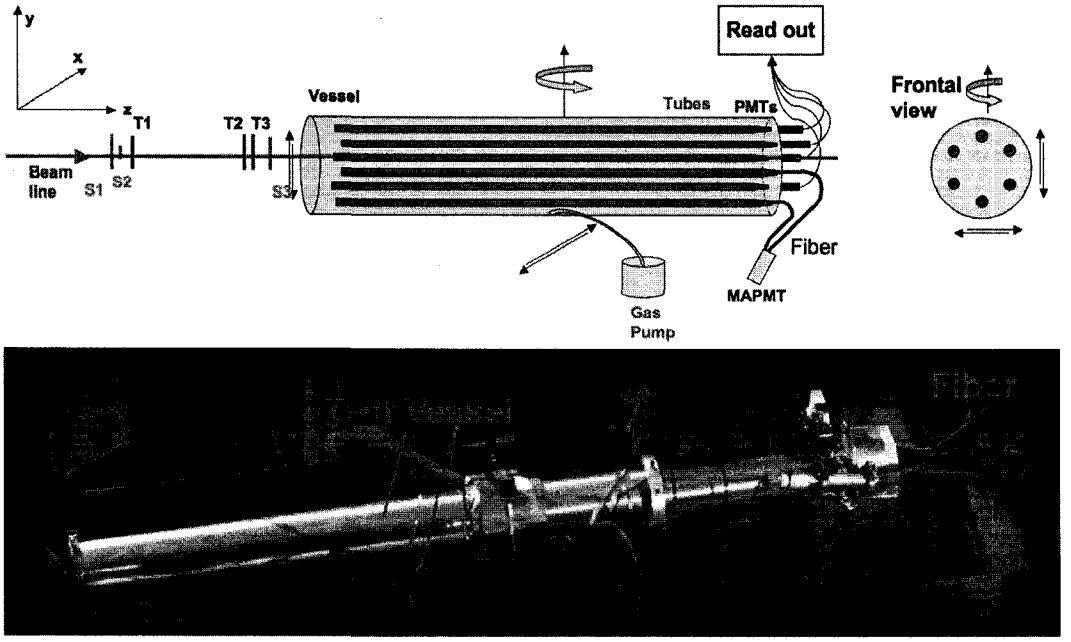

Figure 6.3: *Sketch (top) and photograph (bottom) of the test beam setup at DESY.*

a fibre readout detector, the fibre bundle connects the light collector Winston Cone with the MAPMT.

The PMT and MAPMT output signals are collected by a VME based DAQ system and sent to a computer through a high speed data fibre. The detailed setup of Cerenkov detectors in each test beam experiment is listed in Table 6.1.

6.3.2 Simulation Setup

In the GEANT4 testbeam simulation program, the setup of the experiment is simplified as shown in Fig. 6.4. The simulated detector can be a PMT readout detector or a fibre readout detector. The scintillators and silicon strip detector material is modeled in the simulation. By doing this, the scattering of the incoming electrons in those materials can be simulated. The position and angle of the incoming electrons are calculated in the program.

The scattering of electrons on the side of vessel is not significant in the experiment because all incoming electrons come from the front and hit the front of the vessel at a near 90° angle. For this reason, the test vessel is also

	Tube	Cone	Tube W/fibre	Tube W/PMT	fibre Type	PMT Type
Oct. 2006	MP	3mm WC	6	0	Plastic HUV1000	N/A
July 2007	MP AM	3mm WC 4mm WC	4	2	PUV700 FSU	HAM R2469
Dec. 2007	MP AM	8mm WC 8mm NC	0	2	N/A	HAM R2469

Table 6.1: *List of detectors in each test beam experiment. MP: Mechanically Polished Tube; AM: Tube with Aluminized Mylar; 3 mm WC: Winston Cone with 3 mm output aperture; 8 mm NC: Normal (straight) Cone with 8 mm output aperture. FSU, HUV and PUV are fibres produced by Ceram Optics.*

simplified and the whole vessel replaced by a plastic cover in front of the tube.

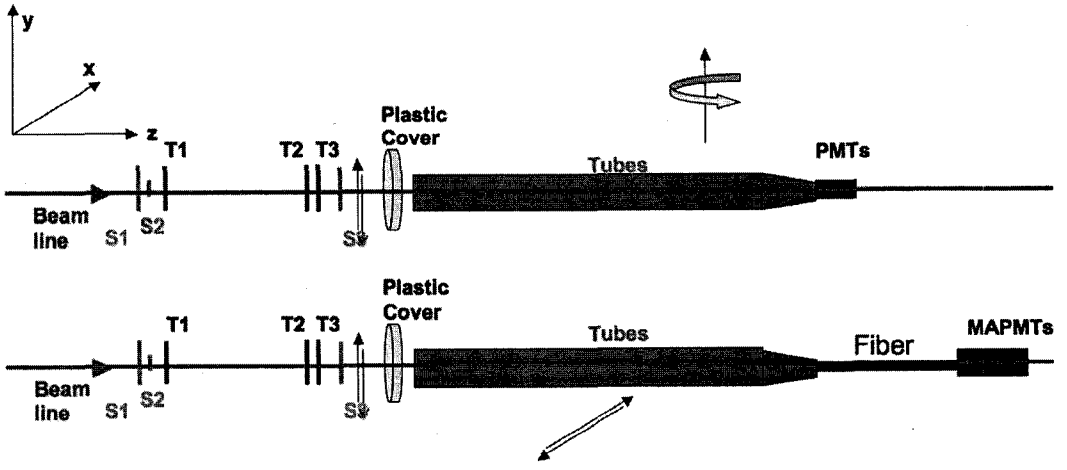

Figure 6.4: *Setup of the test beam simulation. PMT readout detector (top) and fibre readout detector (bottom).*

6.3.3 Simulation Parameters

The main task of the simulation is to specify and validate the operating parameters of the detector. The parameters of interest are as follows.

- Radiator gas refractive index and absorption length, as a function of wavelength, shown in Fig. 6.5 (Isobutane).

- Aluminum reflectivity as a function of wavelength.
- The refractive index of the fused silica readout fibre (core and cladding), as a function of wavelength. The refractive index of fused silica core is shown in Fig. 6.5 (Quartz). In the simulation, a constant numerical aperture is assumed over all wavelengths. The corresponding refractive index of the fibre core is calculated from NA and the refractive index of the core at a certain wavelength ($NA = \sqrt{n_{core}^2 - n_{clad}^2}$). Different NA's from 0.3 to 0.4 are used in the simulation.
- The absorption length of the fused silica fibre as a function of wavelength, as shown in Fig. 6.6.
- The refractive index of the PMT window, as a function of wavelength. It is assumed that the PMT window has the same refractive index of the fused silica fibre core, as shown in Fig. 6.5 (Quartz).
- The PMT quantum efficiency as shown in Fig. 6.5 (PMT).

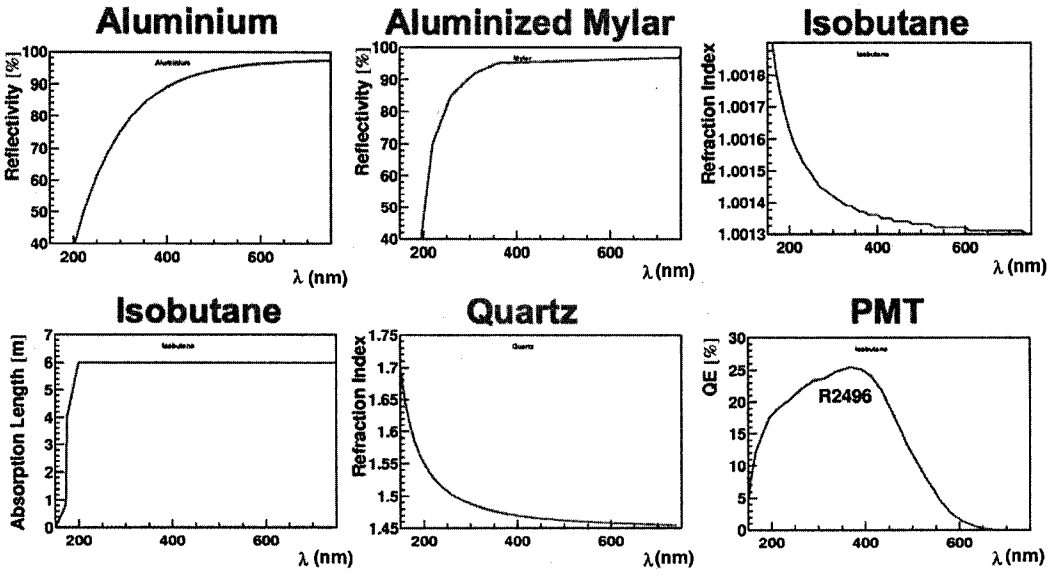

Figure 6.5: *List of simulation parameters.*

The refractive index of C_4F_{10} can be written as [63]

$$\frac{n^2-1}{n^2+2} = \frac{0.152P}{13.5^2 - E^2} \times \frac{308}{T}, \tag{6.1}$$

where n is the refractive index, P is the pressure of the gas in bar, T is the gas temperature in degrees Kelvin, E is the energy of the photon in eV. From the Particle Data Book [10], under STP conditions (273 K and 1 bar), the refractive index of Isobutane for 590 nm light is 1.00190. The refractive index for different wavelength, pressure and temperature can be calculated. Since n is very close to 1, we take the approximation that $n+1 \simeq 2$ and $n^2+2 \simeq 3$, from Eq.6.1, we have

$$n - 1 \simeq \frac{3}{2} \times \frac{0.152P}{13.5^2 - E^2} \times \frac{308}{T}. \tag{6.2}$$

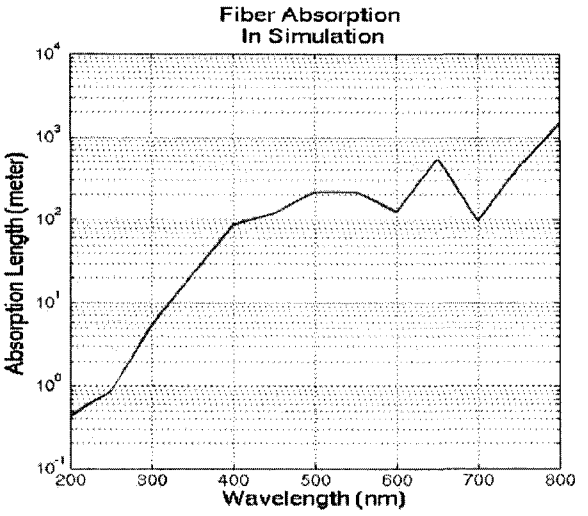

Figure 6.6: *Absorption of the fibre core as a function of wavelength.*

The value of reflectivity of Aluminum, as a function of wavelength, used in the simulation is obtained from the literature [64] and from bench test measurements (Fig. 6.7) while the reflectivity of Aluminized mylar was measured in a bench test at three different wavelength. The reflectivity at other wavelengths is obtained from a rescaled reference curve (Fig. 6.7 right).

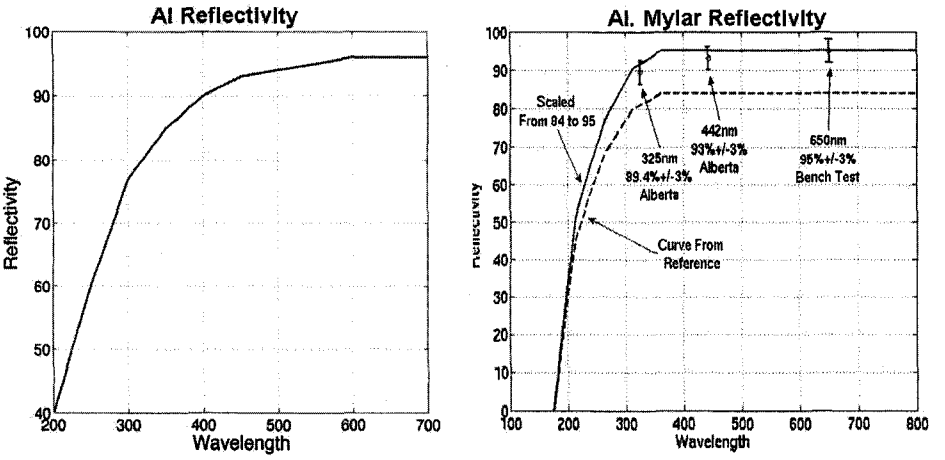

Figure 6.7: *Reflectivity of pure aluminum (left) [64] and reflectivity of Aluminized Mylar [65].*

6.4 Test Beam Results and Simulation

6.4.1 Result from PMT Readout Detectors

Shape of the Beam Profile

The electron beam aperture in the DESY beam area 22 beam line is shaped by a 8 × 8 mm collimator. Before beam electrons enter the Cerenkov tube, their position and angle are measured by the silicon strip trackers. A typical beam position profile is shown in Fig. 6.8. The electron beam size measures 8 by 9 mm primarily due to scattering in the collimator. The beam is approximately evenly distributed in both X and Y directions with slightly more electrons coming from the centre.

Shape of a PMT Signal

Since the PMT is directly mounted on the far end of the Cerenkov tube, a particle traveling down the full length of the tube may also traverse the PMT window. As the diameter of the PMT (8 mm) is smaller than the diameter of tube (17 mm), incoming electrons can be divided into three groups, as shown in Fig. 6.9 (bottom left), where: 0) the electron traverses outside the tube and PMT; 1) the electron traverses inside the tube but exit the tube

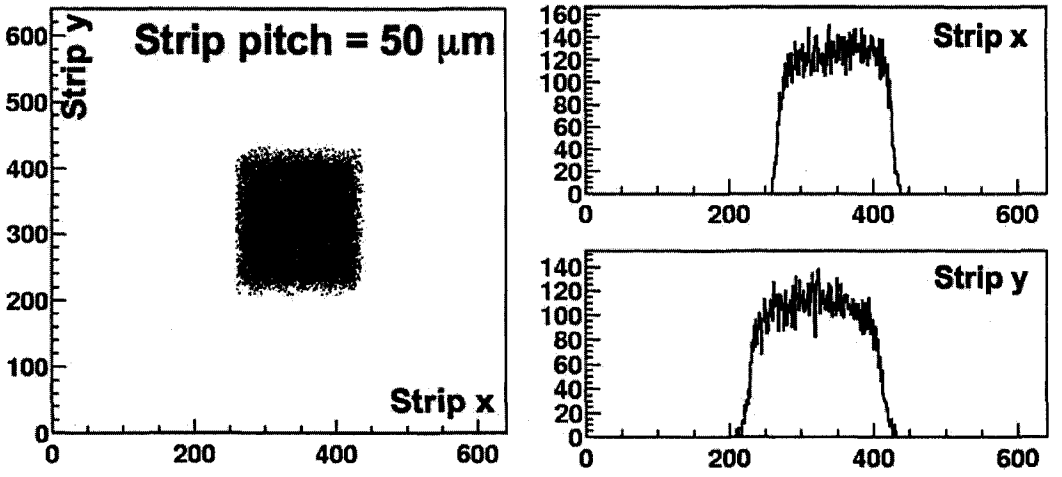

Figure 6.8: *Shape of the beam profile, one strip unit in the x or y direction corresponds to 50 μm.*

without entering PMT; 2) the electron traverses inside the tube and later passes through the PMT.

Cerenkov photons are produced when the electron traverses the Cerenkov tube. However, when an electron passes through the Quartz PMT window, Cerenkov photons are also produced. The discrimination of the photons produced in the PMT window from those produced in the gas is a crucial part of the data analysis.

A typical ADC distribution for a test run is shown in Fig. 6.9 (left). The peak P_0 is due to the noise from trigger and electronics when no Cerenkov light is produced in the Cerenkov tube (case 0 above). Peak P_1 comes from the electrons that produce light only in the gas tube (case 1). Peak P_2 represents case 2 when the electrons produce light both in gas and PMT window. This data is taken at the Dec. 2006 test beam.

In the case where there is no gas in the Cerenkov tube, as shown in Fig. 6.9 (right), both case 0 and case 1 produce no light and give a peak P_0, while case 2 produces a small amount of light in the PMT window which corresponds to P_2.

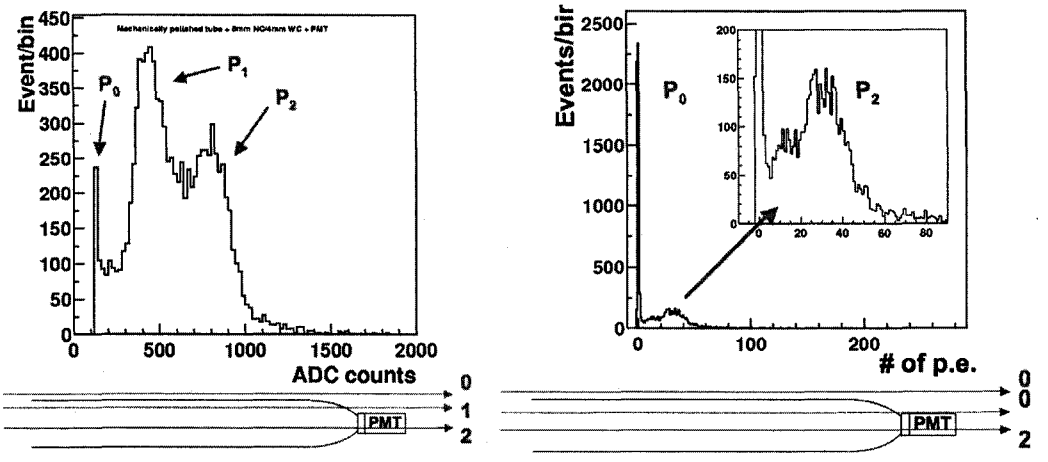

Figure 6.9: *ADC distribution of a test run with gas radiator (left) and photo-electron distribution of a test run under the same condition without the gas radiator (right).*

Silicon Tracker

Due to the materials in front of the detector, a scattered electron sometimes traverses only part of the Cerenkov tube and gives less light. It can also interact with the aluminum tube to produce unwanted background. For this reason, the selection of electrons from it position and angle is very important.

Fig. 6.10 shows an example in which, by selecting the electrons that travel down the length of the tube, the height of P_1 and P_2 rise dramatically. Much more light is produced with these electrons than those that exit the tube or travel very near to the edge of the tube.

Analysis of PMT Signal

The gain of the PMT is determined from the single photo-electron calibration. A small amount of LED light is introduced into the front of the Cerenkov tube via an optical fibre. A calibration run is taken when the LED light is low enough to give only one photo-electron. From this run, the relation between the ADC channels and number of photo-electrons can be determined. This calibration is used for the analysis of real data.

For each data run, after pedestal subtraction, and after calibration which converts ADC counts into number of photo-electrons, the histogram is fitted to three Gaussian distributions, as shown in Fig. 6.11. The three Gaussians

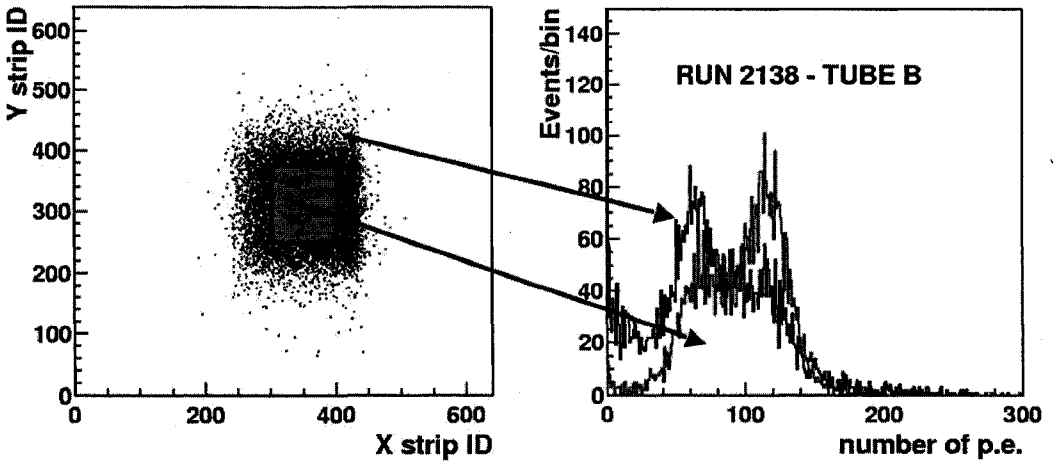

Figure 6.10: *Effect of electron selection by the silicon tracker. By selecting the electrons that travel down the whole length of the Cerenkov tube (red part), the background is greatly suppressed and much more light is produced.*

correspond to peak P_1, P_2 and background.

For a typical run with the gas pressure of 1 bar, the mechanically polished aluminum Cerenkov tube gives $\sim$ 50 photo-electrons when the electron traverse the tube but not the PMT window, and $\sim$ 100 photo-electrons when the electron traverse both tube and PMT window. Which lead to a conclusion that the PMT window contribute $\sim$ 50 photo-electrons.

Consider now, the mylar lined tube, as the reflectivity of aluminized mylar is better than that of pure aluminum, the first peak is at $\sim$ 67 and the second peak at $\sim$ 114. Note that the difference between the two peaks is $\sim$ 50 which is consistent with the mechanically polished tube case - the same PMT window contributes the same amount of photo-electrons in both cases.

By subtracting the 50 photo-electrons produced in the PMT window when necessary, we can draw a conclusion that at 1 bsar, with the same straight 8 mm cone and the same PMT, the mechanically polished tube gives on average 52 photo-electrons and the aluminized mylar tube gives on average 67 photo-electrons.

The performance of the mylar lined tube was slightly superior to that of the mechanically polished aluminum tubes. As the mechanically polished tubes were more robust, reliable and easier to produce, and the mylar lined tube could be damaged by the high temperature during the beam pipe bakeout,

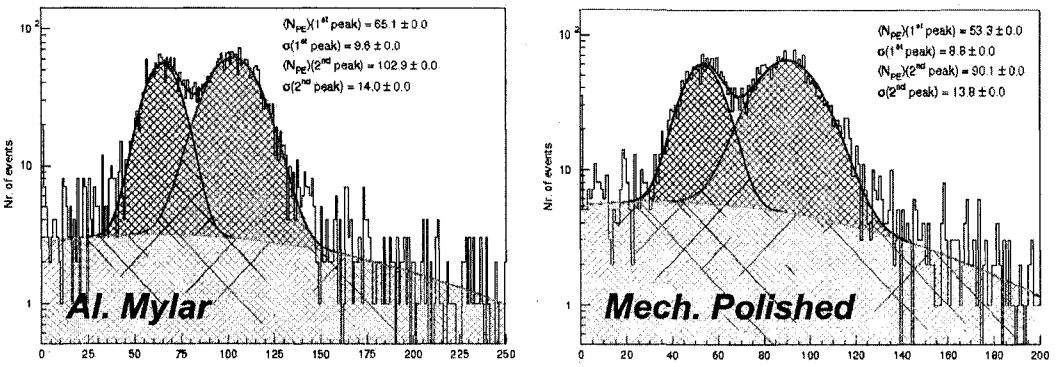

Figure 6.11: *Amplitude Distribution from the PMT readout detector.* $(N_{PE})(1^{st}peak)$ *and* $(N_{PE})(2^{nd}peak)$ *are the number of photo-electrons of the first and second peak.* $(\sigma)(1^{st}peak)$ *and* $(\sigma)(2^{nd}peak)$ *are the width of the first and second peak, respectively.*

the option of mechanically polished tubes in LUCID was chosen.

Pressure Test

A pressure test is carried out by changing the gas pressure in the test vessel from near 0 bar (vacuum) to 2 bar. The refractive index (Eq. 6.1) and absorption length of the gas will vary with pressure. The test was performed for an aluminized mylar tube with a 4 mm Winston Cone (July 2006) and an 8 mm Straight Cone (Dec. 2006). The purpose of this test is to choose the optimal working pressure for the LUCID Phase I and II detectors. Fig. 6.12 shows the detector response under different pressures and the prediction of the Monte Carlo simulation.

Theoretically, the number of Cerenkov photons produced in the detector is proportional to the pressure of the radiator gas. However, at a higher pressure, the emission angle of Cerenkov photons is also bigger. From the Cerenkov theory, the Cerenkov emission angle β is defined as $cos(\beta) = 1/n$. At 1 bar in C_4F_{10} Cerenkov angle is 3°, while at 2 bar it is 5°. As the photons experience more reflections in the tube, thus more light is lost. This is one reason why the pressure response curve turns downward at high pressure (2 bar) instead of continuing on an upward curve. Another reason for this turn over is due to the acceptance angle of the Winston Cone (Normal Cone) and PMT. The acceptance of light arriving at a larger angle, with respect to the axis of the

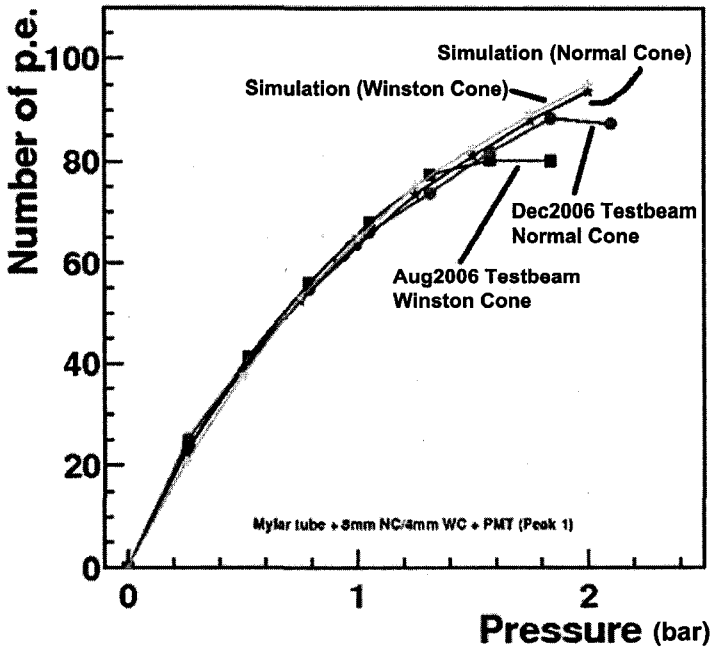

Figure 6.12: *Pressure test for the aluminized mylar tube showing a comparison of measured value with the Monte Carlo prediction. 10k events are taken for both simulation and test beam results.*

tube, is less than that of light arriving at smaller angle to the axis of the tube.

The simulation results agree well with the test results at pressures below 1.5 bar. At higher pressure, the Cerenkov angle is so large that some of the factors become more significant: direction of incoming electrons, misalignment in the mechanics, surface polish and reflectivity of the tube. Some of these effects were difficult to estimate. For example, a determination of surface polish, rather than reflectivity, would require an upgraded test facility that was not available. Another problem was the accurate determination of beam direction and the alignment of the mechanics with respect to the beam direction. In addition, the uniformity of reflectivity and polish was difficult to determine down the full length of the tube. These problems are being studied and will be included in later simulations.

The working pressure of the LUCID Phase I detector is chosen to be 1.3 bar for the following reasons:

- Pressures higher than 1.3 bar require a stronger gas vessel with a more complicated design. A stronger vessel would require more material and would thus increase the background level.
- At 1.3 bar the pressure of the gas is greater than ambient and minor leaks will not introduce impurities into the gas due to the pressure difference. Also, with an excess pressure it is possible to monitor for leaks with a pressure gauge.
- Running at the maximum pressure, given the above constraints, allows the light output to be maximized.
- The Monte Carlo simulation reproduces well the situation from 0 to 1.3 bar.

Angle Test

As mentioned in previous chapters, by using thin and long tubes (1.5 m), pointing at the interaction point of the beams in ATLAS, LUCID is most sensitive to particles coming from the direction of the interaction point. Secondary particles coming in at a larger angle will produce a much smaller signal

in LUCID. To study this property of the LUCID prototype an angle scan test was performed.

The LUCID test vessel sits on a rotatable plate. The plate is rotated from $-2.0°$ to $2.0°$ with a $0.25°$ or $0.5°$ step. The definition of rotation angle is shown in Fig. 6.13. Under a pressure of 1 bar the result of the angle test and the corresponding simulation result for both the mechanically polished tube and the aluminized mylar tube is shown in Fig. 6.14. These data are taken during the December 2006 test beam.

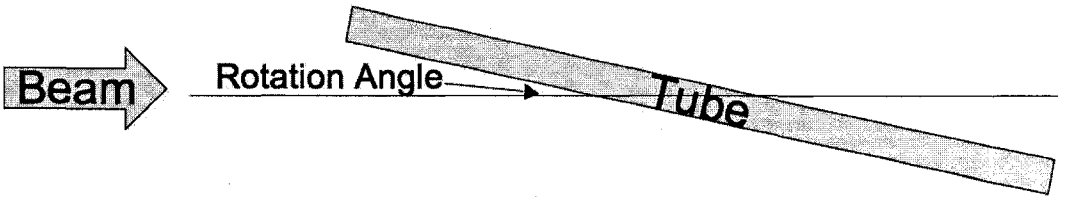

Figure 6.13: *Definition of test angle.*

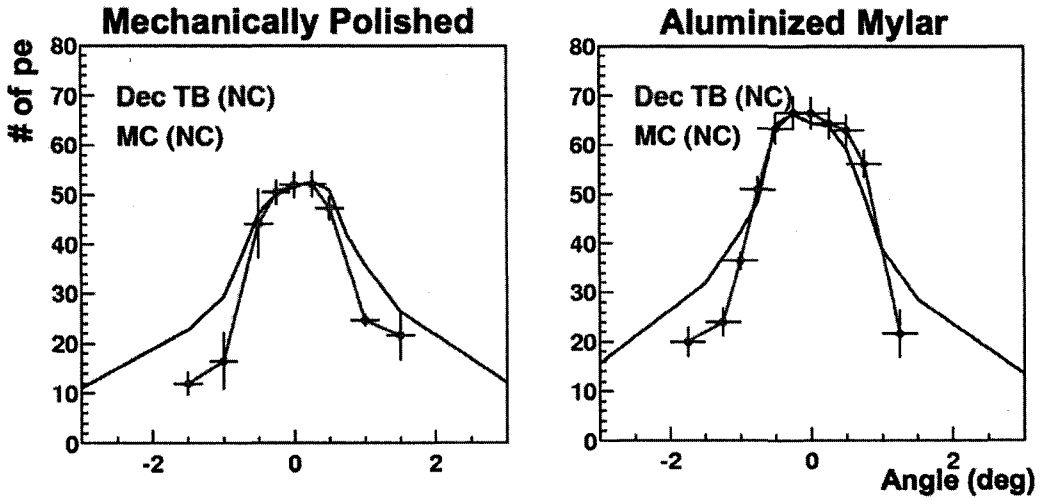

Figure 6.14: *Angle test results comparison with simulation.*

The number of photo-electrons drops to much less than one half when the angle is 1°. This demonstrates LUCID's ability of suppressing non-pointing backgrounds. Simulation results agree with test results at smaller angles. The discrepancy at higher angles is explained in the following section.

6.4.2 Results from Fibre Readout Detectors

Test Setup

The test beam experiments also include tests for fibre readout detectors. In the fibre readout detector case, the light is collected by a Winston Cone or conical light collector, and then transferred to an optical fibre bundle. The fibre bundle is connected to a MAPMT where the light is converted to an electric signal.

6.4.3 Winston Cone

The shape of a Winston Cone is given by [60]:

$$(rcos\theta+zsin\theta)^2+a'r(1+sin\theta)^2-2a'zcos\theta(1+sin\theta)-a'^2(3+sin\theta)(1+sin\theta)=0, \tag{6.3}$$

where $r=\sqrt{x^2+z^2}$. Fig. 6.15 shows a schematic diagram of a Winston Cone and the coordinate system used.

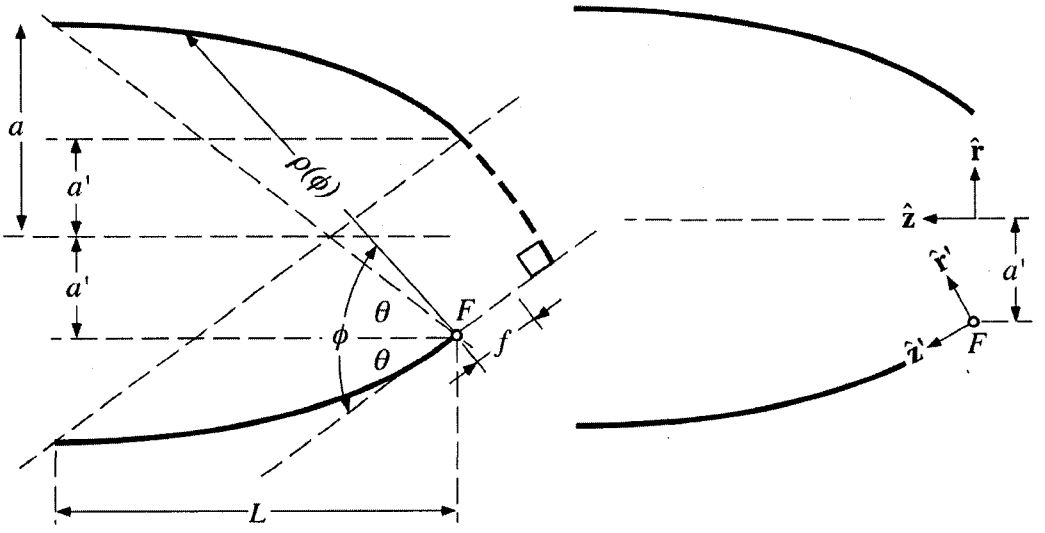

Figure 6.15: *Schematic diagram of a Winston cone light concentrator. The entrance and exit apertures are of radius a and a', respectively. F is the focus of the upper parabola segments, and f is its focal length. The length of the cone is L. The diagram on the right shows the origins and orientations of the focus-centered and symmetry axis-centered coordinate systems.*

In order to produce the Winston Cone used in LUCID, a is set to the inner diameter of the tube. Fig. 6.16 shows a Winston Cone design with input diameter 1.93 cm.

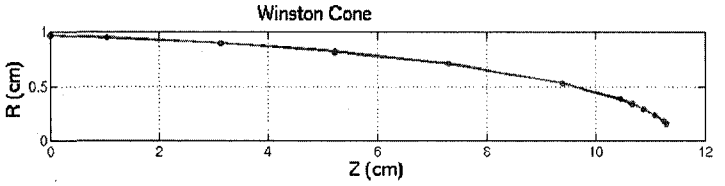

Figure 6.16: *Schematic diagram of a Winston Cone used in test beam.*

Simulation Parameters

To simulate the process of light entering the fibre bundle from the light collector, photographs of the cross section of different fibre bundles are taken. From these pictures (Fig. 6.17 top), the relative position of the fibres can be measured and then implemented in the simulation. Fig. 6.17 (bottom) shows the fibre bundle in the simulation, the outer circle is the exit aperture of the light collector.

Beside the geometrical setup of fibre bundles, other properties of the optical fibre (refractive index, absorption, numerical aperture) and MAPMT (quantum efficiency) is also included in the simulation.

Signal from a fibre readout detector

A typical ADC distribution for a test run is shown in Fig. 6.18 (top-left) at 1 bar. The peak on the left is due to the noise from trigger and electronics when no Cerenkov light is produced in the Cerenkov tube. Fig. 6.18 (top-right) shows the corresponding distribution of number of photo-electrons, after pedestal subtraction and combination of fibre channels. On average, $\sim$ 11.5 photo-electrons are collected in each event at a running pressure of 1 bar. After making the track alignment correction using the silicon strip tracking as

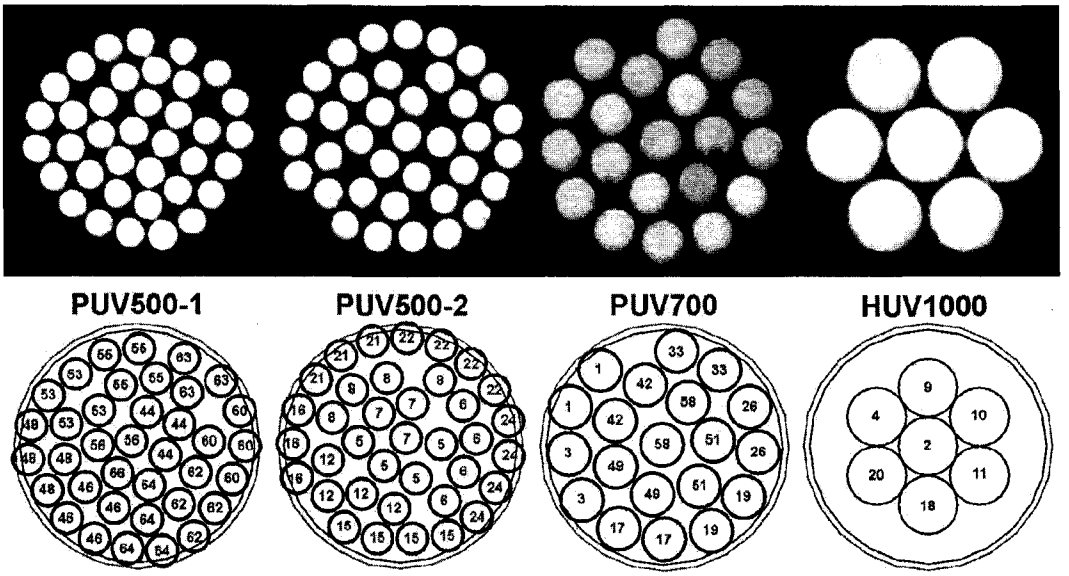

Figure 6.17: *Picture of fibre bundle cross sections (top) and the corresponding fibre bundles in the simulation (bottom). The fibre bundles are: two bundles of 0.5 mm PUV fibre (PUV500-1, PUV500-2), one bundle of 0.7 mm PUV fibre (PUV700), and one bundle of 1 mm HUV fiber. PUV and HUV are brand names of CeramOptics. The numbers shown in the bottom plots are the number of MAPMT channels the fibres are connected to.*

described in the previous section (Fig. 6.10), the number of photo-electrons is increased to an average of $\sim$ 13 per event, as shown in Fig. 6.18 (bottom). On average $\sim$ 60% of the events pass the silicon strip selection. By working at a pressure of 1.25 bar the number of photo-electrons detected in each tube can be increased to $\sim$ 15 as shown in Fig. 6.22.

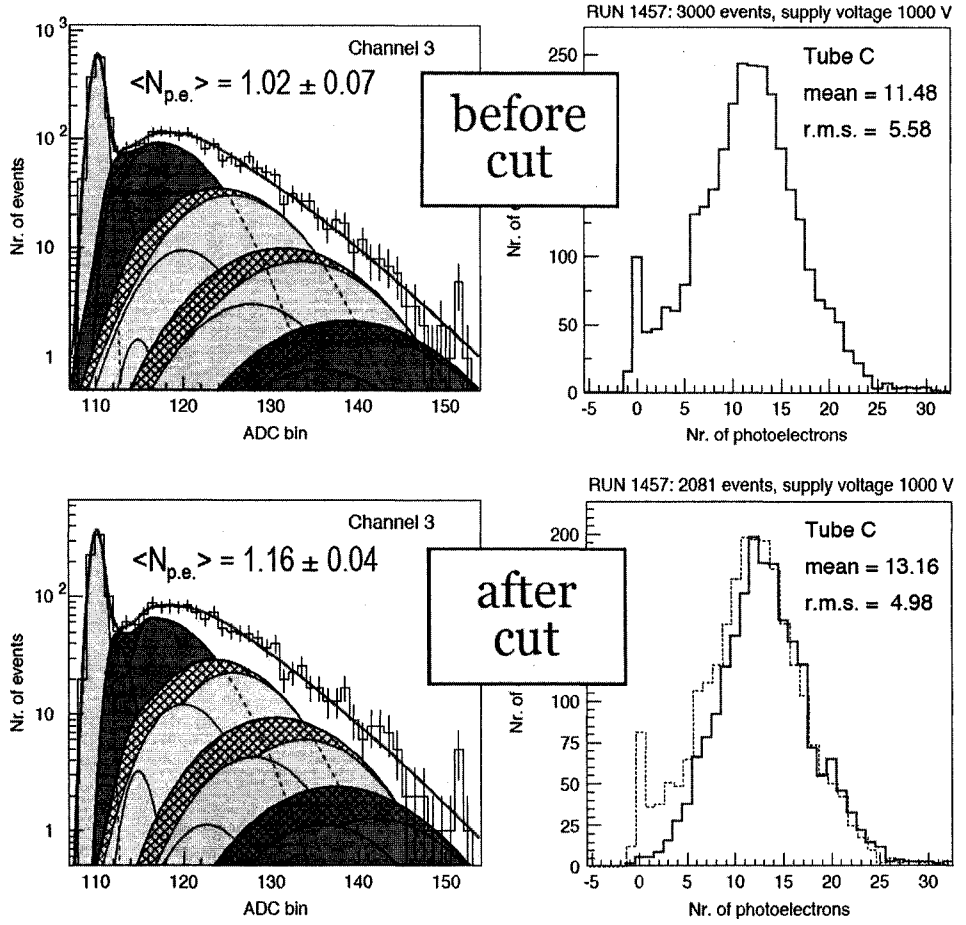

Figure 6.18: *(top-left): A typical ADC distribution of a test run; (top-right): distribution of number of photo-electrons; (bottom-left): the ADC distribution of the same run, selecting only the events when the electron hit the centre part of both silicon stripes; (bottom-right), the corresponding distribution of the number of photo-electrons with silicon stripe selection.*

Distribution of Photons at the Entrance to the Fibre Bundle

Fig. 6.19 (left) shows the distribution of the number of photons across the exit of the light collector. The plot shows the central fibre receives the most

light. Fig. 6.19 (right) shows the incident angle when the photon hits the fibre/light collector interface. A straight cone is used in this case[1]. Photons that have no reflection on the cone retain their initial angle (Cerenkov angle) as the first peak (0 bounce); the more reflections the photon experiences, the higher the angle at which it hits the fibre surface. For a fibre with NA = 0.37, the maximum acceptable incident angle is ~25°. Photons that experience more than three reflections in the reflector, mostly generated by non-interested background particles, are unlikely to enter the fibre even if they survived the reflection on the Aluminum surface.

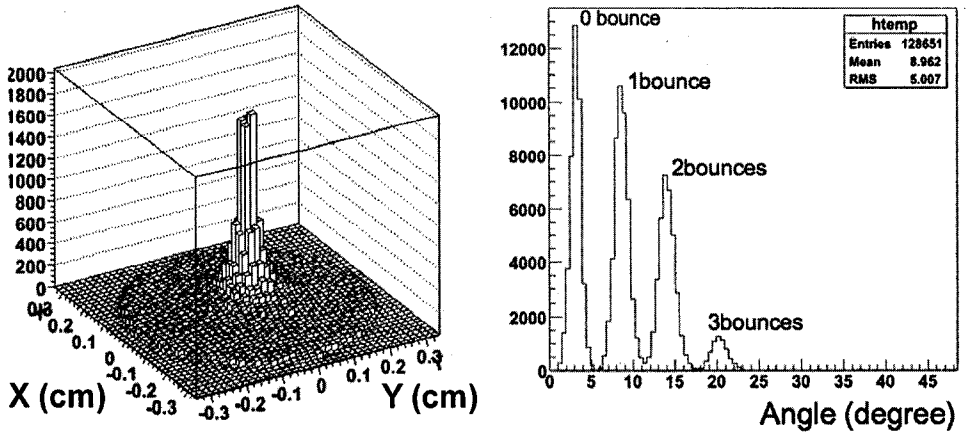

Figure 6.19: *left: lego-distribution of the number of photons arrive at the exit of the light collector (before entering the fiber); right: the angle distribution of these photons.*

Angle Test

An angle test is performed on the fibre readout detectors as on PMT readout detectors. Under a pressure of 1 bar relative, the detector is rotated from −5.0° to 3.0°. The result of the angle test in the December 2006 is shown in Fig. 6.20. The upper curve is obtained by applying the silicon strip selection to the lower curve. The curve is shown as an "envelope" instead of a simple line to indicate the statistical error in the experiment. The number of photoelectrons

[1]Both Winston Cone and Straight Cone are used in test beams, however, the results for Winston Cones is not presented due to the choice to use Straight Cone for final LUCID production, because Straight Cones are at much lower cost with similar performance to Winston Cones.

is reduced ~50% at 1.5°.

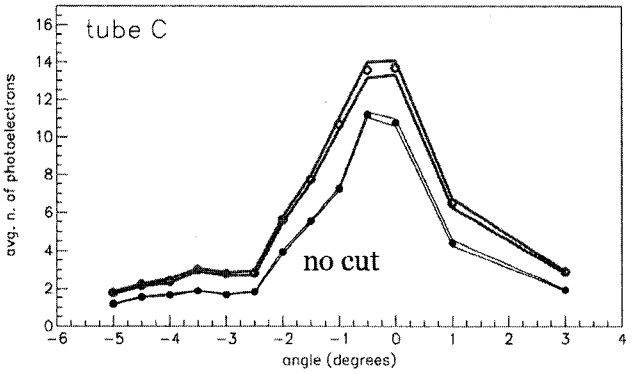

Figure 6.20: *Angle test of a fibre readout detector with (upper curve) and without (lower curve) the silicon strip selection.*

Pressure Test and Simulation

Fig. 6.21 shows the pressure test of the fibre readout detector with/without silicon strip selection. A comparison of test results in December 2006 test beam with simulation results is shown in Fig. 6.22.

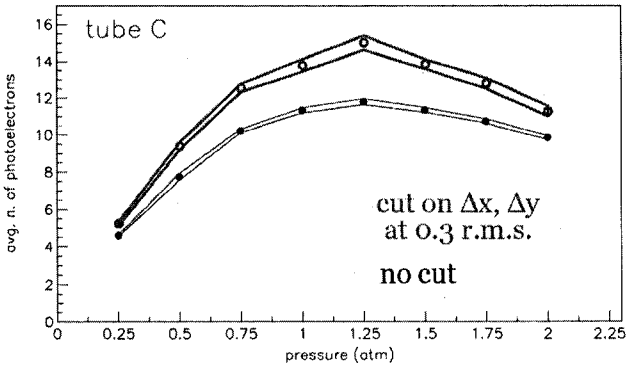

Figure 6.21: *Pressure Test of a fibre readout detector with (upper curve) and without (lower curve) the silicon strip selection.*

The discrepancy between test beam results and simulation results are mainly due to the following reasons:

1. The NA is not uniform over wavelength and information on the variation of NA with wavelength is not supplied by the manufacturer. In addition, the NA provided by the manufacturer includes light that is trapped in

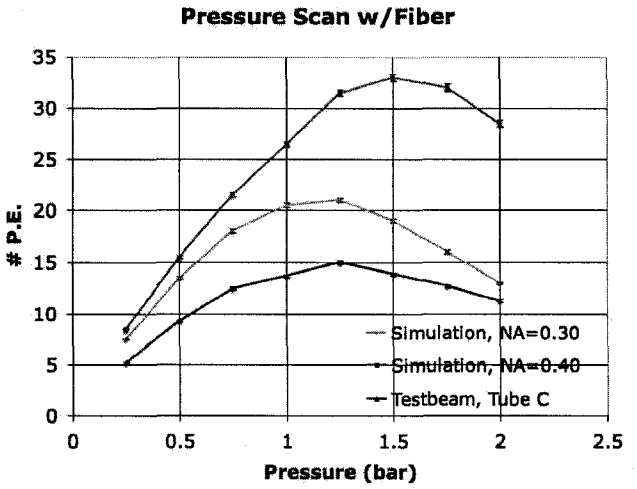

Figure 6.22: *Test beam result of the pressure test for a fibre readout detector, comparing with the simulation result when the numerical aperture of the fibre is set to 0.30 and 0.40.*

the cladding which has a short, wavelength dependent, and unspecified, attenuation length.

2. Efficiency of light acceptance by the fibres. Due to the limit of resolution of the pictures taken for fibre section, the relative positions of the fibres have limited accuracy. The fibres could be damaged during the process of bundling and coupling, which leads to reduced efficiency in transmitting light. This effect is also not included in the simulation.

3. The non-uniformity in the efficiency for light transfer to the MAPMT "Pixel". The MAPMT detection efficiency is not uniform over its surface. For this reason, the coupling of fibres to the MAPMT could affect the MAPMT readout. In the simulation, this effect is not modeled.

4. At a higher pressure, the Cerenkov angle is bigger (3° at 1 bar, while 5° at 2 bar), for this reason, photons at a higher pressure experience more reflections than those at a lower pressure. The slight imperfection in simulating the reflection is amplified. Also, at a higher pressure, because of the larger Cerenkov angle of the emitted light, the angle of the photons coming out of the exit of the light collector (Winston Cone) is much bigger than the lower pressure case. Because of the the angular

acceptance of the optical fibre due to numerical aperture, higher angle photons cannot enter one fibre.

These factors are not quantifiable at this stage so that they are not precisely reflected in the simulation curve.

6.5 Conclusion

The test beam experiments and test bench measurements provided an understanding of the performance of the LUCID detector and was key to the design of LUCID and the choice of the best operating conditions. The test beam results were well reproduced up to 1.3 bar by the Monte Carlo simulation of the PMT readout detector, enabling us to predict the performance of the Phase I LUCID design. The current simulation overestimates the light gathered by the fibre/light-collector readout detector. The baseline Phase II LUCID design, that relies on fibre/light-collector readout Cerenkov tubes, is currently being studied. The Phase I detector includes four fibre/light-collector readout Cerenkov tubes that provide a test platform for the baseline Phase II LUCID detector design.

Chapter 7

Performance of the LUCID Phase I

7.1 Introduction

In order to study the performance of the LUCID detector under the expected radiation environment in ATLAS, a GEANT4 [66] simulation of the LUCID Phase I detector was developed.

7.2 Setup and Procedure of Simulation

The simulation procedure can be divided into two parts. In the first part, the whole ATLAS detector is simulated using GEANT3 [67], with only the uninstrumented volume of the LUCID implemented[1]. The GEANT3 simulation of the ATLAS detector includes the beam pipe and the materials in front of the LUCID. The LUCID volume is placed $\sim \pm 17$ m away from the interaction point (See Fig. 5.1). Minimum-bias interactions generated by the PHOJET 1.12 [68] event generator are input to the GEANT3 simulation. The interaction of these particles with the ATLAS beam pipe and those parts of the detector that lie within their path as they travel towards the LUCID are modeled. The subsequent "hits" in the LUCID volume are recorded. The particles hitting the LUCID volume include not only the primary particles coming directly from

[1]This program is developed by Mike Shupe.

the interaction point, but also the secondary particles produced from the scattering of primaries in the beam pipe, other ATLAS materials, and particles scattered in from material surrounding ATLAS. The minimum-bias processes include non-diffractive elastic scattering, single diffractive dissociation, single diffractive dissociation, double diffractive dissociation, central diffraction (double-pomeron scattering) [69].

A distribution of the number of different types of particles generated in PHOJET at the interaction point is shown in Fig. 7.1. The primary particles are dominantly π^0 and $\pi^{\pm}$, their interaction with the beam pipe will produce secondary electrons, gammas, neutrons and protons due to hadronic and electromagnetic interactions.

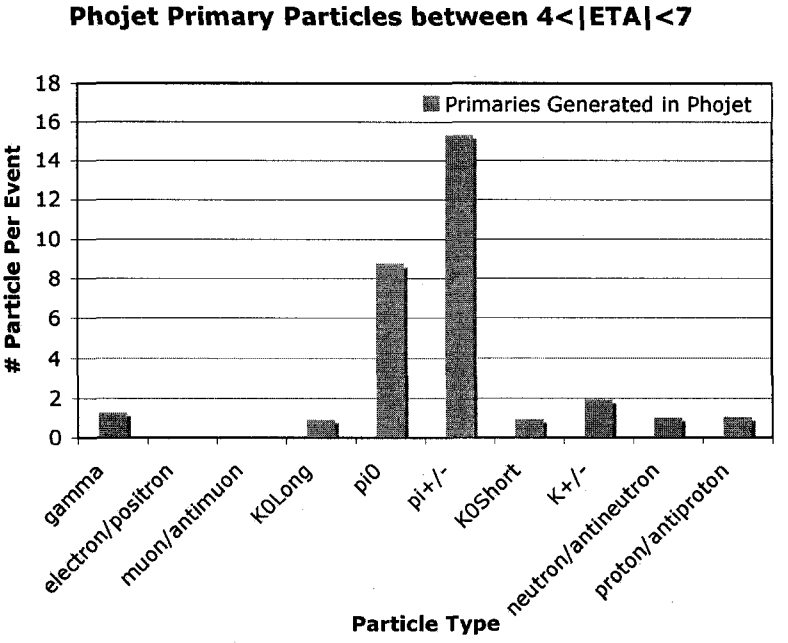

Figure 7.1: *Distribution of different types of particles generated in the PHOJET event generator within pseduo-rapidity range* $4 < |\eta| < 7$.

The shape of the LUCID volume is implemented in GEANT3 (not GEANT4) simulation can be seen in Fig. 7.2 (left). It is a cone shape volume with length $\sim$ 2 m, inner diameter 7.6 cm and outer diameter 16 (18) cm at near (far) end. The LUCID volume (in the first step) is slightly bigger than the complete LUCID detector fully implemented in GEANT4. The distributions of the hit position along the beam axis Z, and the hit position distance to the

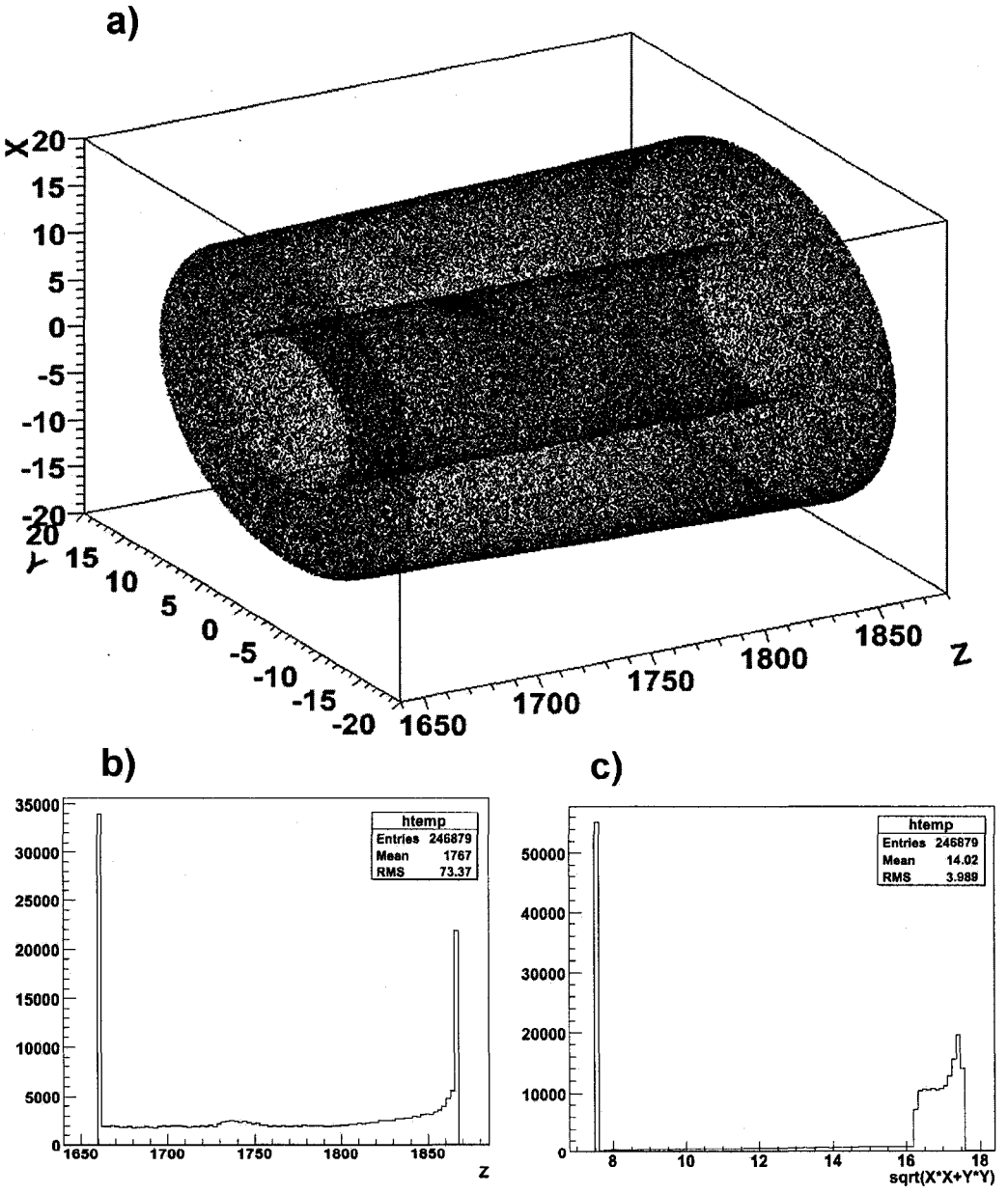

Figure 7.2: *Distributions of the hit positions of background. a) the scatter plot of the hit position of all particles; b) is the Z distribution; c) is the* $R = \sqrt{X^2 + Y^2}$ *distribution.*

beam axis R are shown. It is clear that there are particles coming from all directions hitting all around the LUCID volume.

In the second part of the simulation, using the hits on the LUCID volume collected in the first part of the simulation, a GEANT4 simulation of the detailed LUCID detector, including the gas vessel, Cerenkov tubes, cones and PMTs, is built inside the LUCID volume. For each interaction, the hits collected in the previous step are input into the detailed simulation.

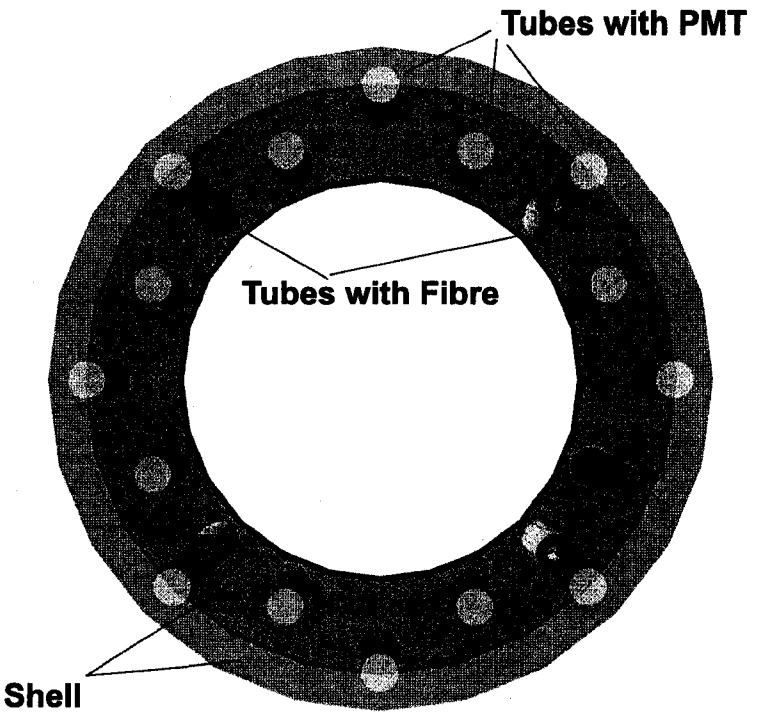

Figure 7.3: *Front view of one LUCID module in GEANT4 simulation, showing the Cerenkov tubes, PMTs, cones, and aluminum shell. fibre bundles are not shown.*

Fig. 7.3 and Fig. 7.4 show the setup of one module of the LUCID Phase I detector. It consists of 16 Cerenkov tubes read out by PMTs and four Cerenkov tubes read out by a remote MAPMT via a cone and a fused silica fibre bundle. The fibre readout detectors are very similar with those tested in the test beam experiment except that the diameter of the Cerenkov tube is slightly smaller (15 mm instead of 17 mm) and a straight light collector (10 cm long) is used, rather than a Winston Cone. The output diameter of the light collector is 6 mm. For the PMT readout detectors, 15 mm PMT sensitive area and 1 mm

Figure 7.4: *Prospective view of one LUCID module in the GEANT4 simulation. The readout structures are not shown.*

quartz PMT window is simulated.

The primary particles (pointing to the LUCID and potentially hit the LUCID) coming from the IP interact with the beam pipe and only a fraction of them reach the LUCID volume. This can be seen by comparing the blue (left) and red (middle) bars in each group in Fig. ??. A large number of secondary particles hit the LUCID volume in each interaction. The neutral particles like gammas and neutrons may interact in the LUCID material and their charged secondaries could generate light in the Cerenkov tubes. The charged particles like electrons and pions will generate light both directly in the Cerenkov tube and by scattering.

The timing characteristic of the particles is also very important for the analysis. As shown in Fig. 7.5, the first peak at $\sim$ 55.5 ns is due to the primaries and hard secondaries[2] coming along the direction from the IP and hit the front surface of LUCID. Particles hitting the side and back of the LUCID arrive at a later time. The second peak near 65ns is due to the particles hitting the back of LUCID volume, mainly backscattered particles from materials downstream.

[2]Secondary particles generated in the beam pipe by primaries that maintain the same time and direction. These secondaries travel the full tube length, giving a signal similar to a primary charged particle.

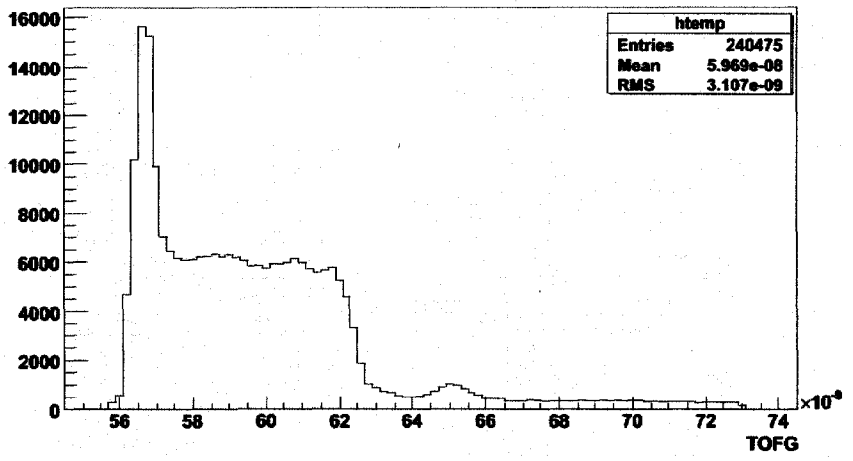

Figure 7.5: *Time of flight distribution of particles when hitting the LUCID volume. Primary and hard secondary particles contribute to the first peak, while the second peak near 65 ns is due to the particles hitting the back of the LUCID volume.*

7.3 Expected LUCID Phase I Performance

The data obtained from step one of the simulation consist of information for each minimum-bias interaction. To simulate different luminosity environments, different number of interactions are input to the GEANT4 simulation per beam crossing. For example, to simulate a low luminosity run at $10^{33}\,\mathrm{cm}^{-2}\mathrm{s}^{-1}$, data from 2 interactions[3] per beam crossing are input to the GEANT4 (Part 2) simulation each time; to simulate a high luminosity run at $10^{34}\,\mathrm{cm}^{-2}\mathrm{s}^{-1}$, data from $\sim$ 20 interactions are input into the GEANT4 (Part 2) simulation per beam crossing. These interaction data are randomly selected from a "pool" of $\sim$ 5000 events. A luminosity range of average 0.1 interactions per event to on average of 10 interactions per event are simulated in the LUCID Phase I simulation, corresponding to a luminosity range $\sim 5 \times 10^{31}\,\mathrm{cm}^{-2}\mathrm{s}^{-1}$ to $\sim 5 \times 10^{33}\,\mathrm{cm}^{-2}\mathrm{s}^{-1}$.

7.3.1 Photo-electrons Generated in the PMT

At a luminosity of 1 interaction per event (on average), the signal pulse size (number of photo-electrons) distribution is shown in Fig. 7.6 (left). The

[3]A random number generator generates the number of interactions at each event with a Poisson distribution of mean 2.

simulation includes: 1) the effect of both primary and secondary particles; 2) the generation of Cerenkov photons, tracing the photons to the PMT; 3) the quantum efficiency of the PMT.

The smaller peak P1 around 25 P.E. is due to the light generated by a charged particle crossing the PMT window. This value is consistent with the theoretical prediction and the test beam results (note that 50 P.E. is detected in the test beam experiment since the PMT window is twice as thick). The bigger peak P2 around 75 P.E. is due to those primary and secondary charged particle that travel down the Cerenkov tube and cross the PMT window. From this we know the signal caused by the gas tube is ~50 P.E., which is consistent with the test beam result (Chapter 7).

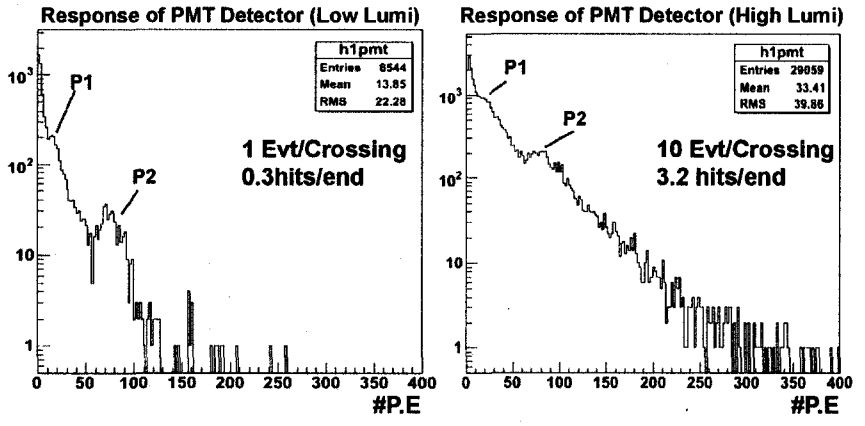

Figure 7.6: *The response of PMT readout detectors at low (left) and medium-high (right) luminosity.*

At a higher luminosity of 10 interactions per event, the corresponding distribution is shown in Fig. 7.6 (right). The two peaks from the PMT window and Cerenkov tube are still clearly visible in the plot, however, due to the increased amount of background, the tail for higher luminosity case is much bigger than the one at lower luminosity.

7.3.2 Estimate of the Number of Photo-electrons Generated in the MAPMT

The signal size (P.E.) distributions are shown in Fig. 7.7 under the same luminosity conditions considered for the PMT readout Cerenkov tubes. The

peak is at ~20 P.E. The signal amplitude is much smaller in the fibre readout detector than the PMT readout detector because of the light loss in the optical system (light collector and optical fiber). However, the advantage of the fibre readout detector is the reduced background from primary and secondary particles. The peak is very clear at a relatively high luminosity, and it is easier to determine the threshold, because 1) the fibre readout detectors has no PMT window; 2) the light collector and fibre bundle helps to reduced noise from non-pointing particles[4]. Also, Cerenkov light produced in the fibres is highly attenuated in the fibre.

Considering the acceptance area of 4 fibre readout detectors and 16 PMT readout detectors, the number of hits, where a "hit" is defined in the next subsection, in the PMT readout detectors is ~4–5 times the number of hits in the fibre readout detectors. Comparing the acceptance area of the PMT readout detectors to that of the fibre readout detectors (16:4), this result is in reasonable agreement.

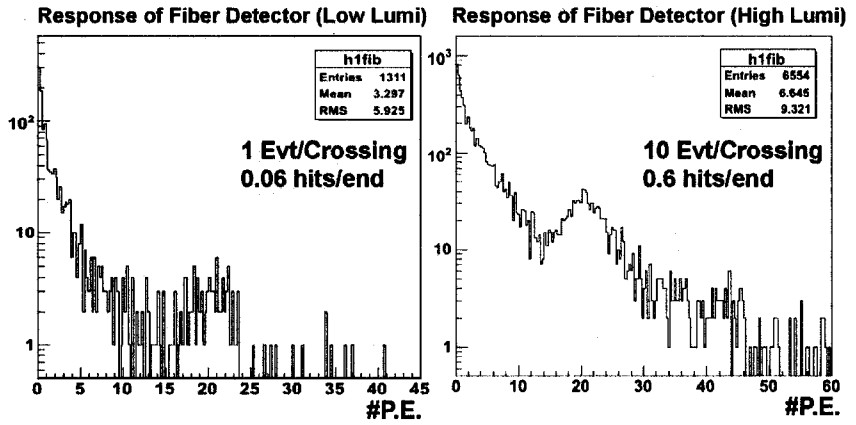

Figure 7.7: *The response of the fibre readout detectors at low (left) and high (right) luminosity.*

[4]The light collector and fibre bundle help reduce noise from non-pointing particles in two different scenarios: 1) light produced by the non-pointing secondary particles in the tube are suppressed since the photons cannot exit the light collector due to its larger angle; 2) due to the NA of the fibres, only light with incident angle smaller than ~ 20° can enter the fibre bundle, so the background (from light with large incidence angle) produced by non-pointing secondary particles is further reduced.

7.3.3 Definition of Hits

A hit in the LUCID Phase I detector is defined as follows. In each beam crossing of the LUCID run, for a certain Cerenkov Tube (there are 20 of them at each end), if the signal (#P.E.) is larger than the preset threshold value, we say that there is one hit in that Cerenkov Tube. This definition is the same for both PMT and fibre readout detectors.

From this definition, there can be at most 20 hits per end and at least 0 hits per end. In the LUCID Phase I, the instantaneous luminosity is directly proportional to the number of hits detected in each event[5].

Considering the simulation, by setting the threshold at 50 P.E. for a PMT readout detector, the number of hits per event is on average 0.3 per end at a luminosity corresponding to 1 interaction per event and on average 3.2 per end at a luminosity of 10 interactions per event. The threshold of the fibre readout detector is chosen to be 13 P.E. With this threshold, there are on average 0.06 hits per end per event at low luminosity (1 interaction per event) and on average 0.6 hits per end per event at medium high luminosity (10 interactions per event).

7.3.4 Determination of Threshold at Higher Luminosity

At higher luminosity, the background in the PMT readout detectors blur out the signal peak and make the determination of threshold more difficult. Although the threshold can be determined at lower luminosity, it is still useful to check the consistency of the threshold at higher luminosity. To solve this problem, the neighbour technique can be used.

Out of the 16 PMT readout detectors at each end, there are four of them which are adjacent to a fibre readout detector. A detected primary or hard secondary particle will traverse the full length of a Cerenkov tube. However, a background particle that traverses the tube at an angle will sometimes cross a neighboring tube as well. By requiring that the adjacent fibre readout detectors have no (or very small) signal, the background in the PMT readout

[5]Under the LUCID Phase I situation, the probability of multiple tracks in the same tube during one event is very low, so multiple tracks in the same tube are considered at most one hit. This only applies to the LUCID Phase I.

detector can be effectively reduced, making it easier to determine the threshold.

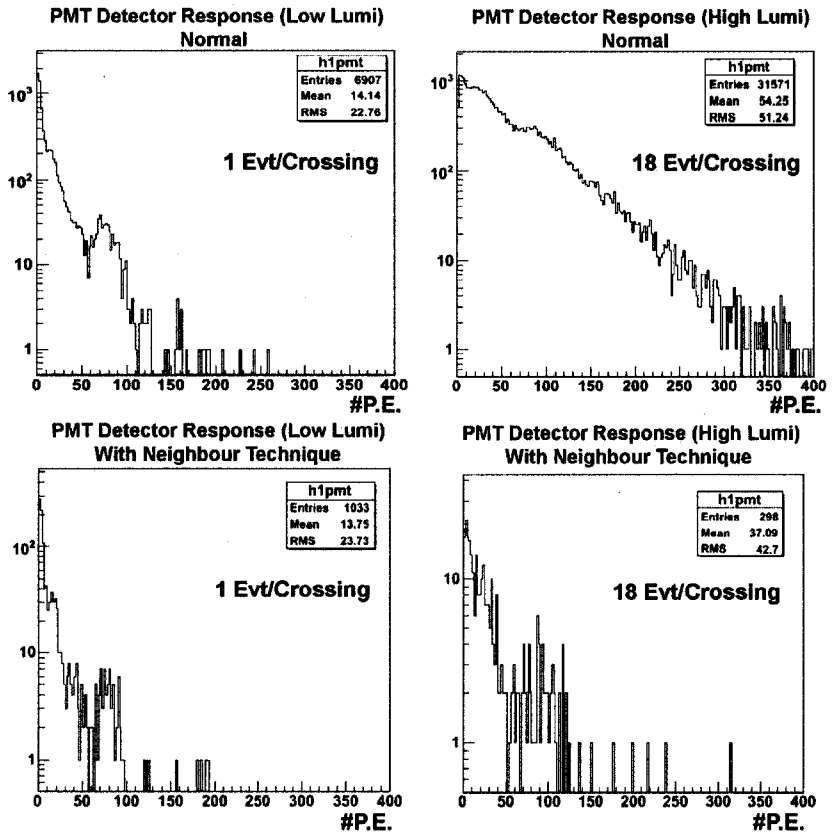

Figure 7.8: *The signal size distribution before (top) and after (bottom) applying the neighbour technique at low (left) and high (right) luminosity.*

Fig. 7.8 shows the signal size distribution before and after requiring that the PMT readout detector's adjacent fibre readout detectors have no more than a 0.1 P.E signal detected. The peak position is not changed after applying the neighbour technique and the threshold is much easier to determine.

7.3.5 Detection Efficiency of LUCID

Fig. 7.9 shows the detection efficiency for the LUCID Phase I from low to high luminosity. In reading this graph please note that $E_{AnyEnd} = E_{BothEnd} + E_{OneEndOnly}$. Where E_{AnyEnd} is the efficiency when there is at least 1 hit in at least one module of the LUCID; $E_{BothEnd}$, there is at least 1 hit in both

LUCID modules; $E_{OneEndOnly}$, there is one and only one LUCID module that has at least 1 hit; E_{NoEnd}, there is no hit in any LUCID module. This graph clearly shows that the method of luminosity determination by zero counting becomes extremely inefficient at high luminosity although it is still useful below around $2 \times 10^{32}\,\mathrm{cm}^{-2}\mathrm{s}^{-1}$. It also shows that the method of hit counting at 10 interactions per event ($\sim 10^{33}\,\mathrm{cm}^{-2}\mathrm{s}^{-1}$) will utilize over 90% of the beam crossings. Even at $\sim 10^{33}\,\mathrm{cm}^{-2}\mathrm{s}^{-1}$ the hit counting method will utilize ~20% of the beam crossings.

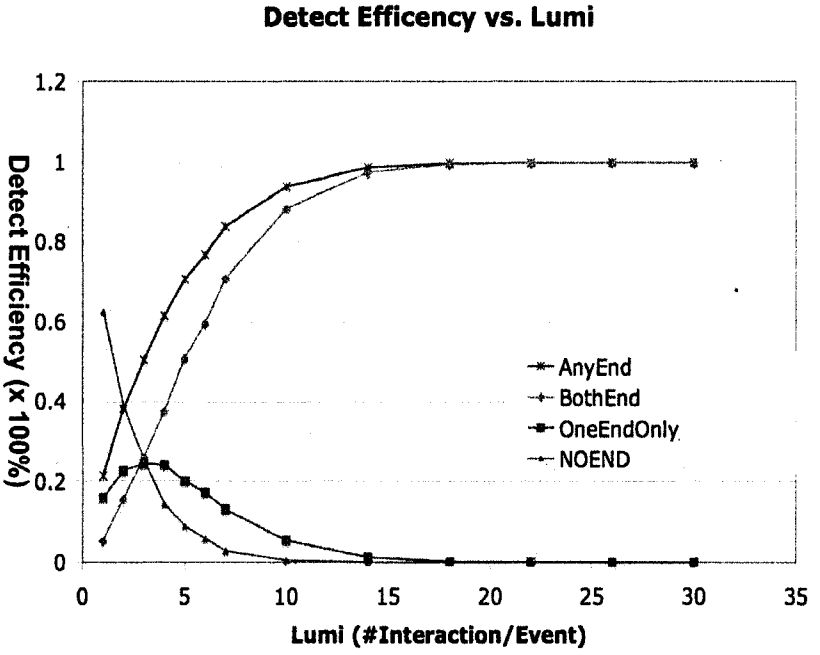

Figure 7.9: *Detection efficiency of the LUCID Phase I. E_{AnyEnd} there is at least 1 hit in at least one module of LUCID; $E_{BothEnd}$ there is at least 1 hit in both LUCID modules; $E_{OneEndOnly}$ there is one and only one LUCID module that has at least 1 hit; E_{NoEnd} there is no hit in any LUCID module.*

7.3.6 Linear Response of the LUCID

There is a linear relationship between the luminosity and the LUCID response (number of hits in the LUCID). Fig. 7.10 shows the relationship between luminosity and number of hits in the LUCID Phase I (both ends, PMT readout detectors only). There are on average 0.6 hits per interaction, with 0.1 hits contributed by the primary particles and the rest of them contributed by

the hard secondary particles. These higher energy secondary particles are produced in the scattering of primaries with the beam pipe and maintain a similar direction and timing characteristic to the primary particle. The LUCID usually cannot distinguish hard secondaries from primaries because they produce similar amounts of light in the Cerenkov tube.

The LUCID Phase I works under a condition of less than ~10 interactions per event (beam crossing). There are on average <3 hits at 5 interactions per event. From the simulation, we estimate the probability of more than one track in the same tube to be ~1% at 5 interactions per event and ~13% at 20 interactions per event. The ability to identify multiple tracks in one detector is more important in Phase II than in Phase I due to a higher luminosity.

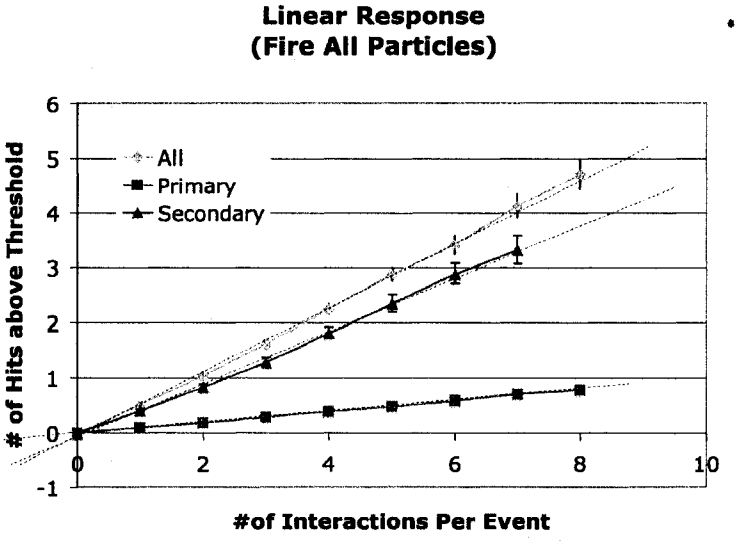

Figure 7.10: *Linear relationship between luminosity and the LUCID Phase I response.*

7.4 Systematic Error Analysis

The main experimental systematic errors in the luminosity measurement arise from two sources: the detector itself and the LHC beam. A list of systematics potentially includes contributions from: beam optics, beam position, gas pressure stability, PMT gain stability, gas contamination and temperature stability. The estimation of these errors is the subject of this subsection.

The systematic errors affect the slope of the linear increase of "hits" with luminosity in the following way. After calibration, the linear relation between luminosity and the number of hits in the LUCID can be written as $N = k_0 L$. For each observed N, the luminosity can be determined from $L = N/k_0$. When the condition changes, assuming the linear relation between N and L is maintained, the real relation between N and L should be $N = k_1 L$, as shown in Fig. 7.11. If in this case, the original relation $N = k_0 L$ is used in the luminosity calculation, measurement error is introduced.

Assume in a specific event under a changed condition, the measured number of hits in the LUCID is N_0, the calculated luminosity is $L_0 = N_0/k_0$. However, the real luminosity is $L_1 = N_0/k_1$. The percentage error between the measured luminosity and real luminosity is

$$\frac{\Delta L}{L_1} = \frac{L_0 - L_1}{L_1} = \frac{N_0/k_0 - N_0/k_1}{N_0/k_1} = \frac{k_1}{k_0} - 1, \tag{7.1}$$

where k_0 is the slope measured from the calibration and k_1 is the real slope under the new condition.

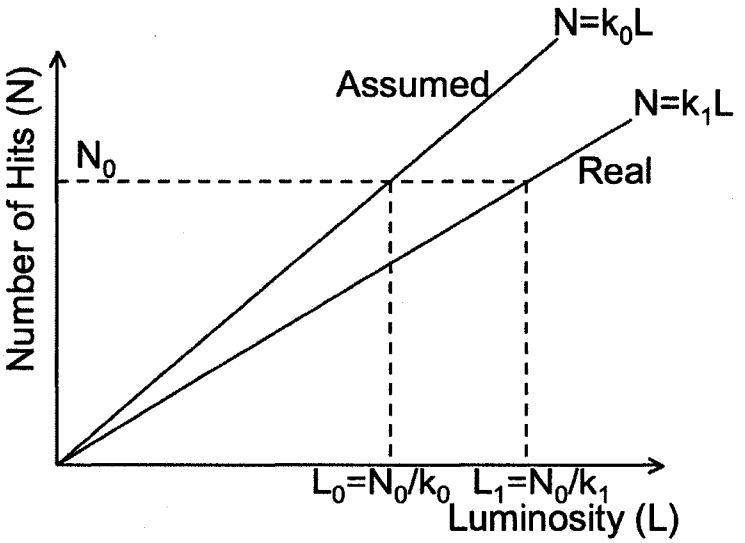

Figure 7.11: *Calculation of luminosity measurement error.*

7.4.1 Beam Optics

The LUCID will be calibrated using the ALFA detectors deployed in Roman Pots around the beam line at 240 m from the ATLAS IP. The ALFA Roman Pot data will be taken under special beam conditions within the special high β, low luminosity ($10^{27}\,\mathrm{cm}^{-2}\mathrm{s}^{-1}$), run scheduled for $\sim$ 2010. The β difference between the calibration beam and the normal running beam of the LUCID is reflected on the beam size in both transverse planes and the beam divergence. A table of beam size and beam divergence in each beam condition is shown in Table.7.1.

	β (m)	Sigma Beam Size (μm)	Beam Divergence (μrad)
Normal Beam	0.5	16	32
Calibration Beam	2600	606	0.23

Table 7.1: *List of beam parameters for normal and calibration beam conditions. Sigma beam size is the width of the Gaussian distribution of the beam size. Beam divergence is the width of the Gaussian distribution of the angle between a beam particle and the beam axis.*

The systematic error introduced by beam optics is estimated in Appendix A. The estimation is based on the fact that the number of hits N and pseudorapidity η have a close to linear relation. When a small change in beam divergence angle is induced by changing β, a corresponding change in the number of hits in the LUCID can be calculated. The calculation shows that the systematic error introduced by the beam optics is below 1%.

7.4.2 Interaction Point Displacement Along the Beam Axis

The collision point of the two protons can have a displacement of several cm along the beam axis (Z direction) with respect to the interaction point. To study this effect, a simulation study combining the Phase I detector simulation and the PYTHIA [32] event generator is investigated. PYTHIA is used to generate minimum-bias events with a Z-displacement of the collision point for each event. The value of the Z-displacement is picked randomly from a

Gaussian distribution with mean value 0 and σ_D = 0 cm, 5 cm, and 10 cm. With the threshold of 50 P.E., the linear relation between number of hits per end and luminosity is shown in Fig. 7.12 for each σ_D. The slopes for σ_D = 0, 5, 10 cm are all $k = 0.34$. The luminosity measurement error $\Delta L/L_1$ is not detectable. The result shows the systematic error introduced by the IP displacement over the expected range is < 0.5% [6].

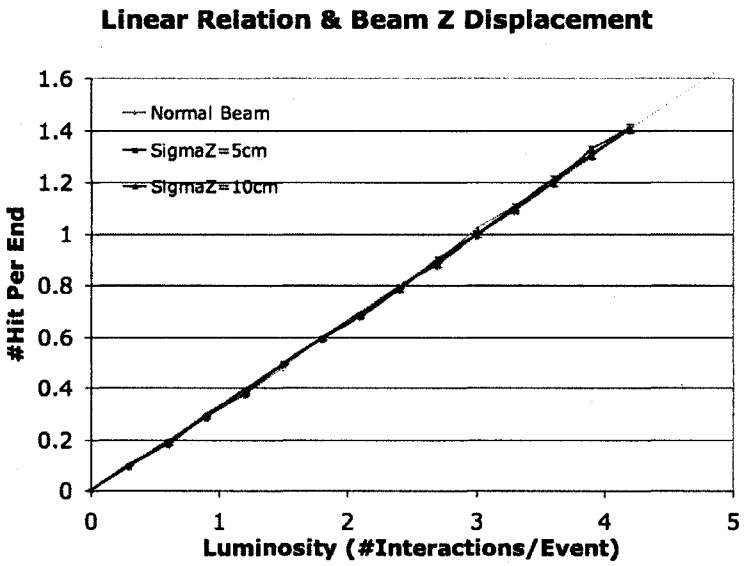

Figure 7.12: *Linear relationship of the LUCID Phase I for different Z-displacement of the IP. The sigma z-displacement of IP along the beam axis σ_D = 0 cm, 5 cm and 10 cm are shown.*

7.4.3 Gas Pressure

The absolute pressure of the LUCID is set to 1.3 bar, 0.3 bar over atmospheric pressure, and is monitored to $\sim \pm 10$ mbar. A simulation study is performed by adjusting the working pressure to (1.30 ± 0.01) bar. This pressure change results in a 0.02° change in the Cerenkov angle $(4.02 \pm 0.02)°$. Fig. 7.13 shows the linear relationship for this study. The slope is changed by ~0.4%. So the systematic error introduced by pressure variance is <0.4%.

[6]The 0.5% is due to the statistical error of this study.

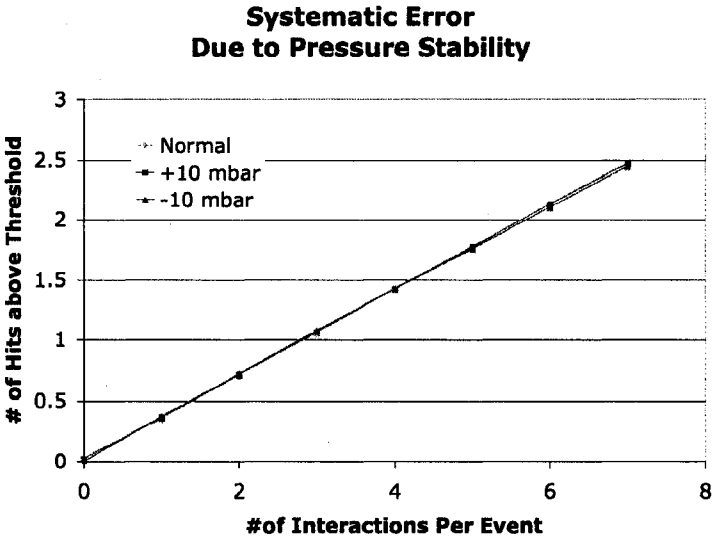

Figure 7.13: *Change of linear relationship when the gas pressure varies for 10 mbar. This plot has a different number of hits per event from Fig. 7.10 because this study utilizes PYTHIA event generator to generate min-bias events and pass these events to the LUCID simulation, while Fig. 7.10 is obtained from the two-part procedure described earlier in this chapter.*

7.4.4 Temperature Variance

The LUCID is working under room temperature, a worst case temperature variance of 5°C to 35°C is assumed, which corresponds to ±5%.

According to Eq. 6.1, the refractive index of C_4F_{10} calculated. Fig. 7.14 shows the relation between number of hits in LUCID and luminosity for normal condition and ±5%temperature change. The slope for the normal condition line is k_0 =0.332 [7], and k_{-5} =0.324, k_{+5} =0.340. Which corresponds to the luminosity measurement error of ~2.5%.

7.4.5 Gas Contamination

The water vapor or O_2 impurities can significantly increase the absorption of light (especially UV light), which reduce the number of hit of the LUCID. To address this point, a filter system is included in the LUCID gas system,

[7]It's different from the k_0 in IP z-displacement curve because this one utilizes the two part normal study procedure described earlier in this Chapter, while the IP z-displacement curves are obtained with PYTHIA+Phase I simulation.

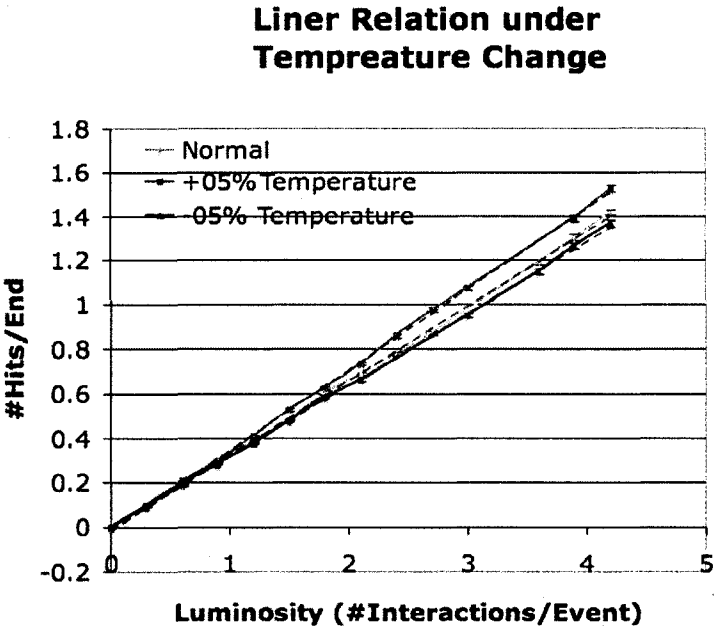

Figure 7.14: *Linear relationship of LUCID Phase I normal condition and ±5% temperature change.*

which reduce the impurities to a safe level (<0.01%), so that its effect on the luminosity measurement is negligible.

7.4.6 LUCID Alignment

The LUCID Phase I detector is expected to align with the beam pipe with a 0.1° accuracy. A simulation study is performed by rotating the LUCID for 0.1° with respect to the centre point of each module. The result shows that the effect on the slope of the linear relation is not detectable. So the systematic error introduced by the LUCID mis-alignment is negligible.

7.4.7 PMT Gain Stability

The gain of the PMT can be monitored by the build-in LED calibration system to an accuracy of ±5%. The change of the PMT's gain results in the error in setting the threshold. A ±5% change in gain corresponds to a ±5% change in the threshold. Fig. 7.15 shows the linear relationship when the threshold varies ±5%. This study is done by applying different thresholds to the upper

most curve in Fig. 7.10. The systematic error is estimated to be ~2.6%.

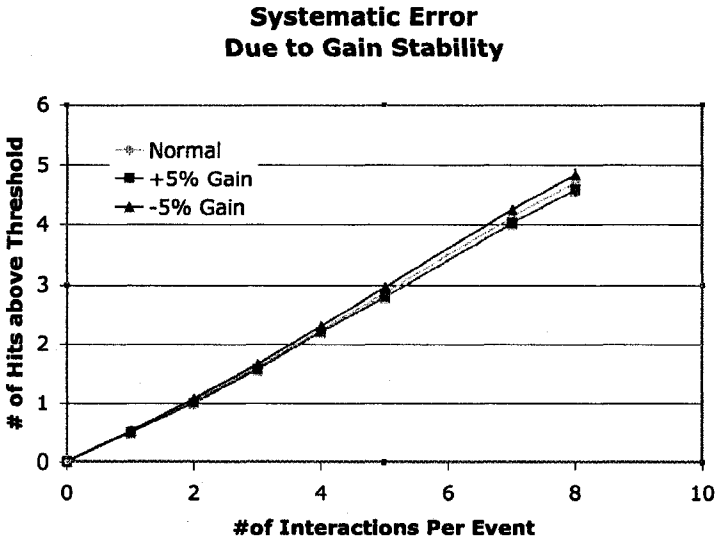

Figure 7.15: *Change of linear relationship when the gain of the PMT varies by ±5%.*

7.5 Conclusion

The background study gives us an estimate of the performance of the LUCID under the real ATLAS environment. For Phase I, it shows a linear relationship between the LUCID response and the real luminosity, which is a important factor for the LUCID to provide an accurate luminosity measurement. The overall systematic error is estimated to be <2.9%. Table 7.2 shows a summary of the systematic errors and their significance. Since the probability of multiple tracks in the same tube is small at phase I conditions (<1%), the systematic error introduced by this effect is neglected in the Phase I study.

Beam Optics	<1%
Beam Position	<0.5%
Gas Pressure Stability	<0.4%
Temperature Variance	<2.5%
Gas Contamination	negligible
PMT Gain Stability	<2.6%
LUCID Alignment	negligible
Multiple Tracks in One Tube	negligible in Phase I
Total (Added Quadratically) :	<3.8%

Table 7.2: *List of Systematic errors and significance for the LUCID Phase I.*

Chapter 8

FP420 Detector

8.1 Introduction

The FP420 project is presently in its R&D phase. It aims to deploy precision silicon detectors to measure the deflection of protons from peripheral collisions. The detectors are installed in the available space near ±420 m from the interaction point of the ATLAS & CMS experiment (ATLAS case is shown in Fig. 8.1). The LHC magnets between the ATLAS and CMS interaction points and the 420 m region deflect protons, that have lost only a small fraction of their initial momentum, out of the beam envelope. FP420 is designed to detect the protons that lose less than 1% of their longitudinal momentum in the interaction. By detecting these protons, a rich QCD, electroweak, Higgs and "beyond the Standard Model" (BSM) physics program becomes accessible.

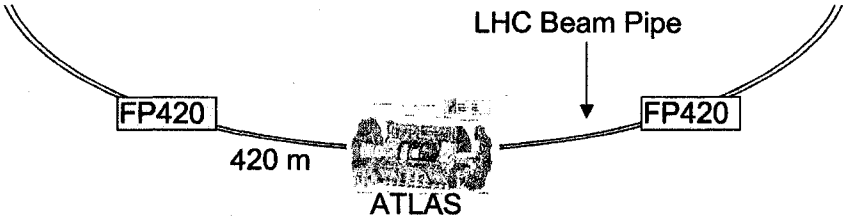

Figure 8.1: *Position of the FP420 detectors relative to the ATLAS detector. The sketch is not to scale.*

There are 15 m drift spaces around 420 m from the ATLAS and CMS interaction points. Protons that lose between 10^{-3} and 10^{-2} of their initial

momenta emerge from the beams in these regions, where the FP420 detectors are proposed to be installed. FP420 utilizes Roman Pots or Hamburg Pipes[1] to put the "edgeless" silicon detectors into a position which is very close to the beam line. The time of flight of the proton to the FP420 detectors is measured using Gas Cerenkov and Fused Silica Radiator Cerenkov detectors.

8.2 Physics at FP420

The forward physics program - including QCD, deflective and two photon physics topics - requires good acceptance for relatively low central masses across the luminosity range of ATLAS. However, ATLAS or CMS with proposed 220 m detectors [7] have no acceptance for central systems below 200 GeV . The FP420 detectors [8] cover the region of fractional proton momentum loss[2] $0.002 < \xi < 0.02$, giving access to central systems in the mass range 30 GeV/c^2 $< M <$ 200 GeV/c^2. With the FP420 detectors, the reach of the ATLAS and CMS detectors is significantly extended.

With the additional acceptance of FP420, the acceptance of the current detectors (ATLAS/CMS and 220 m) to $\xi = 0.002$ for nominal LHC luminosity optics is increased by an order of magnitude. Access to such low ξ is significantly better than that achievable at the Tevatron, and overlaps with the HERA diffractive DIS (deep inelastic scattering) range. This acceptance will allow precise, high statistics studies, for example the gluon content of proton at low-x and gap survival probabilities, which will in turn provide valuable insight into the contribution of multi-parton interactions to the underlying event. With LHC, it is also possible to study the diffractive structure functions of protons at conditions of low β and high Q^2 that HERA cannot reach.

Besides double diffractive interactions, the probing of single diffractive production of W, Z and γ allows the study of the diffractive structure functions under different kinematic regions.

The process $pp \rightarrow p + \gamma\gamma + p$ is an important "standard candle" for exclusive theoretical predictions at the LHC because it does not suffer from

[1]Hamburg Pipes are described in the later sections of this chapter.

[2]$\xi = \frac{\Delta P_L}{P_L}$, where P_L is the longitudinal momentum of the proton and ΔP_L is the loss of longitudinal momentum.

non-perterbative QCD calculation uncertainties and is a non-hadronic final state. Indeed, evidence for this channel has been seen at the Tevatron [70]. The cross-section for this process is 30 (6) fb for photon E_T values larger than 10 (15) GeV. Where both photons are in the central region $|\eta| < 2$.

At higher luminosity ($\sim$ 100 fb), FP420 allows us to study physics "beyond the Standard Model", for example, exotic bound states such as gluinoballs, direct observation of CP violation in some SUSY Higgs scenarios, etc. [7].

8.3 Acceptance, Resolution and Calibration

The acceptance for events where both protons are detected at 420m is shown in Fig. 8.2 (left). The acceptance is governed primarily by the dispersion of the LHC beam at 420 m and the distance of the FP420 silicon detectors from the beam. For a 120 GeV central state, with the detector 3 mm away from the beam pipe, the acceptance is 28% with FP420 itself. With both 420 m and 220 m detectors, the acceptance for higher central state masses can be increased. However, with only 220 m detectors themselves, the acceptance is very poor for low mass central states.

The mass resolution of the central system is dominated by the beam momentum spread of $\sigma_0 = 0.77$ GeV. The mass resolution on the central system of FP420 as a function of the mass of the standard model Higgs boson is shown in Fig. 8.2 (right), for 420 m - 420 m and 420 m - 220 m proton tags. The achievable resolution is better than 1.5 GeV if both protons are detected at 420m. If one proton is detected at 220 m, the resolution is at best $\sim$ 3 GeV for a 120 GeV central system at ATLAS, and at best $\sim$ 3.5 GeV at CMS.

The most reliable and accurate way to calibrate forward proton detectors is to find a high-rate, well understood process, which produces protons of known outgoing momentum determined from a measurement made using the central detectors alone. The $\gamma\gamma \to \mu\mu$ process is one candidate for this purpose and the detailed study of it, used to calibrate the FP420 detectors, is presented in the Chapter 10.

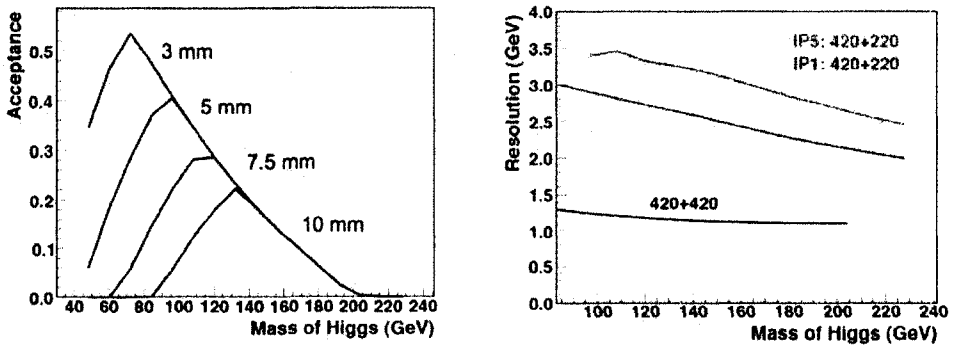

Figure 8.2: *The acceptance as a function of Higgs boson mass for the detection of both protons at 420 m at varying distances from the beam (left). The right hand plot shows the mass resolution as a function of Higgs boson mass for the case where both protons are detected at 420 m (lowest line), one proton is detected at 420 m and one at 220 m at ATLAS (IP1) (middle line) or CMS (IP5) (top line).*

8.4 Backgrounds

There are mainly 3 types of machine induced background processes at the LHC interaction regions:

- Inelastic beam-gas interactions - the interaction of incoming proton and residual gas in the beam pipe.
- Elastic beam-gas interactions - elastic, single diffractive and central diffractive proton-nucleus collisions, producing leading small angle protons.
- Cleaning inefficiency - proton out-scattering from the collimators followed by a lack of absorption in the collimators or in other elements of the beam cleaning system.

Process 2 and 3 are major components of the beam halo background, which is hard to calculate reliably prior to LHC running. Preliminary results for IP5 (CMS) indicate that at full luminosity the rate of halo protons after cleaning is 1 kHz.

For physics backgrounds, the major contribution arises from pile-up events. The low cross section (fb level) of new physics processes in the central exclusive channel requires FP420 to run in a high luminosity environment $L \sim 10^{33} - 10^{34}\,\mathrm{cm}^{-2}\mathrm{s}^{-1}$, where tens of interactions take place at each crossing. Three kind of pile-up backgrounds need to be considered at these luminosities, as

shown in Fig. 8.3, they are: a) protons from two single diffractive events are super-imposed with a central hard scatter; b) protons from one double diffractive events are super-imposed with a central hard scatter; c) a proton from one single diffractive event is super-imposed with a central hard scatter that has a proton as a product.

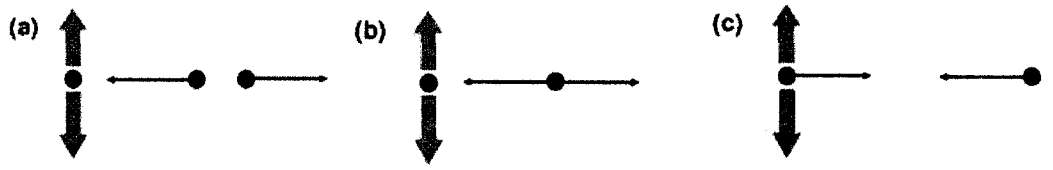

Figure 8.3: *A schematic diagram of pile-up backgrounds to central exclusive production: (a) three interactions, one with a central system, and two with opposite direction single diffractive protons (b) two interactions, one with a central system, and the second with two opposite direction protons (c) two interactions, one with a central system and a proton, the second with a proton in the opposite direction.*

One method to reduce these backgrounds is by high precision timing measurements of the protons [71]. Only the relative arrival time, $\Delta t = t_L - t_R$ needs to be measured, where t_L and t_R are the time of arrival of the proton at either side of IP. If the two protons come from the same event, after calibration we have the z-position of that event as $z_{pp} = \frac{1}{2}\Delta t \times c$. The uncertainty on z_{pp} is $z_{pp} = \frac{c}{\sqrt{2}}\delta t$, where δt is the (r.m.s.) time resolution of the proton measurement. For example, if the time resolution is 10 ps, the spacial resolution will be 2.1 mm. Since the vertex position v_{vertex} of the same event is measured with good precision (~ 50 μm) [45], by matching z_{pp} with v_{vertex}, the pile-up background can be effectively reduced.

8.5 Proton Tagging Detectors in FP420

8.5.1 Modifications to the 420 m Region

In the LHC design, at 420 m there is a 15 m-long "interconnection cryostat" that connects the super-conducting arcs of the accelerator with the warmer interaction regions. The cryostat provides continuity not only of the beams, but also of the insulation vacuum, cryogenic circuits, and thermal and radiation shielding of the accelerator. By redesigning this interconnection cryostat,

extra tracking detectors can be installed without affecting the functionality of the cryostat.

8.5.2 Positioning the Detectors

The FP420 detectors need to be placed near to the beam (several mm). However, during beam injection, due to radiation problems, the FP420 detectors have to be kept out of the standard beam-pipe aperture. So there has to be a mechanism that can move the detector without breaking the continuity of the beam line. Roman Pot detector units were considered a possible solution however the available space near the 420 m area is very limited and bulky Roman Pot units are not suitable for this purpose.

Another possible solution for the movement mechanism under study is the so-called "Hamburg Pipe". It is based on the existing technology used at HERA at DESY (Deutsches Elektronen-Synchrotron). The entire length of the FP420 beam pipe is movable, and connected by bellows at each end to the standard pipe. As shown in Fig. 8.4, there will be three or four pockets installed in the Hamburg Pipe. In the pockets, the silicon detectors, timing detectors and beam position monitors (BPM) are fixed to the pipe in an "optical bench" arrangement, allowing internal alignment to better than 1 micron.

8.5.3 Silicon Detector

The choice of tracking detector is 3D edgeless silicon. It is a new generation of semiconductor devices where, by using micro-matching techniques, electrodes penetrate the entire thickness of the detector perpendicular to the surface [72, 73, 74]. By doing this, smaller collection distances, very fast signals and substantially improved radiation tolerance can be achieved[3]. A drawing of 3D silicon detector compared to regular planar detector is shown in Fig. 8.5.

The response of 3D detectors has been measured and is reported in detail elsewhere [7]. The detector is sensitive within 10 μm of its physical edge.

[3]The collision experiments nowadays are at higher luminosity and demand higher precision in position measurement, the improved radiation tolerance, fast signal, and precision will be very useful.

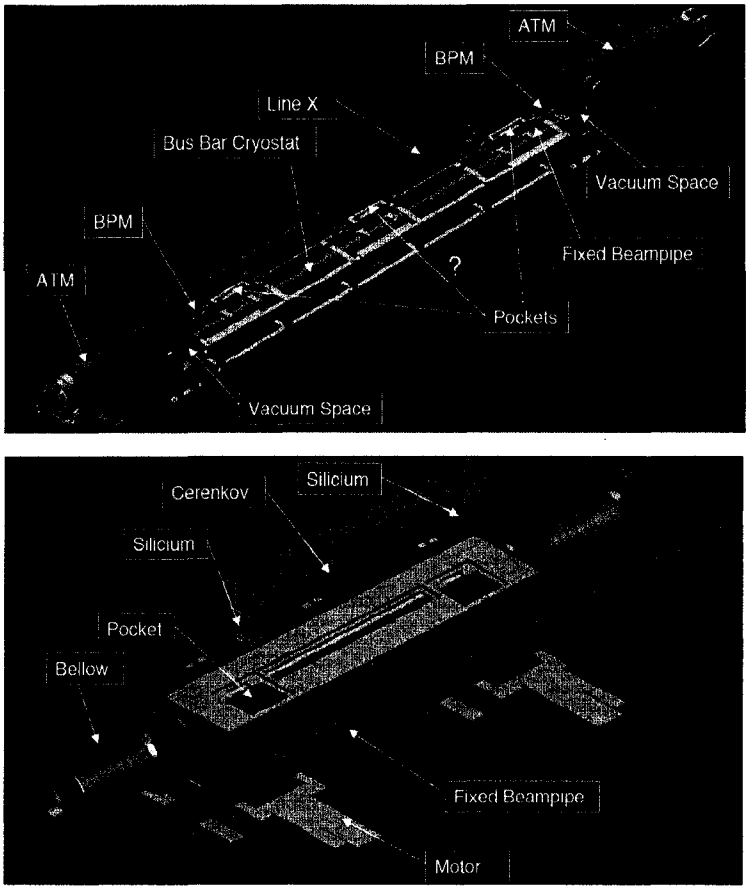

Figure 8.4: *Artistic drawing of the FP420 cryostat (top) and the Hamburg Pipe moving mechanism (bottom).*

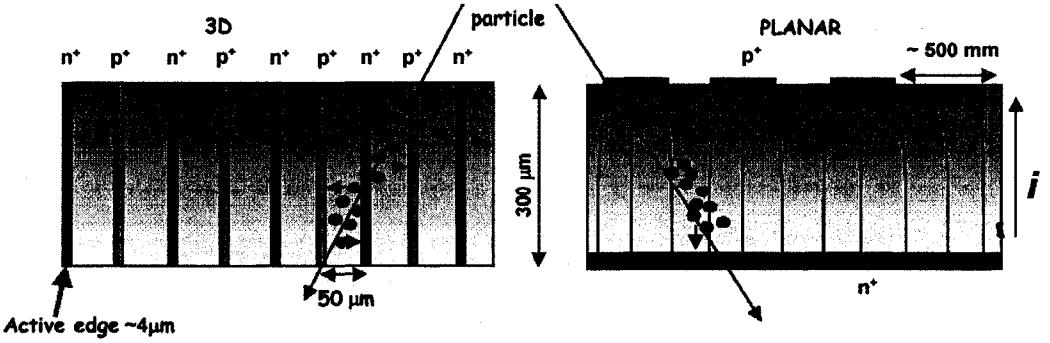

Figure 8.5: *Comparing a pure 3D detector with a regular planar detector. In the 3D detector the p^+ and n^+ electrodes are processed inside the silicon bulk.*

8.5.4 Time of Flight Detectors

To determine the vertex position of the deflected protons, a very precise Time of Flight (ToF) detector is required. A timing resolution within 10ps will provide a vertex resolution of $\sim$ 2 mm. There are two kinds of ToF detectors under construction; a gas Cerenkov counter (GasTOF), and a smaller quartz Cerenkov counter (QUARTIC). QUARTIC is the detector studied in this thesis. These studies are reported in Chapter 9.

Chapter 9

QUARTIC - The Time of Flight Detector for FP420

9.1 Introduction

Background from "pile-up events" in the FP420 detectors (described in Chapter 8) can be effectively reduced by deploying a precise Time-of-Flight (ToF) detector to measure the ToF of the particles impinging on the FP420 silicon detectors. For a ToF resolution of ~10 ps a vertex position resolution of ~ 2.1 mm is in principle achievable. Background reduction is achieved by rejecting tracks not coming from the main event vertex. QUARTIC is a dedicated quartz Cerenkov counter that can measure the time of flight of the proton with the required precision. Fig. 9.1 (left) shows a sketch of the QUARTIC design.

9.2 Design of QUARTIC

The QUARTIC detector is shown in Fig. 9.1. It uses fused silica bars as radiators. QUARTIC consists of an array of fused silica bars arranged in a 4×8 matrix. Each bar is 5 mm in length with a 6 mm × 6 mm cross-section mounted at the Cerenkov angle of 50° to minimize the number of reflections when the light propagates through the polished aluminium light guide to the MCP-PMT (Micro Channel Plate PMT). An air light guide is used to avoid the

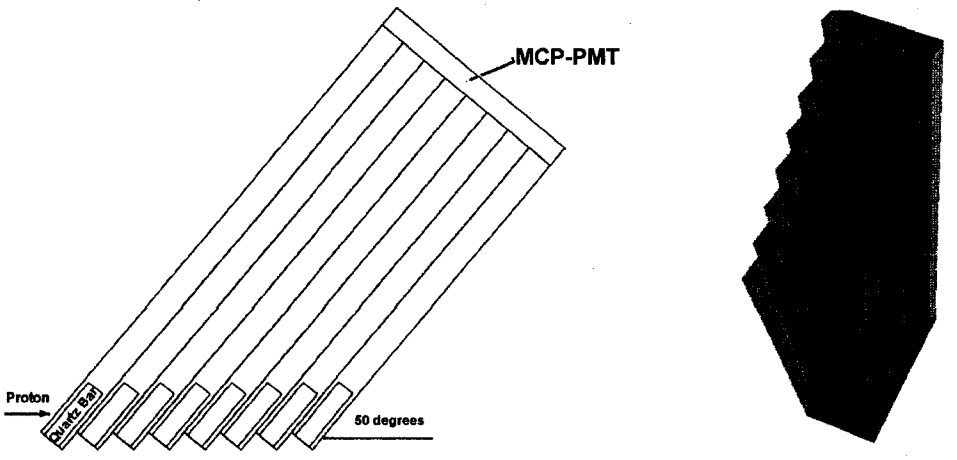

Figure 9.1: *A sketch of QUARTIC design (left) and an artistic drawing of QUARTIC (right). The sketch is not to scale.*

time dispersion from the wavelength dependence of the index of refraction of quartz. In the baseline design two QUARTIC detectors will be mounted after the FP420 silicon detectors system to avoid multiple scattering of particles in the relatively dense fused silica.

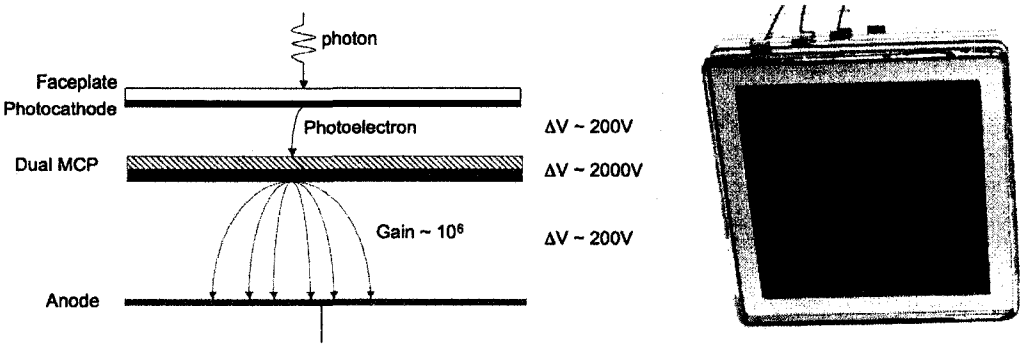

Figure 9.2: *A sketch of MCP-PMT design (left) and a picture of a MCP-PMT (right). The sketch is not to scale.*

The MCP-PMT is different from a conventional PMT in that it uses micro-channel plates to multiply the secondary electrons. A micro-channel plate consists of an array of millions of identical diameter glass capillaries with an internal diameter that can range from around 10 to 20 microns, fused into the form of a thin disk less than 1 mm thick. The channels are made of special glass doped with heavy metals that have the property that they will emit more

than one electron when hit by an electron. Each end of the walls is covered with a metal thin film which acts as an electrode and a high voltage (~2000 V) is applied between both ends of the capillary, as shown in Fig. 9.2. The initial photo-electron is multiplied by collisions with the walls of the glass vessels. Gains of 10^6 to 10^8 can be achieved. MCP-PMTs are fast devices and can provide a very good time resolution (as good as 10 ps).

This design of QUARTIC ensures the photons arrive at the PMT with the smallest dispersion in time. Due to the different transit times through the photo-detector, there is a $\sim$ 30 ps transit time spread. The smallest transit time jitter achieved with a commercial MAPMT is ~10 ps. As each channel is isolated from the others, it in principle measures the time independently. For each proton, multiple measurements reduce the error on the estimate of the ToF significantly. For example, if a proton ToF is measured by 16 isolated channels (for two QUARTIC detectors), the time estimate error is reduced by a factor of 4. Also since the proton we are interested in will traverse multiple channels, this multi-channel design can also be used to help to reduce the background particles coming from other directions.

9.3 Simulation Study of QUARTIC

To study the performance of QUARTIC, a simulation program was developed based on the GEANT4 simulation package. The simulation program models the detector shown in Fig. 9.1, with silica bars 15 mm long, bar width and height 6 mm, and the aluminum wall thickness 0.2 mm. The length of the shortest channel is 81.3 mm and the length of the longest channel is 113 mm.

The physics processes in the program include:

- *For the incoming proton*, the Cerenkov effect in silica, multiple scattering, ionization, elastic and inelastic hadronic interactions in dense media;
- *For photons*, production of Cerenkov photons, transportation, absorption, internal reflection, refraction, reflection on the aluminum surface, and the quantum efficiency of the PMT.

9.3.1 Simulation Parameters

The wavelength-dependent parameters in the simulation include the refractive index and absorption length of fused silica, reflectivity of the aluminum surface, and the quantum efficiency of the PMT.

The quantum efficiency, refractive index and absorption length of fused silica are provided by the manufacturer. Since the aluminum walls are polished bare aluminum, the reflectivity curve for LUCID polished tubes are used (see chapter 6). Fig. 9.3 shows these parameters with respect to photon wavelength. A range of 185 nm to 650 nm is considered in the simulation. The cutoff at 650 nm is due to MCP-PMT quantum efficiency. The cut-off at 185 nm is due to the absorption length of quartz bars. Out of range photons have a very small possibility to survive due to these cuts.

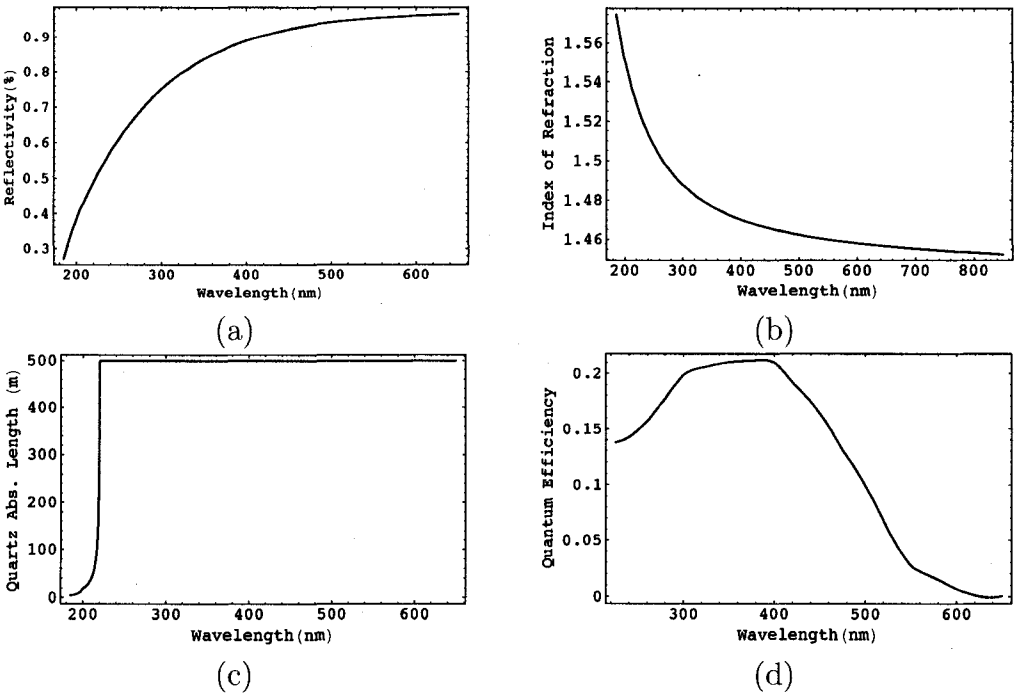

Figure 9.3: *Parameters used in the simulation of QUARTIC. a) reflectivity of aluminum surface; b) refractive index of the quartz bars; c) absorption length of the quartz bars; d) quantum efficiency of the MCP-PMT.*

9.3.2 Hit Positions of Photons on the MCP-PMT Face

Fig. 9.4(a) illustrates the response of the detector to a proton. This figure is produced by the visualization function of the simulation program. Due to the 50 degree angle of the QUARTIC detector with respect to the beam axis, a new coordinate system $(\vec{RX}, \vec{RY}, \vec{RZ})$ is used in some of the following studies. The direction of the new system is shown in Fig. 9.4(b). The $RX = 0$ position in the new system is the plane where the MCP-PMT sits. The $RY = 0$ and $RZ = 0$ point is the top left corner shown in this Figure.

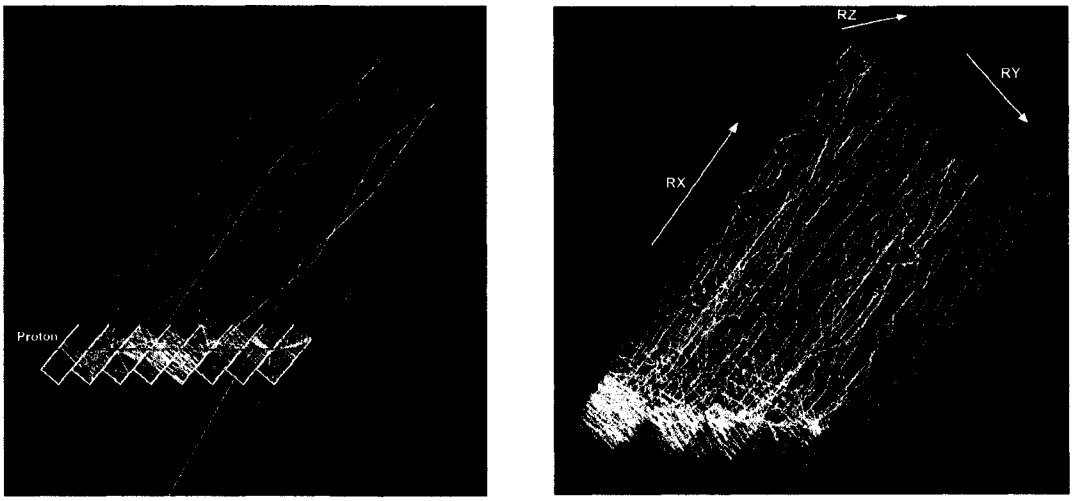

(a) (b)

Figure 9.4: *(a). A proton crossing the quartz bars generate Cerenkov photons that traverse the quartz bars and the hollow light guides; (b). 3D view of QUARTIC in simulation and the definition of* $(\vec{RX}, \vec{RY}, \vec{RZ})$.

The simulated hit positions of photons on the MCP-PMT surface can be used to understand the performance of the detector and also to validate the simulation program. The hit positions of photons in the redefined coordinate system $(\vec{RX}, \vec{RY}, \vec{RZ})$ is shown in Fig. 9.5. Only the photons that produce a photo-electron in the MCP-PMT photo-cathode are included in these plots.

Since the PMT surface is at the $RX = 0$ plane, all photons in the RX distribution fall in the same $RX = 0$ bin. From the RZ distribution, almost all photons arrive within the range of the light guide (6 mm size). The small number of photons in the neighbor channels are due to the Cerenkov photons produced by secondary charged particles introduced by protons crossing the

detector material.

In the *RY* distribution, the channel layout is obvious. A channel with smaller *RY* corresponds to a channel that is closer to the interaction point (with a longer light guide). In longer channels, since the number of reflections is bigger, a smaller number of photons arrive at the PMT surface. The structure in each individual bar is due to the different length of the light guide. The propagation of the photon in the hollow light guide determines the hit position of the photons.

9.3.3 Time and Wavelength Distribution of Photons

The time response of the detector is the critical factor in the overall detector performance. Fig. 9.6, Fig. 9.7 and Fig. 9.9 show the arrival time of the photons and the Time-Wavelength contour plots of the photons that produce a photo-electron. The arrival time of the photons is the time when the photon reaches the face plate of the MCP-PMT. Fig. 9.9 (lower) shows the arrival time distribution of all channels. There are eight peaks all together, which corresponds to 8 channels in the detector. The 10 ps increase in delay for each channel, moving from left to right across the plot, is due to the increase in length of the correspond light guide, increasing with a 4.5 mm pitch, as well as the delay of the proton from one bar to the next one.

Fig. 9.9 (upper) shows the Time-Wavelength contour plot. Two conclusions can be made from this plot: a) the shorter-wavelength photons arrive later than longer-wavelength ones, because they travel with different speeds in fused silica; b) there is a cut around 500 nm due to the fall off of the quantum efficiency of MPC-PMT for photons around that wavelength, or greater.

9.3.4 Time Resolution

Three main factors affect the time resolution of the QUARTIC detector: a) the spread in arrival time of photons at the photocathode, b) the time resolution of the MCP-PMT, dominated by the transit time spread, TTS, of the electrons from emission at the photocathode to arrival at the anodes, and c) the downstream electronics, including signal dispersion in cables. The first factor is minimized using an optimized geometrical design. The MCP-PMTs

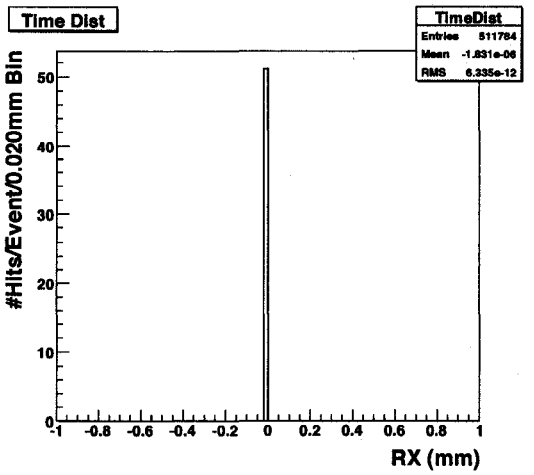

(a)

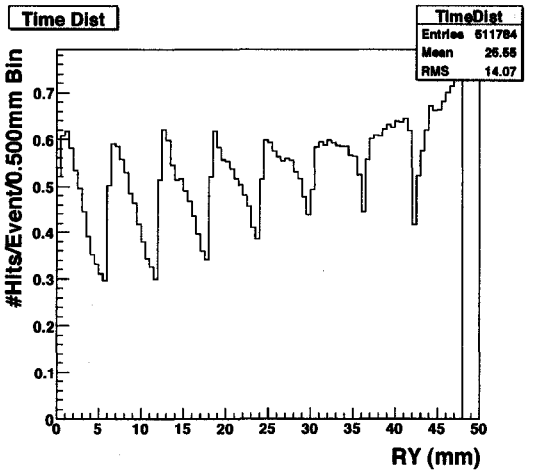

(b)

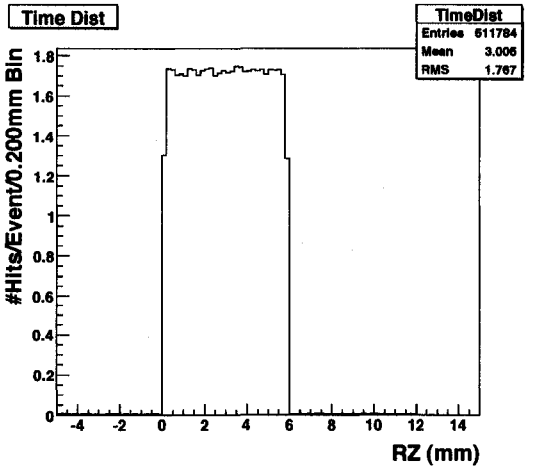

(c)

Figure 9.5: *Positions where the photon-electrons are produced, assuming the PMT is a perfect plane at RX=0. The axis is defined as in Fig. 9.4(b)*

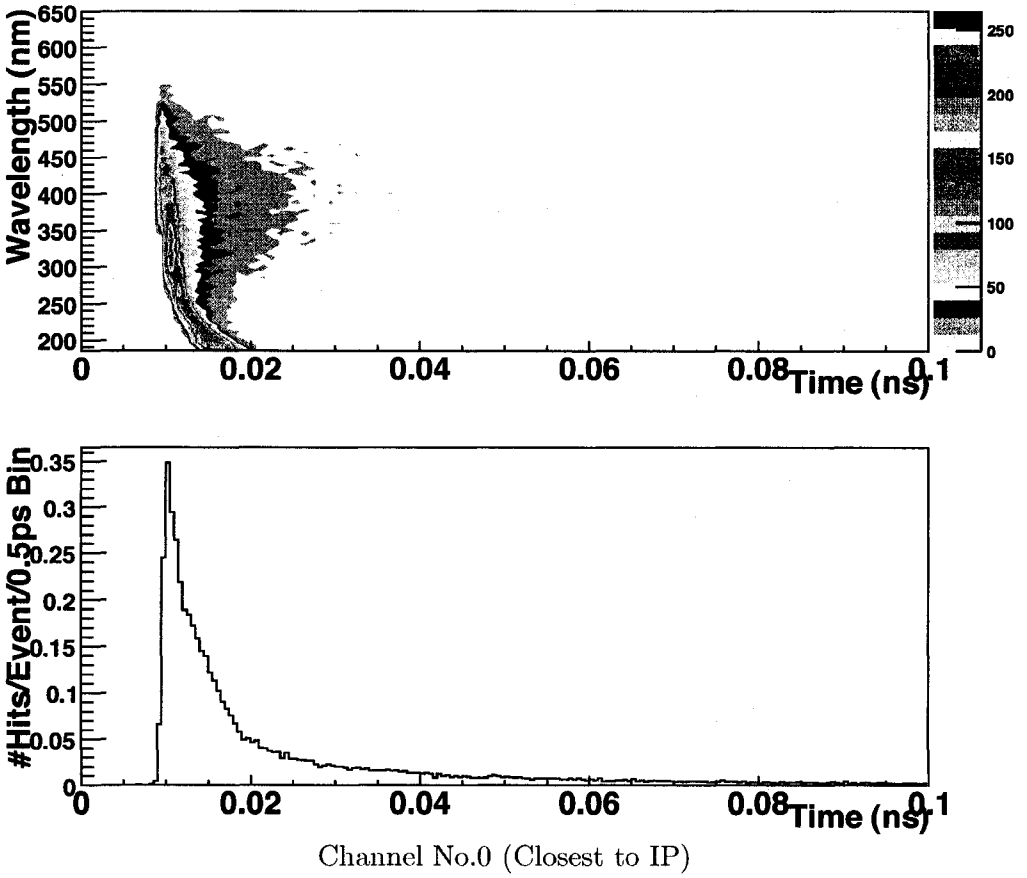

Figure 9.6: *Distribution of photon arrival times at the PMT surface (lower plots), and the contour plot for photo-electron density in time-wavelength space (lower plots), in channel 0. Time 0 is the time when the first photon arrives at the MCP-PMT face. The photon arrival time equals to the photo-electron production time, because only those photons that produce a photo-electron are included.*

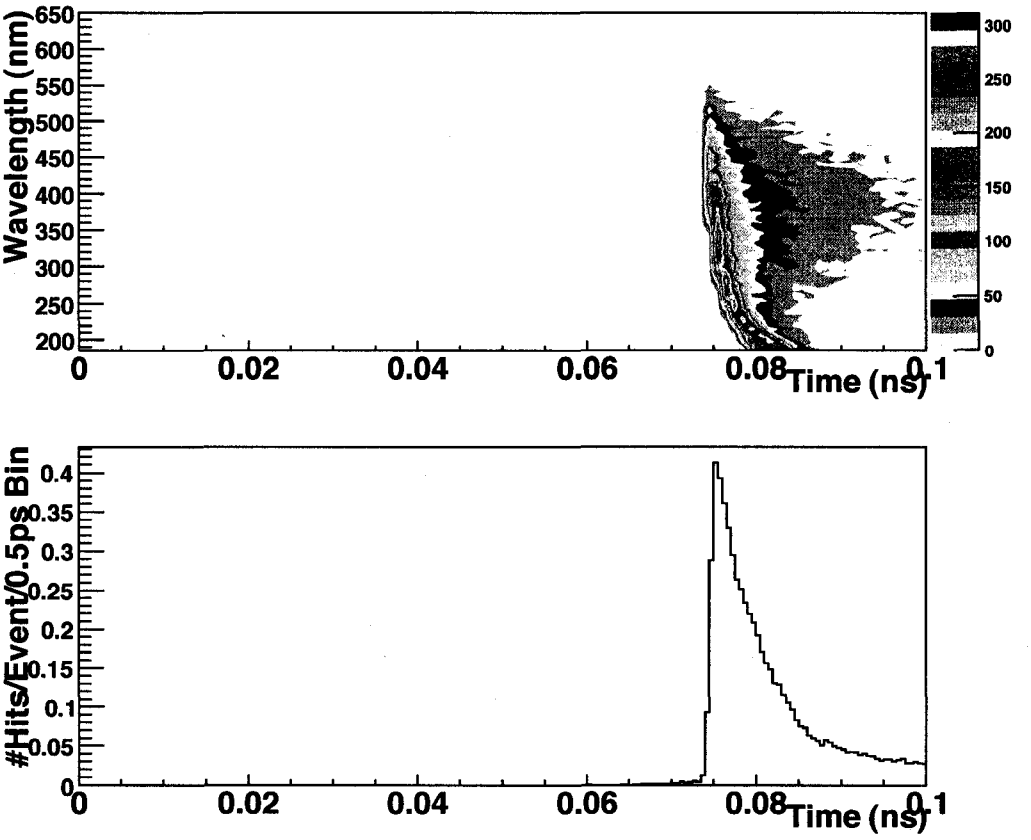

Channel No.7

Figure 9.7: *Distribution of photon arrival times at the PMT surface (lower plots), and the contour plot for photo-electron density in time-wavelength space (lower plots), in Channel 7. Time 0 is the time when the first photon arrives at the MCP-PMT face. The photon arrival time equals to photo-electron production time, because only those photons that produce a photo-electron are included.*

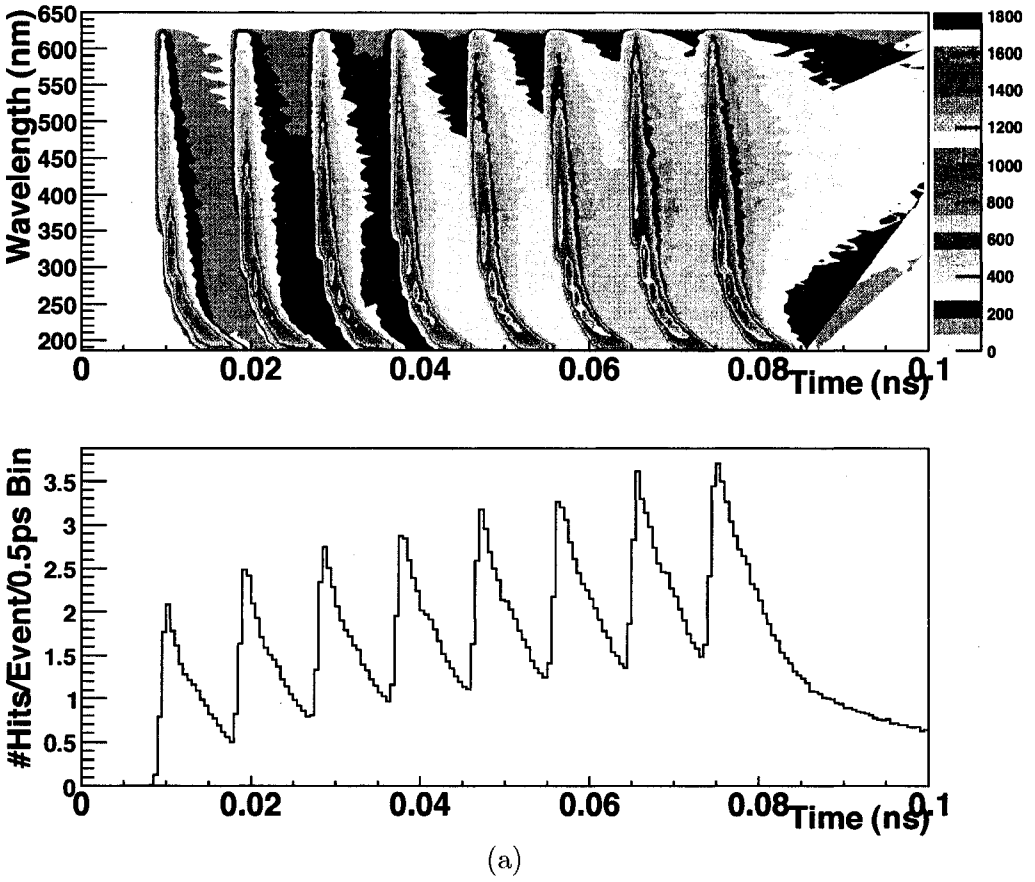

(a)

Figure 9.8: *Effect of PMT quantum efficiency. The plot shows the arrival time distribution and time-wavelength contour plot for photons that arrive at the PMT surface.*

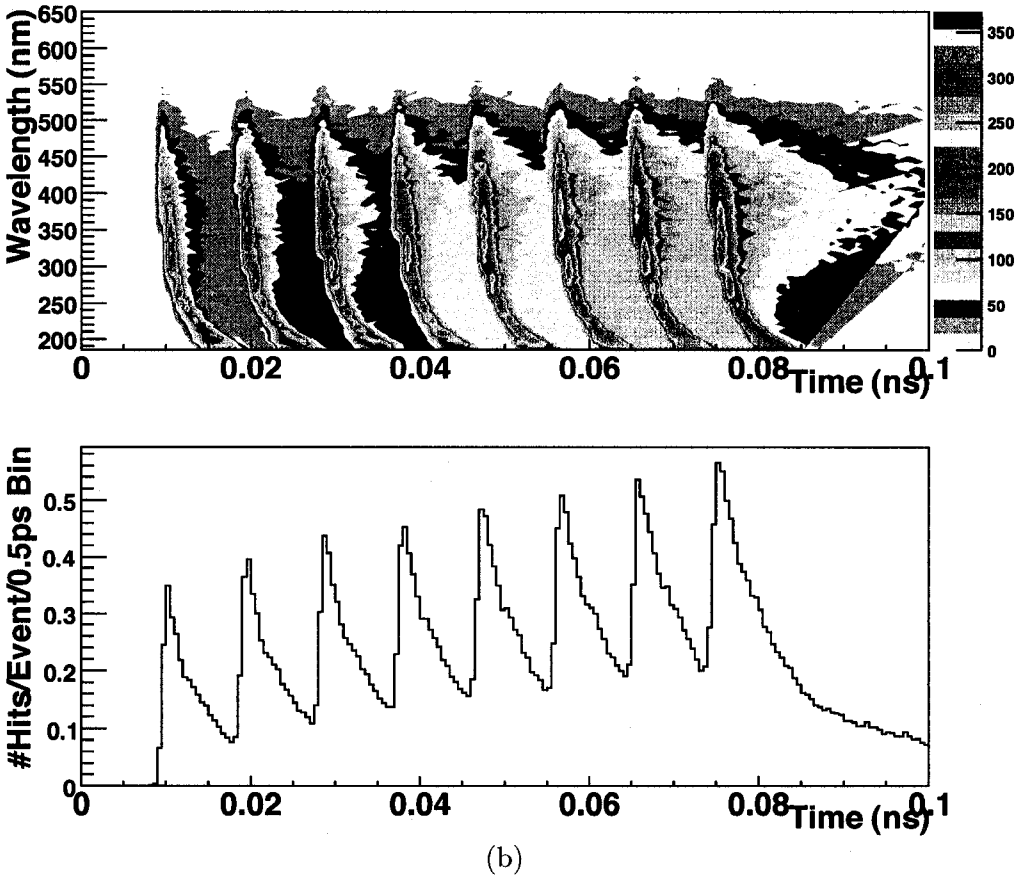

(b)

Figure 9.9: *Effect of PMT quantum efficiency. The plot shows the arrival time distribution and time-wavelength contour plot for photons that arrive at the PMT surface and generate a photo-electron.*

we are considering have a small TTS (~30 ps) for a single photo-electron.

To determine the best achievable time resolution of the detector, arrival time distributions for the longest (0) and shortest (7) channel were studied (Fig. 9.10). More than 80% of the photo-electrons are produced within a 6 ps window. The time dispersion due to MCP-PMT/electronics is not modeled in the simulation.

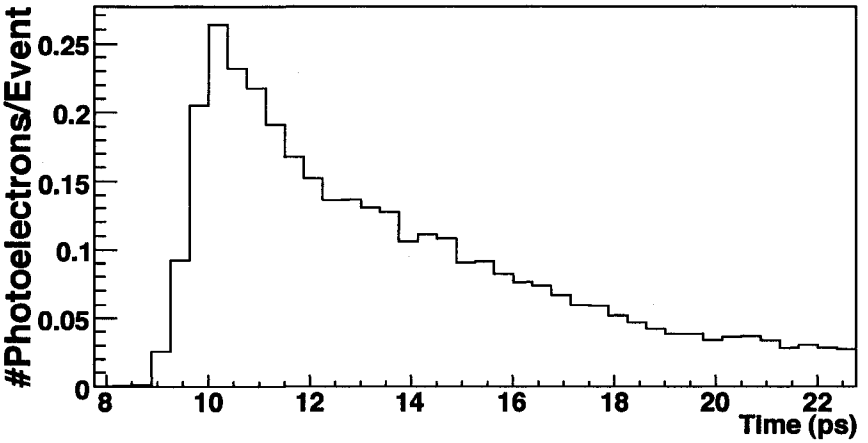

Channel 0

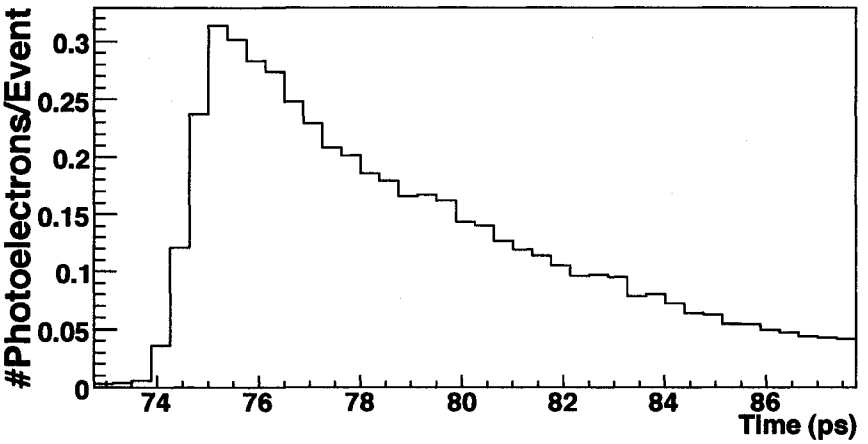

Channel 7

Figure 9.10: *Photon arrival time distribution for channel 0 and 7, as in Fig. 9.6 and Fig. 9.7. The time axis is in picoseconds. 80% of the photo-electrons are produced within a 6 ps window.*

9.3.5 Effect of PMT Quantum Efficiency

The effect of the quantum efficiency of the PMT is illustrated in Fig. 9.8, which shows the time distribution and time-wavelength contour plot for all photons, and and Fig. 9.9, which shows only photons that produce a photo-electron. The relative height of the 8 peaks remains unchanged, however, from the contour plot, photons with wavelength longer than ~500 nm are heavily suppressed. On average, ~ 15% of the Cerenkov photons produce a photo-electron on the PMT cathode.

9.3.6 Number of Photoelectrons

With a data sample of 10,000 events, distributions of the number of photo-electrons collected in each PMT channel is shown in Fig. 9.11. The average number of photo-electrons ranges from 2.5 to 3.5 per channel for different channels. The shortest channel gives the largest number of photo-electrons.

9.4 Test beam and Preliminary Results

By utilizing 3D printing technology, the QUARTIC prototype, as designed in CAD, was "printed" out. As shown in Fig. 9.12 (left), aluminum foils were glued to the inner wall of the channels, and a fused silica bar was inserted. A base was also "printed" for accurate alignment of the channels to the MCP-PMT.

Measurements of prototype QUARTICs have been made in the Fermilab test beam (150 GeV protons). Two QUARTICs QA(channels 1-8) and QB(channels 1-8) were setup as shown in Fig. 9.13. A picture of the setup is shown in Fig. 9.14. The test also includes GasTOF, which is a gas Cerenkov time of flight detector being developed for FP420. The GasTOF is not described in this thesis.

QA and QB used the Burle 85011-501 with 25 and 10 μm pores respectively. The signal for the MCP-PMT's was amplified using a 1 GHz amplifier, passed through a constant fraction discriminator (CFD), and read out by a Phillips 7186 TDC. Several types of amplifiers were tested: ORTEC 9306, Phillips BGA2712, Hamamatsu C5594, and Mini-Circuits ZX60-14012L. Several dif-

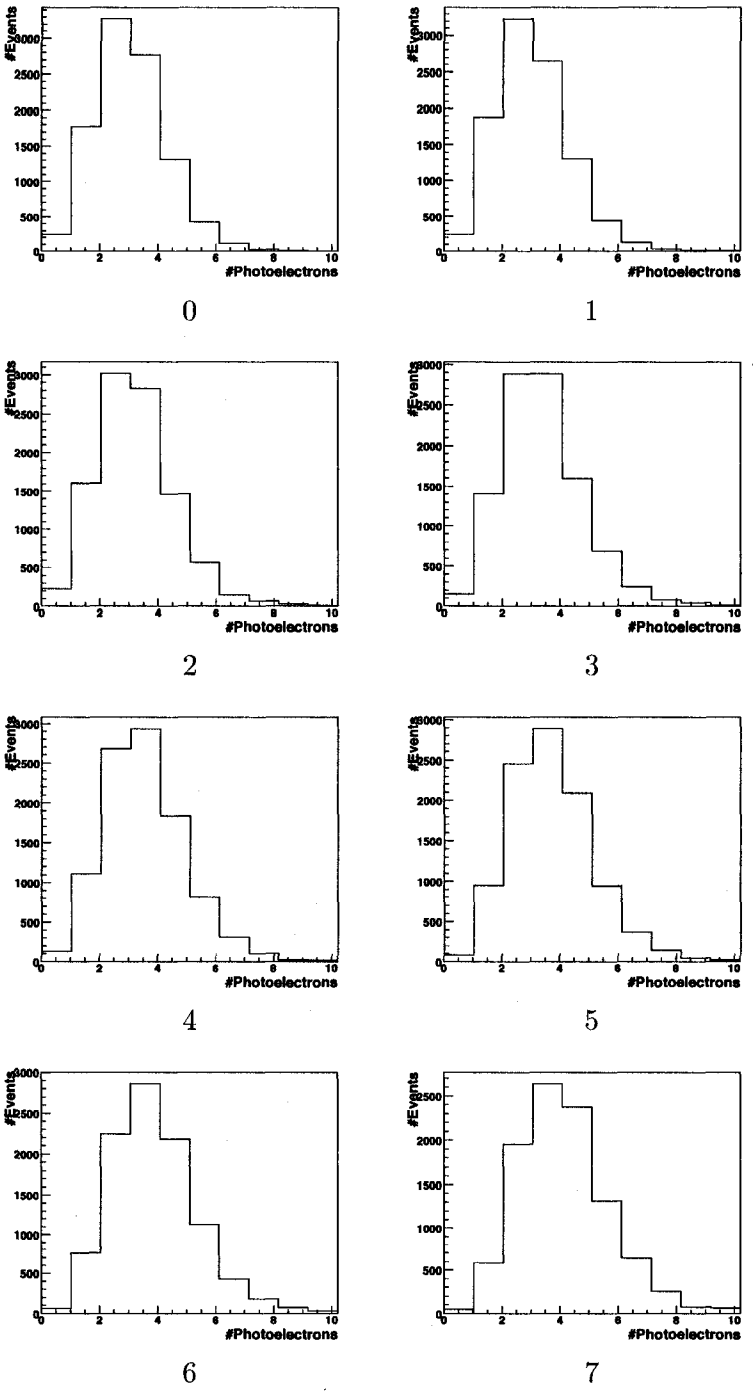

Figure 9.11: *Distribution for the number of photo-electrons per event in each channel.*

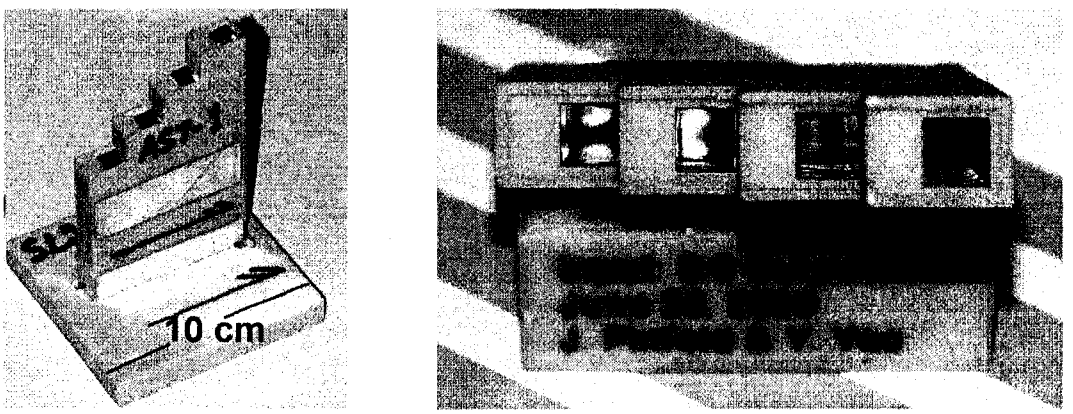

Figure 9.12: *The 3D–printed QUARTIC prototype.*

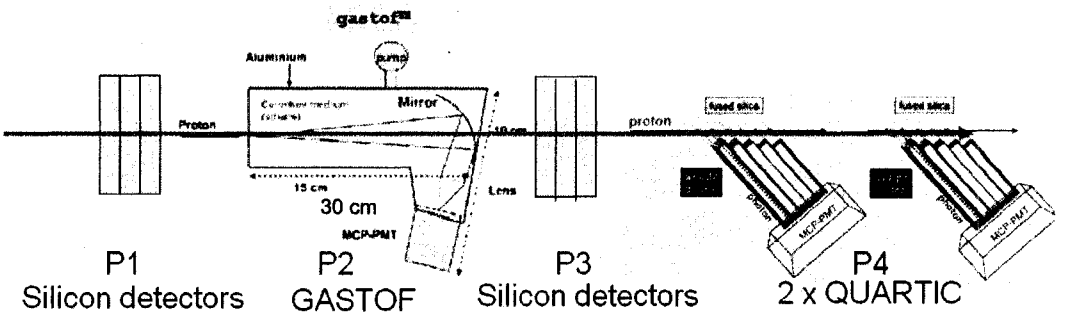

Figure 9.13: *QUARTIC test beam setup.*

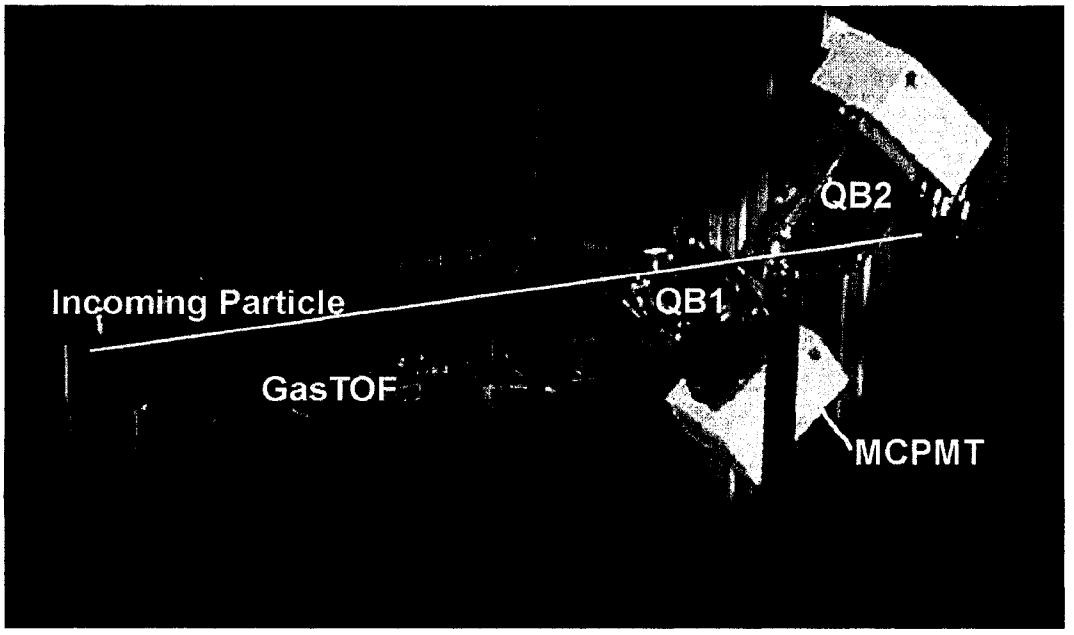

Figure 9.14: *Picture of QUARTIC the test beam setup.*

ferent CFD's were also used: ORTEC 934, ORTEC 9307, and a Louvain-made CFD circuit. A CAMAC based data acquisition system was used, triggered by scintillator tiles located on either end of the detector setup. Multiwire proportional chambers provided track position information.

The average resolution of a QUARTIC channel combining MCP-PMT and electronics was found to be ~82 ps/bar[1] [75]. Using an observed 80% bar efficiency and assuming no channel-to-channel correlations, we would get about 13 measurements instead of 16 (two QUARTIC prototypes), which gives us an estimated QUARTIC only resolution of 23 ps.

The pulse of a QUARTIC signal in the test beam is found to be 2-3 photo-electrons, which is consistent with the simulation result. The $1/\sqrt{N}$ improvement in resolution is also observed in the test beam. A final analysis of the test beam data is still underway.

9.5 Simulation Study of an Alternate QUARTIC Design

An alternate design of QUARTIC detector is shown in Fig. 9.15. 6×15 mm fused silica bars are used. The aluminum hollow light guides are "dog leg" shape. Each light guide consists of two Right Angular Wedges (Trapezoid), which allow the MCP-PMT face to be parallel to the beam line. This design has two advantages over the previous design: 1) the MCP-PMT face is parallel to the beam line. Since most of the beam related background particles are expected to be mostly roughly parallel to the beam axis, the Cerenkov photon production in the face plate can be minimized; 2) the length of the light guide and the fused silica bar can be reduced (several mm) comparing to the previous design, without putting the MCP-PMT too close to the beam.

Fig. 9.16 shows the simulated QUARTIC channel 0 (closest to IP) and channel 7, with the path of proton (blue) and photons (green). The same parameters of aluminum, fused silica and MCP-PMT quantum efficiency are used as in the previous design.

Fig. 9.17 shows the distribution of the number of photo-electrons for chan-

[1]Resolution is the half width of the photo-electron peak.

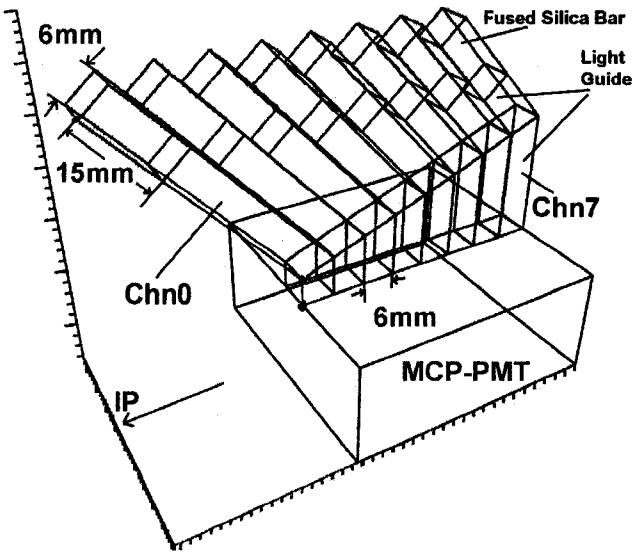

Figure 9.15: *Alternate QUARTIC design.*

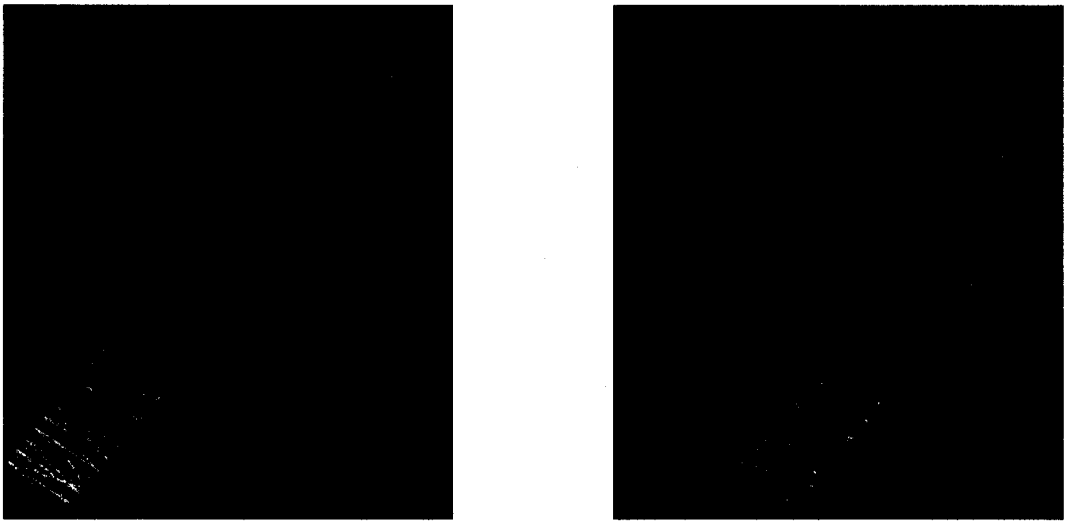

Figure 9.16: *Simulation of alternate QUARTIC design for channel 0 (left) and channel 7 (right), showing the photon and proton path.*

nel 0 and channel 7. The average number of photo-electrons for channel 0 is ~5.5, and for channel 7 is ~3.5, 30%-40% larger than in the previous design. This is due to the fact that the angled light guide is less selective to the direction of incoming photons.

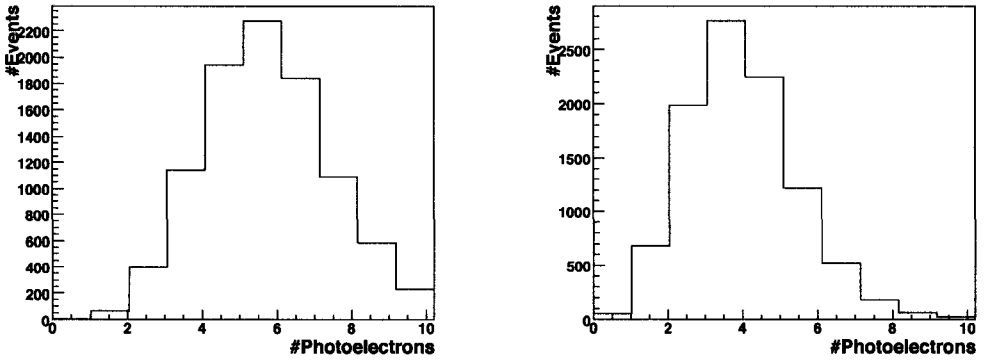

Channel 0 Channel 7

Figure 9.17: *Distribution of number of photo-electron produced in MCP-PMT for channel 0 and channel 7.*

Fig. 9.18 shows the arrival time distribution of the two channels. The width of the peaks are ~10 ps for channel 0 and ~ 20 ps for channel 7. This is also due to the fact that the angled light guide is less selective to the direction of incoming photons. The out of time photons are also non-pointing photons in most cases. However, with the multiple channel measurement capability, the required resolution of below 20 ps can also be achieved.

A prototype of this QUARTIC design was fabricated and was tested in the test beam experiments in late 2007.

9.6 Conclusion

From the simulation study of two QUARTIC designs, 2.5-3.5 photo-electrons are expected in the original design and 3.5-5.5 photo-electrons in the alternate design. A 23 ps ToF resolution was achieved under test beam conditions. A 20 ps ToF resolution corresponds to a vertex position resolution of 4.2 mm. Our test beam experience indicates that a time resolution for QUARTIC of ~ 10 ps is achievable.

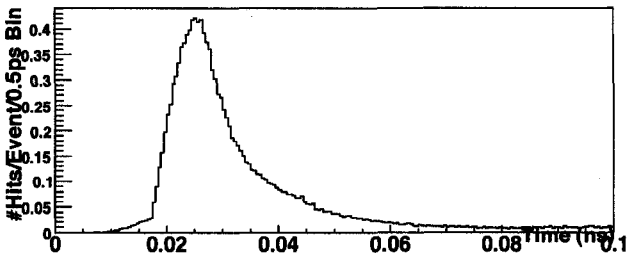

Channel 0

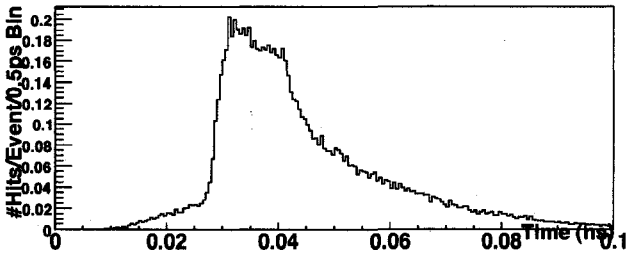

Channel 7

Figure 9.18: *Time distribution of photo-electron produced in MCP-PMT for channel 0 and channel 7.*

Chapter 10

Calibration of FP420 with Muon Pair Production

10.1 Introduction

As discussed in previous chapters, the physics channels to which FP420 is sensitive include exclusive QED muon pair production (Fig. 10.1). The muon pair is created in the central region of ATLAS. This process has been measured in lepton colliders and is well understood [76]. The cross section for this process is relatively high (21 pb with both muons $|\eta| < 2.5$ and $p_T > 3$ GeV[1]). ATLAS (or CMS) can provide high resolution measurement of η and p_T of the central muons. This make it one of the best candidates for the energy calibration of FP420, providing around two thousand calibration events per week at LHC medium luminosity ($10^{33}\,\mathrm{cm}^{-2}\mathrm{s}^{-1}$).

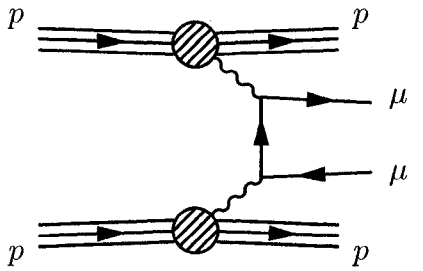

Figure 10.1: *Feynman diagram for two−photon muon pair production.*

[1]The cross-section is obtained from the LPAIR event generator.

10.2 Procedure

This thesis utilizes simulation software (LPAIR [21], FPTracks [77], ATLAS Simulation [78]) to study this method for calibrating the FP420 detectors. In this study, the LPAIR package is used to simulate the process $pp \rightarrow p\gamma\gamma p \rightarrow p\mu\mu p$ using a full matrix calculation. The two muons produced by the simulation are passed into the full ATLAS simulation, which provides the detected (reconstructed) muon energy and direction information. The two protons are passed into the FPTrack package. FPTrack simulates the proton trajectory in the very forward direction.

For a specific event (either real or generated by LPAIR), if at least one outgoing proton is detected by FP420 and both muons are detected (reconstructed) by the ATLAS detector, then this event can be used as a calibration event.

The flow chart of the procedures is shown in Fig. 10.2.

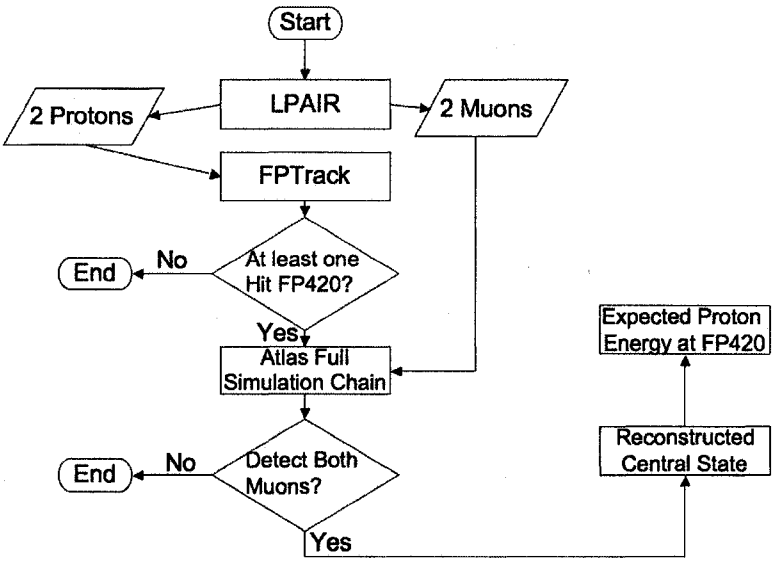

Figure 10.2: *The flow chart for the study of calibration of FP420.*

10.3 Results

The process cross-section is 21.1 pb with the cut when both muons have $|\eta| < 2.5$ and $p_T > 3$ GeV. A sample of 10^5 events are produced by LPAIR,

which corresponds to a data collection time of 55 days with a luminosity of $10^{33}\,\mathrm{cm}^{-2}\mathrm{s}^{-1}$. The pseudo-rapidity cut is selected to match to acceptance of the ATLAS muon system of $|\eta| < 2.5$, and it has a good sensitivity to muons with transverse momentum down to 3 GeV (if we include the proposed low p_T muon trigger from the Tile Calorimeter). The detection efficiency of the muons with respect to p_T for various muon reconstruction algorithms is shown in Fig. 10.3 [79].

In the first step, the protons were passed through FPTrack, 38.7% of these events have at least one proton detected in FP420. In the second step, the central muons in the event selected in the first step are then passed through the ATLAS simulation, and 45% of the events have both muons successfully detected and reconstructed by ATLAS. Events that pass the selection in the second step are used for the calibration.

In total, the number of usable events is

$$n = \sigma \cdot L \cdot \epsilon_1 \cdot \epsilon_2 \cdot t, \tag{10.1}$$

where σ is the cross section determined in LPAIR (21 pb), L is the luminosity, ϵ_1 is the efficiency in the first step (38.7%), ϵ_2 is the efficiency in the second step (45%) and t the time of data taking. At luminosity $L = 10^{33}\,\mathrm{cm}^{-2}\mathrm{s}^{-1}$ (which is one tenth of the full LHC luminosity), one week of data taking can result in $\sim$ 2500 calibration events.

10.3.1 Detection of Protons by FP420

The energy and pseudo-rapidity distributions of the protons at different stages (production, step 1 and step 2) are shown in Fig. 10.4. The detected proton energy loss cut-off can be clearly seen at around 15 GeV (Fig. 10.4 (left), proton energy cut-off 6985 GeV, which corresponds to energy loss 15 GeV), this is consistent with the fractional energy loss > 0.02 predicted in FP420 TDR. The first selection cut events with $\eta > 16$ because the detector is not close enough to the beam to detect the protons with such small deflection angles.

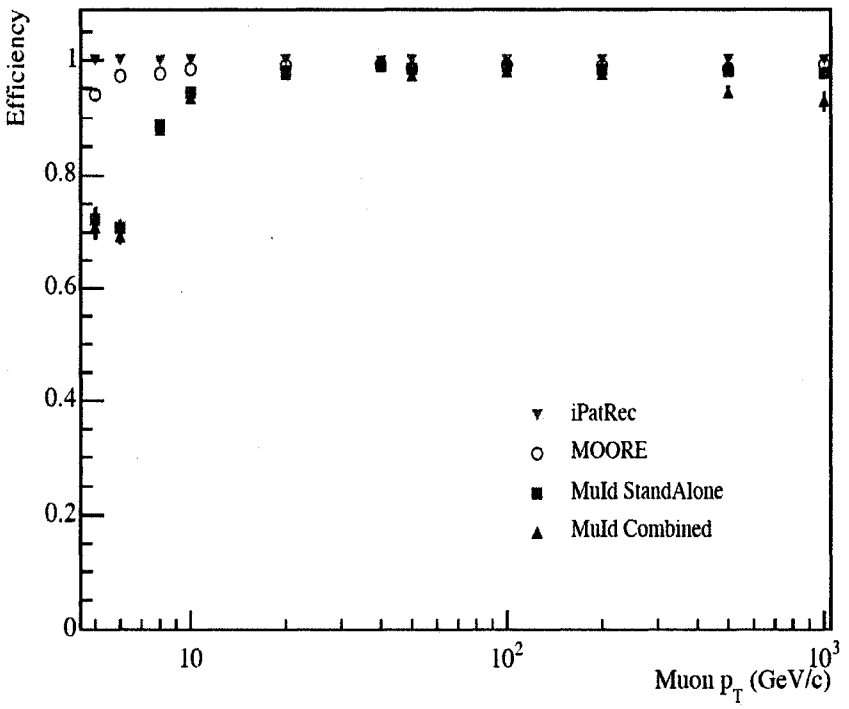

Figure 10.3: *The reconstruction efficiency for ATLAS muon system with different reconstruction software, MOORE and Muid are the major algorithms used in the offline reconstruction.*

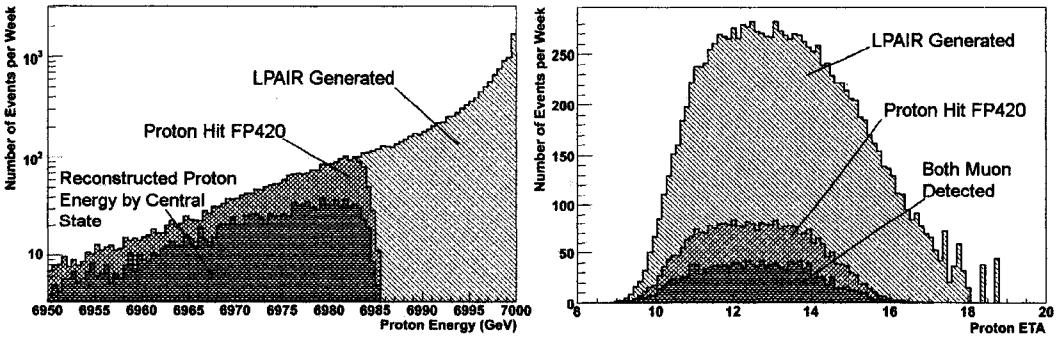

Figure 10.4: *The energy (left) and η (right) distribution of the protons when they are generated by LPAIR, and when they pass the first step and the second step.*

10.3.2 Reconstruction of Central State

Fig. 10.5 shows the reconstructed p_T of the muons from the ATLAS simulation. The relative number of events can be seen from the different curves. The suppression of lower p_T muons observed when we compare curve 1 to curve 2 is due to the lower limit of proton energy loss to which FP420 is sensitive. The suppression of lower p_T muons from curve 2 to curve 3 is due to a lower detection/reconstruction efficiency of the ATLAS muon system.

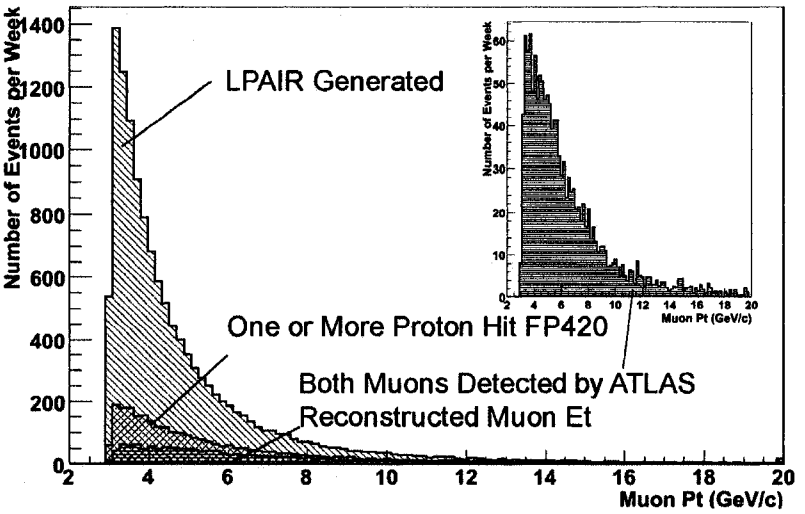

Figure 10.5: *Comparing the distribution for muon p_T. 1) as they are produced by LPAIR; 2) as they pass the selection of step 1; 3) the reconstructed muons p_T as they pass the selection of step 2.*

The muon pair constitutes the central state (Fig. 10.6). As expected the FP420 detectors are not sensitive to central states with energy smaller than $\sim$ 15 GeV. Fig. 10.7 shows the central state selection efficiency with respect to central state energy.

10.3.3 Precision of the Calibration

The precision of the calibration method relies on the measurement precision of the 4-vectors of the muon pair. Since this study permits us to save the real 4-vectors of the muons (so called MCTruth), by subtracting the measured value by the real value, the p_T and η resolution can be obtained. The average value of η and p_T are used for this purpose. Fig. 10.8 (left) shows the resolution for

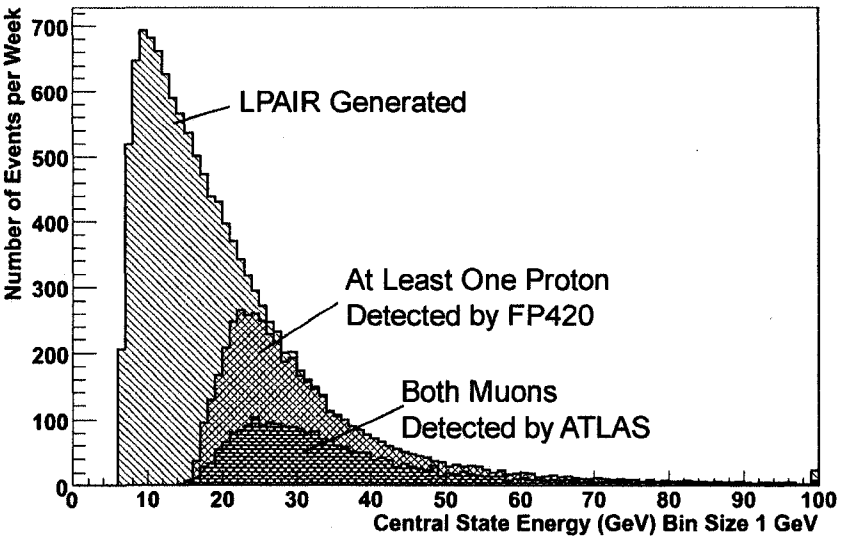

Figure 10.6: *Distribution of central state energy. The upper two curves are from the central state energy generated by LPAIR, the lower curve is from the reconstructed central state energy from ATLAS full simulation.*

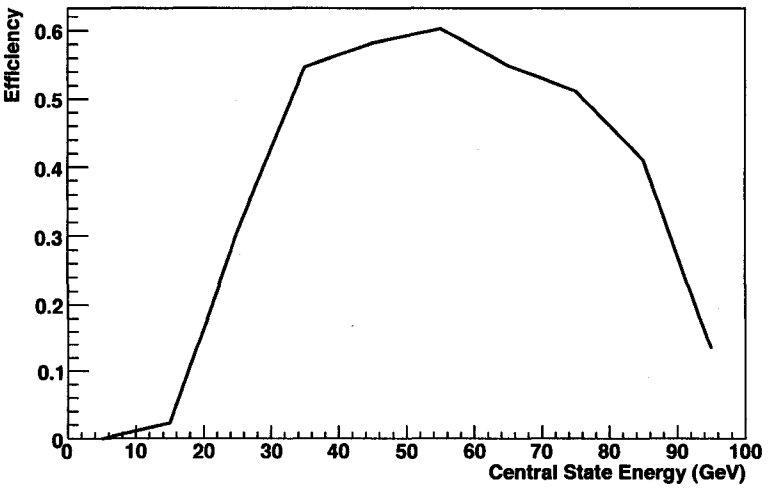

Figure 10.7: *Selection efficiency as a function of central state energy.*

muon η. The RMS of ~ 0.001 is consistent with the predicted ATLAS muon resolution. Fig. 10.8 (right) shows the resolution for muon p_T, it has a RMS of ~ 161 MeV.

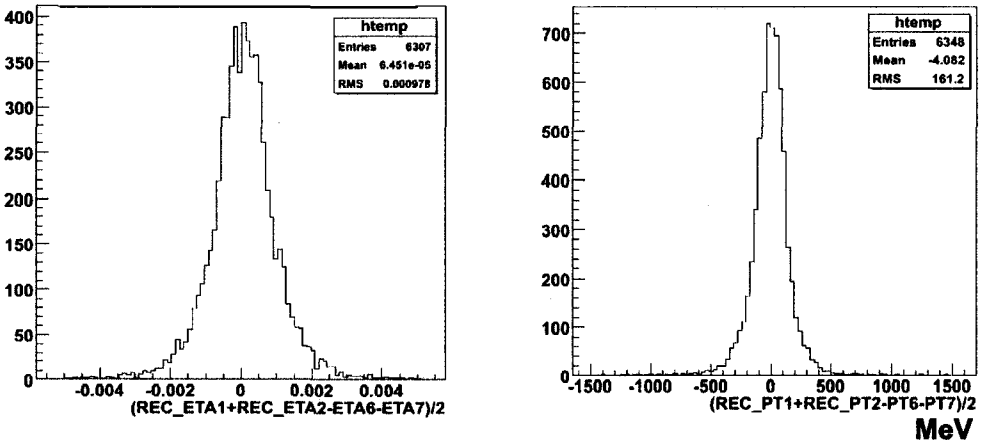

Figure 10.8: *Difference between the real muon η and the reconstructed muon η (left), and the difference between the real muon p_T and the reconstructed muon p_T (right, in MeV), for all events passing the second selection. Note that the average η and p_T of the muon pair are used in the histograms.*

If we assume the fractional energy loss of the proton is very small, then the proton's transverse momentum can be neglected. With the measured muon energy and pseudo-rapidity, $E_{T\mu 1,2}$ and $\eta_{\mu 1,2}$, the energy loss ($E_{\gamma 1,2}$) of the proton can be written as

$$\begin{aligned} E_{\gamma 1} &= \tfrac{1}{2}\left(\frac{E_{T\mu 1}}{sin\theta_1} + \frac{E_{T\mu 2}}{sin\theta_2} - \frac{E_{T\mu 1}}{tan\theta_1} - \frac{E_{T\mu 2}}{tan\theta_2}\right), \\ E_{\gamma 2} &= \tfrac{1}{2}\left(\frac{E_{T\mu 1}}{sin\theta_1} + \frac{E_{T\mu 2}}{sin\theta_2} + \frac{E_{T\mu 1}}{tan\theta_1} + \frac{E_{T\mu 2}}{tan\theta_2}\right), \end{aligned} \tag{10.2}$$

where $\theta_{1,2} = 2 \times \tan^{-1}(e^{-\eta_{1,2}})$ are the angle between the momentum direction and the beam axis. The proton energies are

$$\begin{aligned} E_1 &= 7\,\text{TeV} - E_{\gamma 1}, \\ E_2 &= 7\,\text{TeV} - E_{\gamma 2}, \end{aligned} \tag{10.3}$$

and the fraction energy loss:

$$\begin{aligned} \xi_1 &= E_{\gamma 1}/E_1, \\ \xi_2 &= E_{\gamma 2}/E_2. \end{aligned} \tag{10.4}$$

The distribution for one of the proton's calculated energy and fraction energy loss is shown in Fig. 10.9. The RMS of the energy distribution (Fig. 10.9 left) is $\sim$ 900 MeV, which corresponds to an RMS $\sim 10^{-4}$ (%0.01) in the energy loss distribution (Fig. 10.9 right).

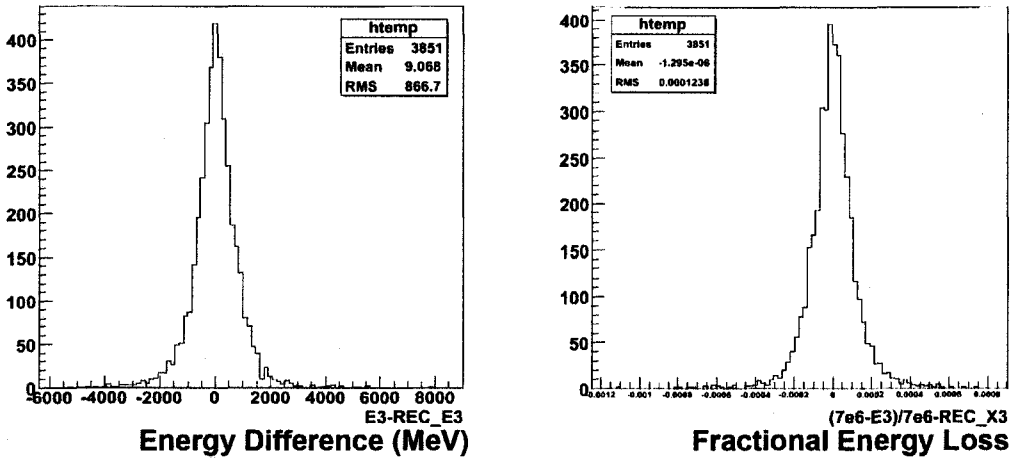

Figure 10.9: *Difference between the real proton energy (energy loss) and the calculated proton energy (energy loss), for all usable events and for the $z > 0$ side proton only.*

10.4 Conclusion

Under the ideal working condition of ATLAS (as in simulation), the above described method can be used to calibrate the proton energy with a resolution of $\sim$ 900 MeV. Since the measurement of two protons are independent, the resolution for the central state energy is $\sim$ 1.8 GeV. This calibration method is one possible way to achieve the high precision measurement of the central state energy in the FP420 detectors, providing around 2500 events per week at luminosity $10^{33}\,\mathrm{cm}^{-2}\mathrm{s}^{-1}$.

Chapter 11

Conclusion

The ATLAS detector construction is now completed and ATLAS is ready to explore the widest possible range of physics signals after the LHC collider begins running in 2008, at an unprecedented centre of mass energy. An accurate luminosity determination is required to calculate the cross-section for observed processes. The measurement of the luminosity requires a detector designed for, and dedicated to, the task. This detector and its upgrades must be capable of covering the full luminosity range of ATLAS.

LUCID is a luminosity monitor proposed by the Alberta ATLAS group, approved by the ATLAS Collaboration in February 2007 and constructed in collaboration with the University of Bologna, CERN and Lund University in 2007. Phase-I of LUCID, designed to cover low to medium ATLAS luminosities (up to $5 \times 10^{33}\,\mathrm{cm}^{-2}\mathrm{s}^{-1}$), will be installed in March 2008. Phase-II LUCID installation is planned for 2010, prior to high luminosity running. Although a Phase-II LUCID baseline design is already in place it is envisaged that this design will necessarily be modified as we gain experience with Phase-I. The challenges that the Phase-II design has to face are increased radiation levels and a possible role for the Phase-II detector in the forward physics program.

LUCID will initially provide luminosity measurements, calibrated with respect to machine measurements, of accuracy of approximately 10%. In the interim we hope to make use of physics processes such as $\gamma\gamma \rightarrow \mu^+\mu^-$ and W/Z counting to provide an additional calibration. In this case, we could see and improvement of the luminosity resolution in the range 5-10%. In 2009-2010 it is envisaged that ATLAS will make a measurement of elastic $p - p$

scattering in the Coulomb region, using the ALFA detects deployed in Roman Pots at ±220 m from the ATLAS intersection point. This measurement will allow us to make a direct calibration of LUCID that can be transferred to higher luminosities. Using this calibration we envisage that a final luminosity resolution determination using LUCID of a few percent is achievable.

As one of the founding members of the LUCID group at Alberta I was for the first two years solely responsible for the simulation of the LUCID detector. In 2005 when the Bologna group joined the effort I became the leader of the simulation group. The simulation of the LUCID detector reported in this thesis is my work. It provided the necessary input to assess: the design of the light collection (Winston Cone and Straight Cone); specifying the Fibre Bundle fabrication; the Cerenkov tube parameters; choosing the radiator gas; determining the working pressure and specifying the PMTs, etc.. I also took part in bench tests of the LUCID Cerenkov tube reflectivity at Alberta and two test beam experiments at DESY in Germany. My test beam responsibilities were primarily to compare the test beam measurements with the simulation in situ, as well as to take part in test beam setup and running.

A major concern in the design and deployment of the LUCID detector is the determination of the effect of the soft and hard backgrounds from beam related processes at the LUCID position and comparing them to the expected signal. I created a LUCID-specific simulation of the ATLAS detector from the intersection point of ATLAS to the LUCID detector up to the LUCID detectors ±17 m away. This simulation was compared and contrasted with the official ATLAS background and signal estimates in the vicinity of LUCID. I lead the LUCID effort in this area until LUCID was officially approved by the ATLAS group in February 2007. The study of LUCID Phase I detector simulation that I made was crucial in providing the understanding the background, the luminosity measurement method, the performance of LUCID, and the systematic error of luminosity measurement. The final approval of the LUCID by the ATLAS Collaboration would not have been forthcoming without this input.

The forward region of ATLAS is now an active and exciting area of development include the:

- LUCID detector (approved);

- Zero Degree Calorimeter (approved);
- The ALFA project (pending approval);
- the FP420 project (R&D phase).

The aim of the FP420 project is to deploy precision silicon detectors in Roman Pots, or Hamburg pipes, at ±420 m from the ATLAS intersection point, in order to measure the trajectory of protons deflected from peripheral and ultra-peripheral collisions. This will allow the kinematics of the central state to be calculated. A key element of this program is the measurement of the diffractive Higgs boson signal as well as other Standard Model and SUSY processes.

Owing to the small cross-sections expected it is important that FP420 can run at medium and high luminosity. To be effective some method of pile-up background suppression is needed. I was one of the founding members of QUARTIC group that proposed we deploy precision Time of Flight (ToF) detectors adjacent to the FP420 tracking detectors in order to suppress pile-up background. The QUARTIC detector consists of an array of four rows of quartz bars that are 8 bars deep read out by microchannel plate PMTs (MCP-PMTs). It is planned that two QUARTIC detectors are deployed by each FP420 detector, giving 16 measurement of the ToF of each deflected proton.

I was in charge of the GEANT4 simulation of the QUARTIC detector. This simulation, reported in this thesis, tested various geometries, light guides, radiators, and MCP-PMT properties. In addition, I constructed the light guide system and quartz bar deployment mounts for the second QUARTIC prototype, utilizing the three dimensional plotter at the University of Alberta.

I helped show from my simulation studies that the QUARTIC detector could obtain ToF resolutions of <10 ps/bar giving 3-4 photoelectrons in each channel. If this is convoluted in quadrature with a contribution to the resolution from the readout electronics, estimated to be 30 ps/bar, the overall resolution is expected to reach approximately 40 ps/bar. If each bar is 100% efficient the 16 measurements of each deflected proton made by QUARTIC allow a ToF precision of 40 ps. This would give an overall precision of 10 ps ToF resolution, enabling the measurement of the vertex position of ~2 mm in the

Z-coordinate. Such a resolution would allow around a factor of 50 reduction in the main pile-up background channel.

An important requirement for the success of the FP420 project is the ability to calibrate the detectors. To this end I investigated the use of the exclusive two photon di-muon production ($pp \rightarrow p\gamma\gamma p \rightarrow p\mu\mu p$) which provides around 2500 events per week at a luminosity of $10^{33}\,\mathrm{cm}^{-2}\mathrm{s}^{-1}$. The results of my simulation study, that combined the LPAIR MC and the ATLAS full simulation, showed that we could calibrate the energy measurement of FP420, with a resolution < 2 GeV, using the above processes.

Bibliography

[1] ATLAS Calibration. Atlas: Detector and physics performance. technical design report. vol. 2. 1999. CERN-LHCC-99-15.

[2] David J. Griffiths. Introduction to elementary particles. NEW YORK, USA: WILEY (1987) 392p.

[3] Lep electroweak working group, status of august 2005. *http://lepewwg.web.cern.ch/LEPEWWG/.*

[4] C. E. Vayonakis. On the unitarity limits of top quark and higgs boson masses. *Europhys. Lett.*, 12:29, 1990.

[5] R. Barate et al. Search for the standard model higgs boson at lep. *Phys. Lett.*, B565:61–75, 2003.

[6] Atlas: Detector and physics performance. technical design report. vol. 1. CERN-LHCC-99-14.

[7] *Total cross-section, elastic scattering and diffraction dissociation at the Large Hadron Collider at CERNTOTEM Technical Design Report.* Technical Design Report TOTEM. CERN, Geneva, 2004.

[8] M. G. Albrow et al. Fp420: An r&d proposal to investigate the feasibility of installing proton tagging detectors in the 420-m region at lhc. CERN-LHCC-2005-025.

[9] Jeff R. Forshaw. Diffractive higgs production: Theory. 2005.

[10] S. Eidelman et al. Review of particle physics. *Phys. Lett.*, B592:1, 2004.

[11] Krzysztof Piotrzkowski. High energy two-photon interactions at the lhc. 2002.

[12] V. M. Budnev, I. F. Ginzburg, G. V. Meledin, and V. G. Serbo. The two photon particle production mechanism. physical problems. applications. equivalent photon approximation. *Phys. Rept.*, 15:181–281, 1974.

[13] K. Hencken, P. Stagnoli, D. Trautmann, and G. Baur. Photon photon and photon hadron physics at relativistic heavy ion colliders. *Nucl. Phys. Proc. Suppl.*, 82:409–413, 2000.

[14] Robert N. Cahn and J. D. Jackson. Realistic equivalent photon yields in heavy ion collisions. *Phys. Rev.*, D42:3690–3695, 1990.

[15] Manuel Drees, John R. Ellis, and D. Zeppenfeld. Can one detect an intermediate mass higgs boson in heavy ion collisions? *Phys. Lett.*, B223:454, 1989.

[16] G. Baur et al. Hot topics in ultra-peripheral ion collisions. 2002.

[17] Gerhard Baur, Kai Hencken, Dirk Trautmann, Serguei Sadovsky, and Yuri Kharlov. Coherent gamma gamma and gamma a interactions in very peripheral collisions at relativistic ion colliders. *Phys. Rept.*, 364:359–450, 2002.

[18] (ed.) Jarlskog, G. and (ed.) Jonsson, L. Two photon physics at LEP and HERA. Proceedings, Workshop, Lund, Sweden, May 26-28, 1994.

[19] G. Levman. Muon pair production by two photon collisions at hera. In *Hamburg 1991, Proceedings, Physics at HERA, vol. 1* 623- 628. (see HIGH ENERGY PHYSICS INDEX 30 (1992) No. 12988).

[20] A. G. Shamov and Valery I. Telnov. Precision luminosity measurement at lhc using two-photon production of mu+ mu- pairs. *Nucl. Instrum. Meth.*, A494:51–56, 2002.

[21] S. P. Baranov, O. Duenger, H. Shooshtari, and J. A. M. Vermaseren. Lpair: A generator for lepton pair production. In *Hamburg 1991, Proceedings, Physics at HERA, vol. 3* 1478-1482. (see HIGH ENERGY PHYSICS INDEX 30 (1992) No. 12988).

[22] K. Hencken, Yu. V. Kharlov, G. V. Khaustov, S. A. Sadovsky, and V. D. Samoylenko. Tphic, event generator of two photon interactions in heavy ion collisions. IFVE-96-38.

[23] Maarten Boonekamp and Tibor Kucs. Pomwig v2.0: Updates for double diffraction. *Comput. Phys. Commun.*, 167:217, 2005.

[24] V. A. Khoze, A. D. Martin, and M. G. Ryskin. Prospects for new physics observations in diffractive processes at the lhc and tevatron. *Eur. Phys. J.*, C23:311–327, 2002.

[25] Valery A. Khoze, Alan D. Martin, and M. G. Ryskin. Can the higgs be seen in rapidity gap events at the tevatron or the lhc? *Eur. Phys. J.*, C14:525–534, 2000.

[26] John C. Collins. Light-cone variables, rapidity and all that. 1997.

[27] A. De Roeck, V. A. Khoze, A. D. Martin, R. Orava, and M. G. Ryskin. Ways to detect a light higgs boson at the lhc. *Eur. Phys. J.*, C25:391–403, 2002.

[28] J. Monk and A. Pilkington. Exhume: A monte carlo event generator for exclusive diffraction. *Comput. Phys. Commun.*, 175:232–239, 2006.

[29] S. M. Troshin and N. E. Tyurin. Energy dependence of gap survival probability and antishadowing. *Eur. Phys. J.*, C39:435–438, 2005.

[30] Michael Spira. Qcd effects in higgs physics. *Fortsch. Phys.*, 46:203–284, 1998.

[31] A. Djouadi, J. Kalinowski, and M. Spira. Hdecay: A program for higgs boson decays in the standard model and its supersymmetric extension. *Comput. Phys. Commun.*, 108:56–74, 1998.

[32] Torbjorn Sjostrand, Leif Lonnblad, and Stephen Mrenna. Pythia 6.2: Physics and manual. 2001.

[33] V. A. Khoze, A. D. Martin, and M. G. Ryskin. Hunting a light cp-violating higgs via diffraction at the lhc. *Eur. Phys. J.*, C34:327–334, 2004.

[34] A.G. Oganesyan K.A. Ispiryan, I.A. Nagorskaya and V.A. Khoze. *Sov. J. Nucl. Phys.*, 11:712, 1970.

[35] D. L. Borden, V. A. Khoze, W. J. Stirling, and J. Ohnemus. Three-jet final states and measuring the $\gamma\gamma$ width of the higgs at a photon linear collider. *Physical Review D*, 50:4499, 1994.

[36] Valery A. Khoze, Alan D. Martin, and M. G. Ryskin. Double-diffractive processes in high-resolution missing- mass experiments at the tevatron. *Eur. Phys. J.*, C19:477–483, 2001.

[37] A. B. Kaidalov, V. A. Khoze, A. D. Martin, and M. G. Ryskin. Central exclusive diffractive production as a spin parity analyser: From hadrons to higgs. *Eur. Phys. J.*, C31:387–396, 2003.

[38] (Ed.) Bruning, O. et al. Lhc design report. vol. i: The lhc main ring. CERN-2004-003-V-1.

[39] W. W. Armstrong et al. Atlas: Technical proposal for a general-purpose p p experiment at the large hadron collider at cern. CERN-LHCC-94-43.

[40] Cms, the compact muon solenoid: Technical proposal. CERN-LHCC-94-38.

[41] Alice: Technical proposal for a large ion collider experiment at the cern lhc. CERN-LHCC-95-71.

[42] Lhcb technical design report: Reoptimized detector design and performance. CERN-LHCC-2003-030.

[43] V. Berardi et al. Totem: Technical design report. total cross section, elastic scattering and diffraction dissociation at the large hadron collider at cern. CERN-LHCC-2004-002.

[44] Atlas inner detector: Technical design report. vol. 2. CERN-LHCC-97-17.

[45] Atlas inner detector: Technical design report. vol. 1. CERN-LHCC-97-16.

[46] M. S. Alam et al. Atlas pixel detector: Technical design report. CERN-LHCC-98-13.

[47] A. Manara. *Particle identification using time-over-threshold measurements in the ATLAS transition radiation tracker.* PhD thesis, INDIANA UNIVERSITY, 2000.

[48] Atlas liquid argon calorimeter: Technical design report. CERN-LHCC-96-41.

[49] M. I. Ferguson et al. Electron test beam results for the atlas liquid argon forward calorimeter prototype. *Nucl. Instrum. Meth.*, A383:399–408, 1996.

[50] Atlas tile calorimeter: Technical design report. CERN-LHCC-96-42.

[51] Atlas first-level trigger: Technical design report. CERN-LHCC-98-14.

[52] S Ask, D Malon, T Pauly, and M Shapiro. Report from the luminosity task force. Technical Report ATL-GEN-PUB-2006-002. ATL-COM-GEN-2006-003. CERN-ATL-COM-GEN-2006-003, CERN, Geneva, Jul 2006.

[53] A M. Cooper-Sarkar. Low-x physics and w and z production at the lhc. 2005.

[54] B L Caron and J L Pinfold. *Luminosity Measurement at the Large Hadron Collider.* PhD thesis, University of Alberta, Edmonton, AL, 2006. Presented on 13 Apr 2006.

[55] U. Amaldi et al. The real part of the forward proton proton scattering amplitude measured at the cern intersecting storage rings. *Phys. Lett.*, B66:390, 1977.

[56] D. Bernard et al. The real part of the proton - anti-proton elastic scattering amplitude at the center-of-mass energy of 546- gev. *Phys. Lett.*, B198:583, 1987.

[57] A. Gorisek. 2005.

[58] D. Acosta et al. The cdf cherenkov luminosity monitor. *Nucl. Instrum. Meth.*, A461:540–544, 2001.

[59] D. Acosta et al. The performance of the cdf luminosity monitor. *Nucl. Instrum. Meth.*, A494:57–62, 2002.

[60] E. W. Weisstein. *Millimeter/submillimeter Fourier Transform Spectroscopy of Jovian Planet Atmospheres.* PhD thesis, AA(CALIFORNIA INSTITUTE OF TECHNOLOGY.), January 1996.

[61] P. Barrillon et. al. Maroc: Multi-anode read out chip for mapmts. *Proceeding of IEEE-2006 Nuclear Science Symposium, San Diego, U.S.A.*, 29 Oct.2 Nov. 2006.

[62] Private Communications Mauro Villa.

[63] R. Arnold et al. A ring imaging cherenkov detector: The delphi barrel rich prototype. part b: Experimental studies of the detector performance for particle identification. *Nucl. Instr. Meth,*, A270:289–318, 1988.

[64] W. R. Leo. Techniques for nuclear and particle physics experiments: A how to approach. page 201. Berlin, Germany: Springer (1987) 368 p.

[65] *http : //p25ext.lanl.gov/ ∼ hubert/aerogel/agel_note.ps.*

[66] M. Asai. Geant4-a simulation toolkit. *Trans. Amer. Nucl. Soc.*, 95:757, 2006.

[67] R. Brun and F. Carminati. Simulation: Status and future trends for geant. Prepared for 9th International Conference on Computing in High-energy Physics (CHEP 91), Tsukuba, Japan, 11-15 Mar 1991.

[68] *http://lepton.bartol.udel.edu/∼eng/phojet.html.*

[69] A Kupco. Mc event generators and their predictions for minimum bias events at lhc energies. Technical Report ATL-PHYS-99-019, CERN, Geneva, Apr 1999.

[70] CDF Collaboration Aaltonen et. al. *Phys. Rev. Lett.*, 99:24002, 2007.

[71] M. G. Albrow and A. Rostovtsev. Searching for the higgs at hadron colliders using the missing mass method. 2000.

[72] Segal J. 3d - a proposed new architecture for solid-state radiation detectors. *Nuclear Instruments and Methods in Physics Research Section A: Accelerators, Spectrometers, Detectors and Associated Equipment*, 395, 21 August 1997.

[73] S. I. Parker and C. J. Kenney. Performance of 3-d architecture silicon sensors after intense proton irradiation. *IEEE Trans. Nucl. Sci.*, 48:1629–1638, 2001.

[74] C. Da Via et al. Advances in silicon detectors for particle tracking in extreme radiation environments. *Nucl. Instrum. Meth.*, A509:86–91, 2003.

[75] Private Communications Andrew Brandt.

[76] K. Fujikawa. Muon pair creation via two-photon exchange in charged-particle collisions. 2. hadron collisions. *Nuovo Cim.*, A12:117–132, 1972.

[77] Private Communications Peter Bussey.

[78] A. Rimoldi et al. Atlas detector simulation: Status and outlook. Prepared for 9th ICATPP Conference on Astroparticle, Particle, Space Physics, Detectors and Medical Physics Applications, Villa Erba, Como, Italy, 17-21 Oct 2005.

[79] A Ventura. Muon reconstruction and identification for the event filter of the atlas experiment. Technical Report ATL-DAQ-CONF-2007-001. ATL-COM-DAQ-2005-035, CERN, Geneva, Oct 2005. Talk given in the parallel session High Energy Physics of the 9th ICATPP Conference.

Appendix A

Estimation of Systematic Error from Beam Optics

The number of hits per unit η is approximately linear with respect to η in the LUCID region, as shown in Fig.A.1. So we have

$$\frac{dN}{d\eta} = K, \tag{A.1}$$

where K is constant. At small angles $tan\frac{\theta}{2} \approx \frac{\theta}{2}$, so the pseudorapidity can be written as

$$\eta = -ln\left(tan\frac{\theta}{2}\right) \approx -ln\frac{\theta}{2}, \tag{A.2}$$

thus

$$d\eta = -\frac{1}{\theta}d\theta. \tag{A.3}$$

Assume one LUCID tube is located in η with a size $\pm\epsilon$ in η, the total number of hits in that tube should be proportional to the integral:

$$N = K\int d\eta = -K\int_{\theta-\epsilon}^{\theta+\epsilon}\frac{1}{\theta}d\theta = Kln\left(\frac{\theta-\epsilon}{\theta+\epsilon}\right) \approx 2K\epsilon\theta. \tag{A.4}$$

So the percentage variance of the number of hits in a LUCID tube is equal to the percentage variance of the θ angle of the position of the tube:

$$\frac{\Delta N}{N} = \frac{\Delta\theta}{\theta}. \tag{A.5}$$

The measurement error caused by different beam conditions is equivalent to the effective θ change for the LUCID tubes under these conditions.

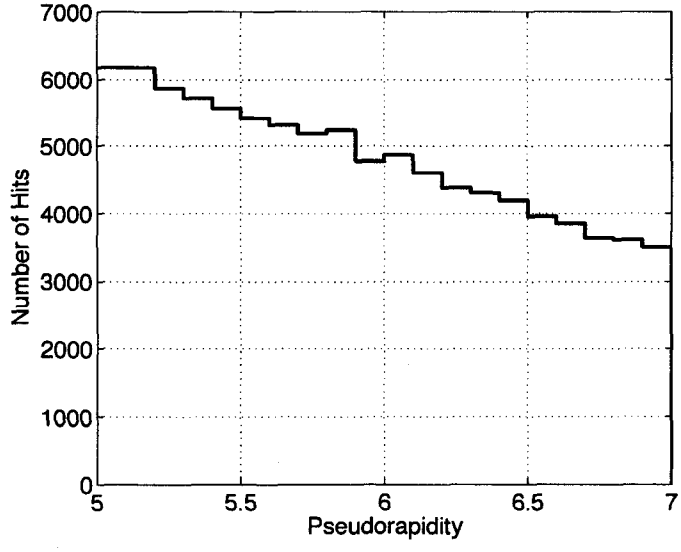

Figure A.1: *Relation of number of hits per unit η. The plot is obtained the minimum bias events generated by PHOJET 1.12 (same as used in LUCID background simulation). The number of hits N and η have close to a linear relation: $dN/d\eta = constant$.*

As shown in Table.7.1, the calibration beam has a sigma beam size 606 μm in the transverse X and Y planes. Fig. A.2 illustrates the change of angle due to the transverse beam size.

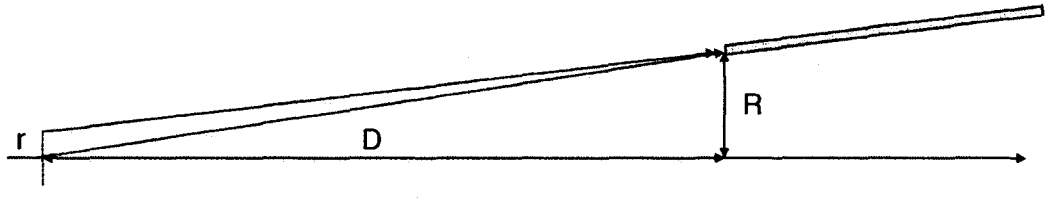

Figure A.2: *Effect of beam size on LUCID acceptance. The horizontal line is the Z axis.*

For a LUCID tube

$$\theta \approx \frac{R}{D} = \frac{96\,\text{mm}}{17000\,\text{mm}} = 5.65\,\text{mrad}. \tag{A.6}$$

In the case when the vertex position is shifted in the transverse plane for a distance r, the equivalent change of the θ of the LUCID tube is

$$\Delta\theta = \frac{r}{D}. \tag{A.7}$$

So we have

$$\frac{\Delta\theta}{\theta} = \frac{r}{R} = \frac{0.606\,\text{mm}}{96\,\text{mm}} = 0.6\%. \tag{A.8}$$

The average measurement error introduced by the transversal beam size is around 0.6%.

By a similar approach, the measurement error caused by beam divergence can also be related to $\Delta\theta/\theta$.

The beam divergence of the normal beam is 32 μrad, while the divergence of calibration beam is 0.23 μrad which we can neglect. In normal beam conditions, let's consider the extreme condition that the error reaches its maximum.

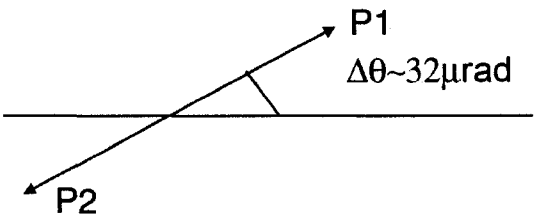

Figure A.3: *Effect of beam divergence on the LUCID acceptance. The horizontal line is the z axis.*

In the situation shown in Fig.A.3, the two protons collide in the opposite direction, which have an angle of 32 μrad with respect to the beam axis (z). This is equivalent to change in the LUCID tube position by 32 μrad, so the error in the measurement is

$$\frac{\Delta\theta}{\theta} = \frac{32\mu\text{rad}}{5.65\text{mrad}} = 0.6\%. \tag{A.9}$$

By adding the error introduced by transverse beam size and beam divergence quadratically, the systematic error caused by the beam optics is $\sqrt{0.006^2 + 0.006^2} = 0.85\% < 1\%$.